COMPUTER BASED CHARACTERIZATION OF A SPATIAL-SPECTRAL (S2) MATERIAL SIGNAL PROCESSOR

by

Ahmed Khallaayoun

A thesis submitted in partial fulfillment
of the requirements for the degree
of

Master of Science

In

Electrical Engineering

MONTANA STATE UNIVERSITY
Bozeman, Montana

April 2006

APPROVAL

of a thesis submitted by

Ahmed Khallaayoun

This thesis has been read by each member of the thesis committee and has been found to be satisfactory regarding content, English usage, format, citations, bibliographic style, and consistency, and is ready for submission to the Division of Graduate Education

Dr. Richard Wolff

Approved for the Department of Electrical Engineering

Dr. James Petersen

Approved for the Division of Graduate Education

Dr. Joseph J. Fedock

STATEMENT OF PERMISSION TO USE

Ahmed Khallaayoun

April 2006

ACKNOWLEDGEMENTS

I would like to thank Prof. Randy Babbitt for giving me the opportunity to be a part of an extraordinary team that made working at The Spectrum Lab an amazing and wonderful research experience. The care and encouragement as well as patience of colleagues were indeed essential.

My deepest thanks go to my supervisor Dr. Tiejun Chang for being so patient with me and for taking me by the hand and teaching me the art of modeling and simulations. I am greatly indebted to Dr. Mingzhen Tian for all her invaluable assistance in writing this dissertation. I would also like to profoundly thank Dr. Krishna Rupavatharam for all the discussions that made the complex seem simple, and also for his unsurpassed kindness and support. I am also grateful to my academic advisor Dr. Richard Wolff for his care and guidance. I thank my fellow graduate student Cy Drollinger for his support and help through all this research experience.

Special thanks and unfathomable love goes to my family. My parents, Abdelwahed Khallaayoun and Soad Benohoud, for their unconditional and constant love and support, as well as to my sisters, Houda and Sara.

Most of all, I would like to thank God, for the blessings and sound belief in Him, health, and sanity and for putting me in a path that allowed me to meet people that have been kind to me and allowing me the opportunity to reciprocate.

TABLE OF CONTENTS

TABLE OF CONTENTS - CONTINUED

TABLE OF CONTENTS - CONTINUED

LIST OF TABLES

LIST OF TABLES-CONTINUED

Table Page

LIST OF FIGURES

LIST OF FIGURES - CONTINUED

Figure Page

LIST OF FIGURES - CONTINUED

Figure Page

LIST OF FIGURES - CONTINUED

LIST OF FIGURES - CONTINUED

LIST OF FIGURES - CONTINUED

Figure Page

ABSTRACT

The Spectrum Lab has developed a computer based model for a new generation processor where one of its applications promises improvement in current and future generation Radars. This processor is named the S2CHIP (Spatial Spectral Coherent Holographic Integrating Processor). The purpose of this work is to characterize the S2CHIP under different conditions in terms of signal strength, noise level and dynamic range. The characterization has been done using a new simulator developed at the Spectrum Lab based on the Maxwell-Bloch equations. This tool enabled us to simulate various effects based not only on the material properties but also effects based on the laser source and other components that make up the overall system. Laser beam geometry, material thickness, integration processing, and material and laser coherence time are addressed in this thesis. These simulations give a good measure on the performance of the S2CHIP.

CHAPTER ONE

INTRODUCTION

The goal of this research was to characterize a revolutionary optical processor namely the Spatial Spectral Coherent Holographic Integrated Processor (S2CHIP). The core of the S2CHIP consists of Spatial-Spectral holographic (SSH) material. The technology based on SSH materials proved promise in wideband bandwidth applications in fields of optical memory [1], RF spectrum analysis [2], atmospheric seeing [3], arbitrary waveform generation [4], and range-Doppler radar [5], among others. The S2CHIP has shown potential in improving radar resolution (range and Doppler), increase optical memory densities, and help produce much better spectrum analyzers in terms of bandwidth and resolution. This thesis discusses how the S2CHIP technology behaves in the context of radar applications. We use a simulator to study and characterize the S2CHIP in terms of the material thickness, laser beam geometry, integration processing, laser and material coherence time.

Most of the terms used in this thesis are not common in the "Electrical Engineering" community, hence, the rest of the introduction as well as the first chapter are dedicated to explaining and clarifying the background to enable the reader to benefit from the results of this research without any ambiguity.

Introduction to Research Topic

In radars, target detection starts by sending an electromagnetic wave (Tx), which propagates through free space. Once an object with an impedance different then the one of free space is encountered, a portion of the original wave is reflected (R_x) and detected after some time τ. This delay determines the range (R) or the target's distance from the radar. The frequency or Doppler shift in the return signal determines the velocity of the target. The range and the delay are related as shown in equation (1.1)

$$R = \frac{c\tau}{2} \tag{1.1}$$

Where τ = round trip propagation time, c = speed of light.

In conventional radars, the transmit (reference) and the return signals are digitized, Fourier transformed, matched to the reference signal, and then finally converted back to the time domain for range and Doppler extraction. The digital matched filtering for the radar application requires very high bandwidth ADCs (Analog to Digital Converters) which limits the resolution that radars can attain. In addition, an unwanted delay is caused by the extensive data processing required to extract the range and Doppler information.

The S2CHIP, on the other hand, has the ability to process ultra-wideband signals with high dynamic range. As depicted in Figure 1, where the gray area represents the S2CHIP module, the transmit and return signals, which are at RF frequencies, are modulated onto an optical carrier and stored in the S2 material using a stabilized laser, this process is known as the writing or programming process. Another laser beam is used to retrieve the data from the S2 material which is know as the readout or probing process, finally the optical beam containing all the desired data is detected and post processed to extract range and Doppler information with very high resolution. With an instantaneous bandwidth of more then 20 GHz, the S2CHIP is able to process the transmit and return signal without the need for low noise amplifiers or digitization[1]. The S2CHIP will eliminate the traditional receiver complexity and improve the current and next generation radar systems.

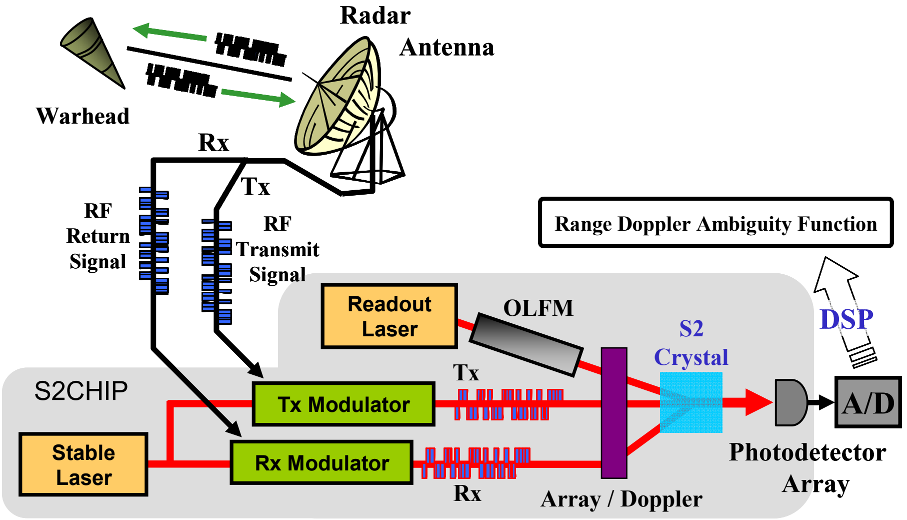

Figure 1 Schematic of S2CHIP range-Doppler radar processor [5]

The research work presented in this thesis is based on exercising a simulator that relies on the basic numerical computation of Maxwell-Bloch (MB) equations. MB equations model the evolution of the field, atomic polarization, and the population

---

[1] The digitization will eventually be needed after detection but the bandwidth after detection will be low compared to the processing bandwidth.

component in an inhomogeneously broadened medium. The simulator will be described in detail later in this thesis (refer to Chapter 3). This work determines the S2CHIP performance under different conditions and how different parameters will affect the ranging in terms of the dynamic range.

The basic approach to the S2CHIP technology can be summarized in two basic steps. First, the material is illuminated by an optical beam. The material inherently stores the combined power spectrum of the input signal. The stored spectral content contains all the amplitude and phase information of the temporally modulated signals only now it is stored in the material in the spectral domain. At this stage, the material is in essence an absorptive spectral filter. The second step consists of sending another optical waveform that will interact with the stored filter and produce the processed signal.

In the chapter that follows, a concise background on the principles that make the S2CHIP technology possible is presented, the third chapter includes an overview of the Maxwell-Bloch simulator. Propagation effects on the signal dynamic range are discussed in chapter four. The fifth chapter is dedicated to the study of interference and cross talk that occurs in the S2 material. The integration processing is discussed in chapter six. Chapter seven and chapter eight present the simulation results concerning the effects of the material and laser coherence time on the signal dynamic range, respectively. Finally, chapter nine discusses the laser beam geometry. The simulations and results have enabled evaluation of the device performance and have led to a better understanding of how the device behaves under certain parameters.

My contribution to this research consists of using my electrical engineering knowledge to characterize a novel optical processor. The research consisted of understanding the concepts of the technology behind the S2CHIP and pushing the material to the level where it is efficient and understanding how it behaves under those conditions. The concepts of signal processing knowledge including intermodulation and harmonics analysis, signal analysis in time and frequency domain, digitization, as well as extensive data analysis among others, were all necessary to achieve my research goal.

CHAPTER TWO

TECHNOLOGY AND BACKGROUND

This chapter explains some of the processes and phenomena that have led to the S2CHIP technology. This chapter answers the question: how does the S2CHIP processor store and process information and how is the information retrieved? First, the spectral hole burning and optical coherent transient is introduced, the focus then shifts to the material properties to understand how spatial-spectral holography occurs in this material.

The S2CHIP technology is based on the coherence interaction of the optical pulses with inhomogeneously broadened absorbers. As shown in Figure 2, an atom is excited from the ground to the excited state if a photon with energy E_p equal to the difference in energy ΔE between the excited state E_e and ground state E_g is absorbed. When an atom relaxes from the excited to the ground state a photon is radiated, the decay of the atom to the ground state can either occur spontaneously or by stimulation. In spontaneous emission the decay rate Γ_e is related to the upper state lifetime T_1, $T_1 = \frac{1}{2\pi\Gamma_e}$. The upper state life time of material such as Tm^{3+}: YAG is in the order of 1ms [6]. In the stimulated emission, a photon is used to induce the transition of the atom from the excited to the ground state. The emitted photons add coherently to the input field.

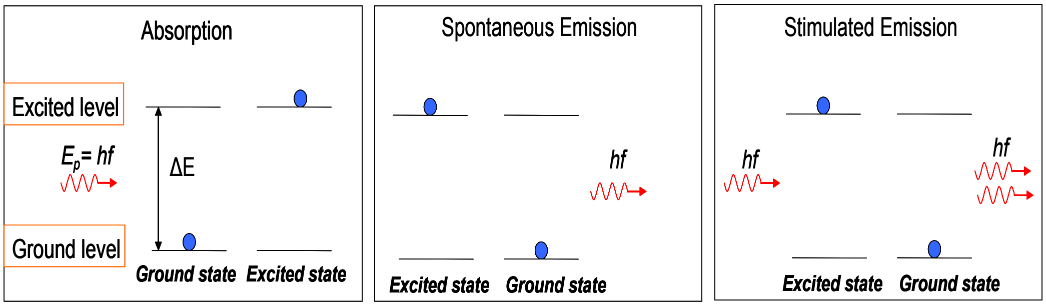

Figure 2 Absorption and emission in a two level atomic representation

Homogeneous and Inhomogeneous Broadening

Rare-earth elements such as lanthanides are elements with an atomic number ranging from 57 (lanthanum) to 70 (ytterbium). When rare earth ions are doped into an inorganic crystal (e.g. Tm^{3+}:YAG) two major broadening mechanisms take place, Homogeneous and inhomogeneous broadening. Figure 3 shows how the homogeneous and inhomogeneous broadening occur.

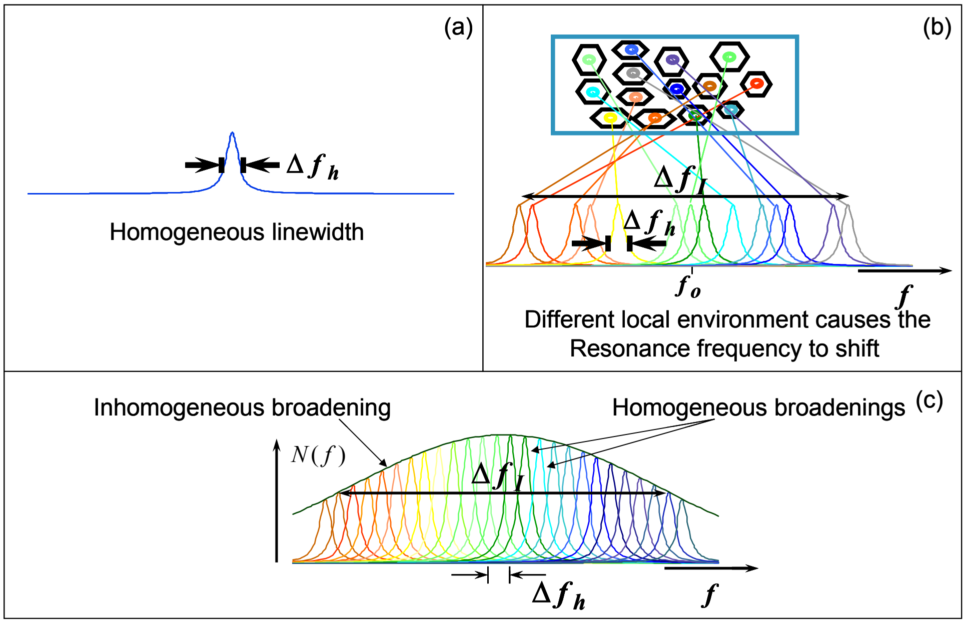

Figure 3 (a) homogenous linewidth (b) shifting of the resonance frequency of atoms due to different local environment (c) homogeneous and inhomogeneous broadening.

At cryogenic temperatures (<10^{o} Kelvin), each individual ion doped in the crystal has a very sharp resonance with a width Δf_h called the homogeneous linewidth as depicted in Figure 3 (a), since the broadening is experienced equally by all ions in the medium. The homogenous linewidth is related to the material coherence lifetime T_2, $T_2 = \frac{1}{\pi \Delta f_h}$. The inhomogeneous broadening is due to the imperfections in the crystal, each atom in the medium experiences a slightly different environment causing a shift in the resonance frequencies of the individual atoms as illustrated in Figure 3 (b). Since the imperfections are random, the inhomogeneous broadening usually has a Gaussian profile as depicted in Figure 3 (c).

The interaction of temporally structured coherent pulses (e.g. laser beams) resonant with rare earth doped crystals (e.g. Tm^{3+}:YAG) is described by what is known as Optical Coherent Transient (OCT). In other words, OCT process describes how an optical coherent pulse will behave as it passes through an S2 material.

Spectral Hole Burning and Photon Echoes

If a narrowband laser is incident on the S2 material, it selectively excites the group of ions resonant with the laser's wavelength to the excited state and thus burning a hole in the absorption profile of the medium. This process is called spectral hole burning.

When a modulated optical pulse is incident in the medium the spectral content of that particular pulse is imprinted in the medium. The spectral distribution of the pulse contains more energy in some frequencies than others. Intuitively, the frequencies with more energy will excite more ions and ones with less energy will excite fewer ions, thus creating a spectral profile. If we take the example where two brief pulses with a time delay τ_d are incident on the medium, the S2 material will store the spectral content of these pulses, which is a spectral grating with a period of $1/ \tau_d$.

When an optical pulse interacts with the spectral grating already present in the S2 material, a delayed replica of the pulse is generated and is called a photon echo. In the process involving three input pulses, the echo is usually called *stimulated photon echo*. Two input pulses can result in photon echo as well and it is called *two-pulse echo*. The two-pulse echo can be regarded as an extreme of the three-pulse case with the second and third pulses temporally overlapped with each other.

When the three input pulses are collinear, the echo pulse propagates in the same direction as the input. If the first two pulses propagate in different directions, they create a spatial-spectral grating in the material. After the probe pulse, the echo, is generated in the direction of $\vec{k}_e = \vec{k}_3 + \vec{k}_2 - \vec{k}_1$, where $\vec{k}_i$ represents the direction of the ith pulses.

S2 Material Programming and Readout

To program the S2 material, either brief Gaussian pulses or coded waveforms are used. The brief Gaussian pulses are used in the simulation environment in order to minimize the computational time and simplify the simulation in order to study a particular effect. In real life cases, coded waveforms such as binary phase shift keying (BPSK) are used in order to provide processing gain [7]. The codes used are specified by there length (N) and the bit rate (R_b). A typical N-bit BPSK with pseudo-random noise signal provides a signal to sidelobe ratio of $\sim \sqrt{N}$.

In addition to the length and types of codes used, integration is used to increase processing gain. Integration consists of using a series of waveforms (multiple shots), the power spectrum of each shot is accumulated in the material which enhances the contrast of the spectral grating. The repetition rate is set higher then the coherence time of the material to minimize coherent interference between the shots. If the same code is used for a particular number of shots (J), the peak to sidelobe ratio (PSR) is increased by $\sqrt{J}$.

In the radar application, the goal in the readout stage is to obtain the spectral content stored in the material such that the information about the range and velocity of the target can be extracted. This thesis focuses on the ranging aspect, i.e. readout the spectral grating period or the echo delay.

In most of the simulations presented in this thesis, low bandwidth readout of high bandwidth processing is used. This is achieved by using low power optical pulses with linear frequency modulation, namely, optical frequency chirped pulses. The chirped pulses are characterized by there chirp rate (κ) which is defined as $\kappa = \frac{B_c}{T_c}$, where T_c is the chirp time and B_c is the chirp bandwidth. The readout chirped pulse with a field amplitude E_R, can be written as:

$$E_R(t) = E_R \cos\left(\left(\omega_L - \frac{1}{2}B_c\right)t + \frac{1}{2}\kappa t^2\right)$$

Once the chirp field interacts with a spectral feature, the output field contains the coherence feedback from the material, which carries the complete information about the stored spectral feature. As depicted in Figure 4, once a chirped field is incident on the S2 material, the output field is modified such that in Figure 4 (a) the field contains an attenuated duplicate of the spectral hole. In Figure 4 (b), the output for a grating contains a transmission field and its delayed replica. The transmission and echo fields are spatially and temporally overlapped, and a beat signal $\left|E_{trans}(t) + E_e(t)\right|^2$ representing the spectral grating. The echo delay time can be obtained by Fourier transforming the detected spectral grating.

Another geometry that will discussed in this thesis is the angled beam geometry where the pulses used are on different spatial paths, the benefit from this geometry as it will be discussed later separates the transmitted and echo fields spatially. As depicted in Figure 4 (c) the angled beam geometry spatially separates the transmission and echo fields, the spatial-spectral grating is contained in the echo field, yet, the grating can be extracted by beating the echo field with the reference field.

The angled beam geometry offers many advantages over the collinear one, on the processing, readout and detection. The angled beam geometry provides high dynamic range for the signals compared to the collinear geometry. The desired delay, which provides us with the range of the target, is obtained by beating the transmitted field with the output echo field in the collinear geometry. In the angled beam geometry, the output echo field is beaten with the input field which proves to significantly improve the dynamic range of the signal as will be shown in chapter nine.

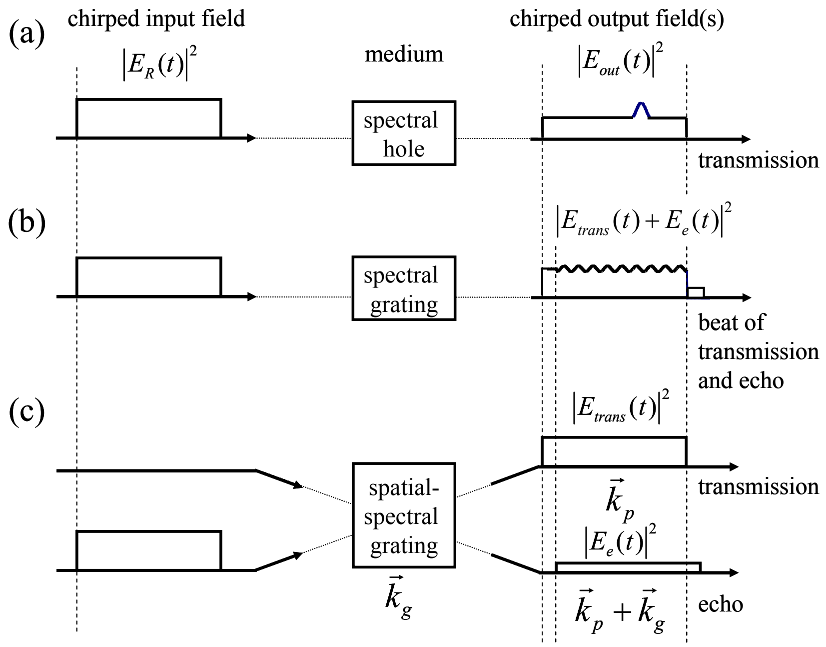

Figure 4 Chirped field readout illustration for (a) spectral hole (b) spectral grating (c) angled beam geometry for a spatial-spectral grating. The left side of figure represents the intensity of the input chirped field, the middle represents the medium with different features programmed in it, and the right side portion of the figure represents the output field intensities. Note: this figure was extracted from [12]

Under the conditions that the S2CHIP is configured (using thick medium, multiple shots or integration…), the response of the S2 material proves to becoming nonlinear, the study of distortion become of the essence in this case. In the case where a single delay spectral grating is generated nonlinear effect start to manifest by mean of having energy appearing at multiples of the principal frequency, namely, harmonics. In addition to harmonics, when a multiple delay spectral grating is studied, the intermodulations which are defined as two frequencies present simultaneously appear as new distortion.

Let us assume a modulation where two cosine waveforms are used $\cos(\omega_1 t)$ and $\cos(\omega_2 t)$, the principal peak is present at frequencies, ω_1 and ω_2, the second order intermodulation is present at $\omega_1 \pm \omega_2$, and the third order intermodulation will be present at frequencies, $2\omega_1 \pm \omega_2$ and/or $2\omega_2 \pm \omega_1$. When ω_1 and ω_2 are equal, the harmonics order follows as the principal peak ω, and the second order harmonic is at 2ω and the third order harmonic is at 3ω. Chapter 5 is dedicated to the study of intermodulation.

The reader should note that in the coming chapters the term dynamic range (DR) and spur free dynamic range will be used extensively. The dynamic range (DR) represents the ratio between the principal peak (signal peak) and the averaged noise floor level, the spur free dynamic range (SFDR) on the other hand represents the ratio between the principal peak and the sidelobe averaged value.

OCT processes which are of interest in this thesis are very complex, yet, there exists an approach that approximates the OCT processes under certain conditions. The Fourier Transform approximation (FTA) approach taken by Mossberg in the early 80's approximates the OCT processes under the conditions that the optical pulses used are optically weak [1]. The FTA is discussed in the next section.

Fourier Transform Approximation

Mossberg has approximated the OCT process using the Fourier Transform Approximation (FTA), which will help the reader understand the OCT process. One should note that the FTA is only valid when weak optical pulses are used to program and readout the S2 material (linear regime).

Consider a linear time invariance filter (LTI), as shown in Figure 5, with an input x(t) and an output y(t), the signal x(t) is altered by a transfer function $h(t)$ to produce an output signal y(t). In the time domain the output can be written as:

$$y(t) = h(t) * x(t) \tag{2.1}$$

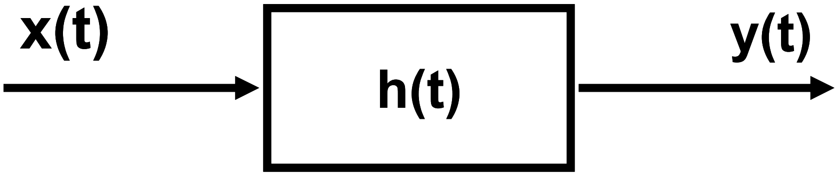

Figure 5 Linear time invariant filter diagram

In an LTI system, the superposition principle applies, and describes the inputs and outputs by a linear relationship, meaning that for k input signals the system is expected to produce k output signals. In addition, a time shift applied to the input will result in an equal time shift at the output. Using the two properties mentioned, the output y(t) is the convolution of the input x(t) with response to the filter $h(t)$.

$$y(t) = \int_{-\infty}^{\infty} x(\tau)h(t-\tau)d\tau = x(t) * h(t)$$

The Fourier transform is used to obtain the spectral components of x(t), and is defined as:

$$X(\omega) = \frac{1}{2\pi}\int_{-\infty}^{\infty} x(t)e^{-i\omega t}dt \Leftrightarrow x(t) = \int_{-\infty}^{\infty} X(\omega)e^{i\omega t}d\omega \qquad (2.2)$$

Rewriting equation (2.2) in the frequency domain the output becomes:

$$Y(\omega) = X(\omega)H(\omega) \qquad (2.3)$$

The OCT process imprints $H(\omega)$ and generates $Y(\omega)$ using three pulses. The first two $E_1(t)$ and $E_2(t-\tau_{21})$ which are time dependent and separated in time by a delay τ_{21} can be written in the Fourier domain as $E_1(\omega)$ and $E_2(\omega)e^{-i\omega\tau_{21}}$, these pulses produce $H(\omega)$. To generate $Y(\omega)$ a third pulse $E_3(t-t_3)$ or $E_3(\omega)e^{-i\omega t_3}$.

At any particular frequency the electric field strength is related to the excitation of the absorbers in the ground state. The Fourier transform of a waveform containing two combined sinwave is ideally two impulses at the frequencies at which the temporal waves are modulated. In the S2 material, the same concept is applied, only we use two brief pulses and the material stores the information spectrally, the sinwave (transform of the two brief pulses) is manifested in the material by changing the population in the ground state differently at each frequency, which creates a spectral grating in the S2 material.

When the pulses are incident on the medium, their interference effect is the sum of the two Fourier transform power spectra. The combined power spectrum is the square of the electric fields amplitudes, which follows as:

$$\begin{aligned}|E_{21}(\omega)|^2 &= \left|E_1(\omega)+E_2(\omega)e^{-i\omega\tau_{21}}\right|^2 \\ &= |E_1(\omega)|^2+|E_2(\omega)|^2+E_1(\omega)E_2^*(\omega)e^{i\omega\tau_{21}}+E_1^*(\omega)E_2(\omega)e^{-i\omega\tau_{21}}\end{aligned} \tag{2.4}$$

The first two term in equation (2.4) represent the power spectra of the first and second pulse, the rest of the terms are the cross terms which represent the interference of the power spectrum of each pulse. These later terms contain the full amplitude and phase information for each pulse. The third term is not considered since it is not causal.

By using a third pulse $E_3(t-t_3)$ to probe the medium, the pulse will act on each atom and will cause an emission signal proportional to the number of absorbers in the ground state. The output signal in the time domain can be written as:

$$E_{out}(t) \propto \int_{-\infty}^{\infty} |E_{21}(\omega)|^2 E_3(\omega)e^{-i\omega t_3}e^{i\omega t}d\omega \tag{2.5}$$

If only the interference terms are taken from Equation (2.4) then the output signal will become:

$$E_{out}(t) \propto \int_{-\infty}^{\infty} E_1^*(\omega)E_2(\omega)E_3(\omega)e^{-i\omega(t-(t_3+\tau_{21}))}d\omega \qquad 2.6)$$

Equation (2.6) describes the FTA output signal in terms of the input pulses assuming that the pulses used have low intensities to keep the response in the linear region.

The FTA is a quick and useful method, yet, the regime where it is viable involves low pulse intensity. Another method that has been used to solve for an OCT process in an optically thin media is the undepleted pump approximation which simply states that the absorption in the thin medium is so small that the polarization is uniform all through the medium making the output field proportional to the polarization of the medium, thus eliminating the propagation effect. Unfortunately, thin mediums imply low power efficiencies.

Obtaining high power efficiencies is possible in thick media. To describe the full dynamics of the OCT process in this case, it is essential to explain how the propagation affects the polarization which in part affects the output field. The Maxwell wave equation in combination with the optical Bloch equations is needed to describe the full dynamics of the process.

The next chapter will deal with describing the Maxwell-Bloch simulator used in research. The theoretical model that represents this OCT process using Maxwell-Bloch equations will not be represented in the body of this thesis but the reader can learn more about the theory behind the simulator in [8, 9, 14]

CHAPTER THREE

COMPUTER BASED USING MAXWELL-BLOCH EQUATIONS

The Fourier Transform approximation was used under the assumption that the process is linear, in other words, the pulses used are optically weak and that the medium used is optically thin. In the linear regime, it is assumed that the output field is a linear transform of the input pulses as discussed earlier. If high energy pulses are used and saturation is induced, the spectral feature is distorted from the power spectrum of the input pulses. In addition, in optically thick media, the absorption is substantial and the polarization starts to act back on the field and the linear filter theory breaks down as the absorption length increases. To find an accurate solution to an OCT process where the medium is optically thick and high energy pulses are used, the coupled Maxwell-Bloch equation are used. The Bloch equations govern the coherent effect of light interacting with an ensemble of inhomogeneously broadened two level atoms. The Maxwell equations describe the propagation of the field in a thick medium. The simulator based on the coupled Maxwell-Block equations is described in detail in the next sections.

As the S2 materials started to show promise in many applications, and rather then using approximations to predict the behavior of these materials, the development of an accurate simulation tool that relied on Maxwell-Bloch equations proved necessary. The material based simulator was produced by Tiejun Chang at The Spectrum Lab over a period of more then four years. This software is called an OCT simulator since it describes how a signal behaves as it propagates through the S2 material. In the course of developing the OCT simulator, comparison of simulation results to experimental data was used to validate the accuracy of this tool.

Computer Based Simulations for S2CHIP Processing

As mentioned earlier the Maxwell-Bloch (MB) simulator is based on the numerical computation of the Maxwell-Bloch equations. Experiments, though necessary to characterize a system, tend to sometimes mask some of the individual effects (inherent or externally introduced), these effects can be studied in detail in a simulation environment. The MB simulator can virtually predict the field output under all the possible scenarios in an OCT processing. The MB simulator was developed using C++, and a graphical user interface (GUI) has also been developed. The simulator can run on any computer with a Microsoft Windows operating system.

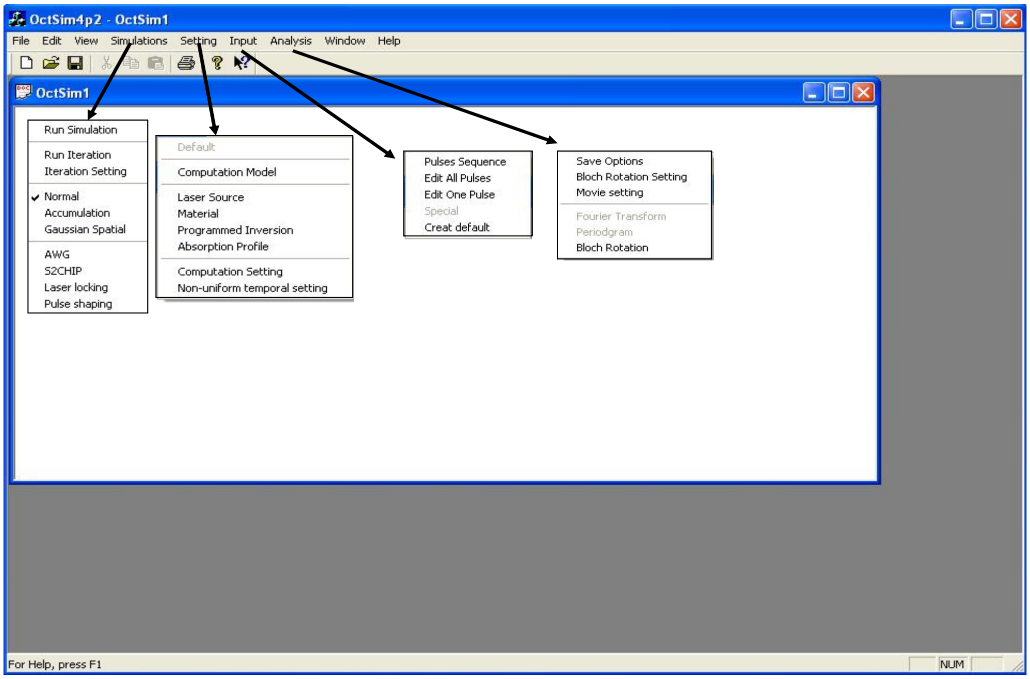

Figure 6 Screen shot Maxwell-Bloch simulator's GUI and the different menu option

As depicted in Figure 6, the different menu options in the GUI allow the user to choose an input pulse sequence of a desired waveform as well as edit the pulse(s) needed to program or to probe the medium. The simulator menu options include the laser source parameters, the S2 material parameters, and the computation settings. The remaining sections of this chapter explain each of the menu options in detail.

Setting

The setting menu option gives the user the alternative to choose a computational model. The model by default is based on Maxwell-Bloch equations. There other computational models that have been developed which are based on Maxwell-Power spectrum, Beer's law-Bloch, and Beer's law-Power Spectrum. The other models are mentioned for generality and they will not be discussed in this thesis.

The simulator allows the user to choose two ways to generate a grating as depicted in Figure 7 (a). In the first method, two or more brief pulses or patterned pulse(s) are used to program a grating into the medium. In second method, the user can utilize the simulator's ability to generate a perfect grating. The user can choose the strength, period, bandwidth, center, and phase of the grating. The simulator also allows the study of preset spectral holes. The spectral holes can be calibrated by there depth, width, and type (Lorenzian or Gaussian).

As shown in Figure 7 (b), the setting menu provides the simulation of a noisy laser by introducing random walk noise and limiting the coherence time of the laser.

In the case where the user chooses to generate his/her own grating, the spectral or spatial-spectral grating can be loaded using the "load to file" function in the simulator, then the user can set any other input to probe that particular grating, either a brief pulse or a chirped field.

Finally, the material properties can also be changed. The user can chose what type of material and absorption profile to use in the simulation as shown in Figure 7 (c). The coherence time along with the population decay can be altered.

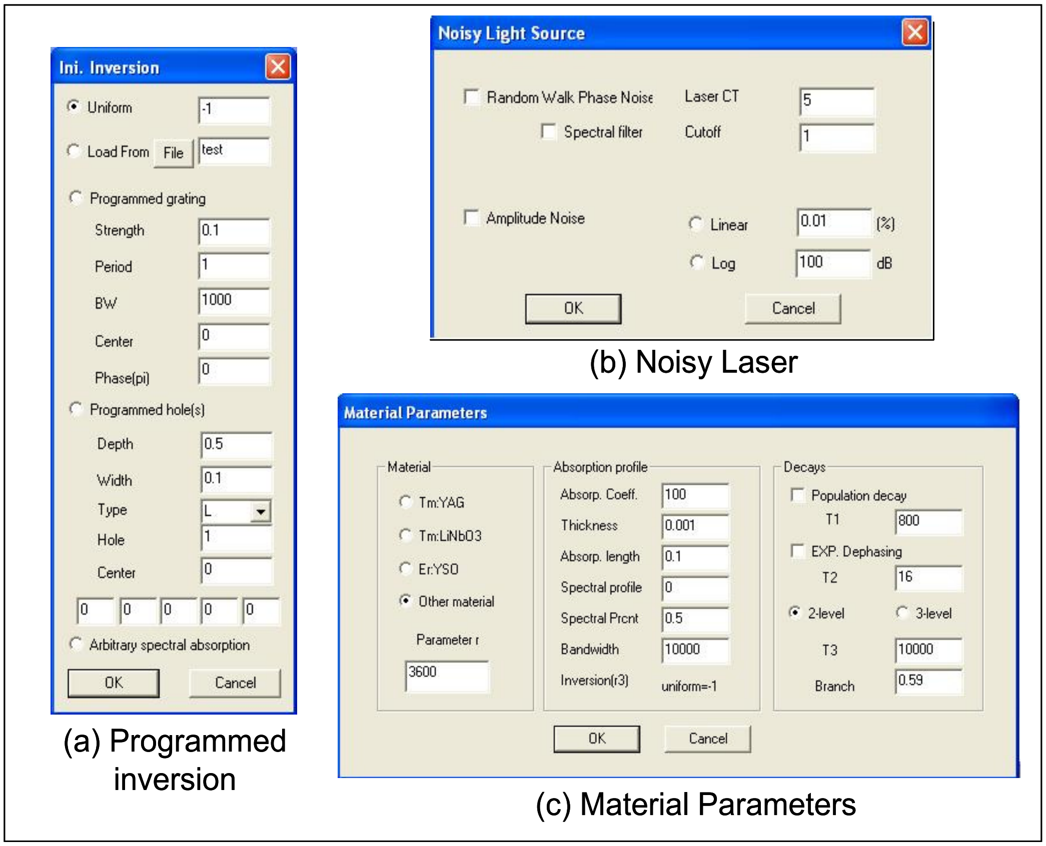

● Uniform -1
○ Load From File test
○ Programmed grating
Strength 0.1
Period 1
BW 1000
Center 0
Phase(pi) 0
○ Programmed hole(s)
Depth 0.5
Width 0.1
Type L
Hole 1
Center 0
0 0 0 0 0
○ Arbitrary spectral absorption

(a) Programmed inversion

☐ Random Walk Phase Noise — Laser CT 5
☐ Spectral filter — Cutoff 1
☐ Amplitude Noise — ○ Linear 0.01 (%) — ○ Log 100 dB

(b) Noisy Laser

Material
○ Tm:YAG
○ Tm:LiNbO3
○ Er:YSO
● Other material
Parameter r 3600

Absorption profile
Absorp. Coeff. 100
Thickness 0.001
Absorp. length 0.1
Spectral profile 0
Spectral Prcnt 0.5
Bandwidth 10000
Inversion(r3) uniform=-1

Decays
☐ Population decay
T1 800
☐ EXP. Dephasing
T2 16
● 2-level ○ 3-level
T3 10000
Branch 0.59

(c) Material Parameters

Figure 7 Setting menu options, (a) programmed inversion (b) noisy Laser (c) material parameters.

One of the important parameters that need to be carefully selected is the computational setting. As illustrated in Figure 8 (a), the computational selection is divided into temporal (time), spectral (frequency), and spatial (space) settings. The non-uniform setting option in the MB simulator which is depicted in Figure 8 (b) offers an effective way to save on computational time. An example of how the computational settings are applied is show later in the chapter.

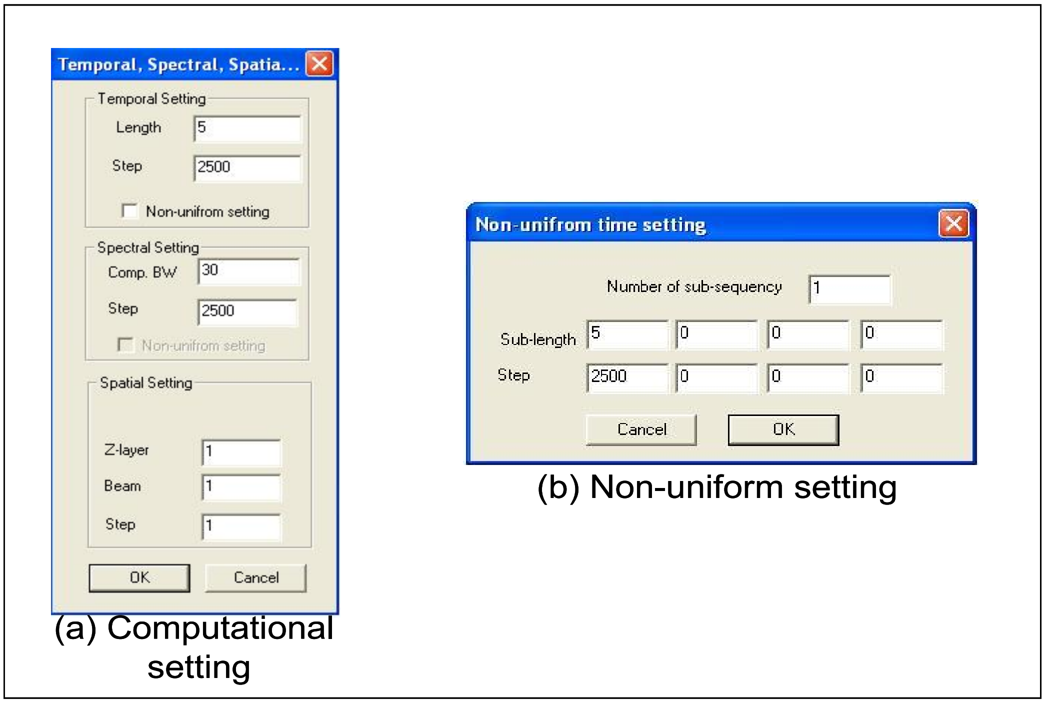
Temporal, Spectral, Spatia...

Temporal Setting
Length: 5
Step: 2500
☐ Non-unifrom setting

Spectral Setting
Comp. BW: 30
Step: 2500
☐ Non-unifrom setting

Spatial Setting
Z-layer: 1
Beam: 1
Step: 1

(a) Computational setting

Non-unifrom time setting

Number of sub-sequency: 1

Sub-length	5	0	0	0
Step	2500	0	0	0

(b) Non-uniform setting

Figure 8 (a) temporal and spectral setting (b) non-uniform time setting

To illustrate the value of the non-uniform setting in terms of computational time, let's take the example where two brief pulses are used to program the medium and a chirped field is used to probe the medium. Usually the brief pulses have a very short duration which requires very high temporal resolution. The chirp rate does not need the sampling rate that was applied for the writing pulses. If a uniform computational setting is applied, the resolution for the feature with the lowest temporal width will set the temporal sampling. This method works fine as long as all the features require the same resolution, but if the resolution required is different then computational time might be wasted. The use of non-uniform setting allows the user to separate the simulation time into separate entities and the user can choose to use the different sampling regimes required for each entity separately, this method proved to have saved us a great deal of computational time.

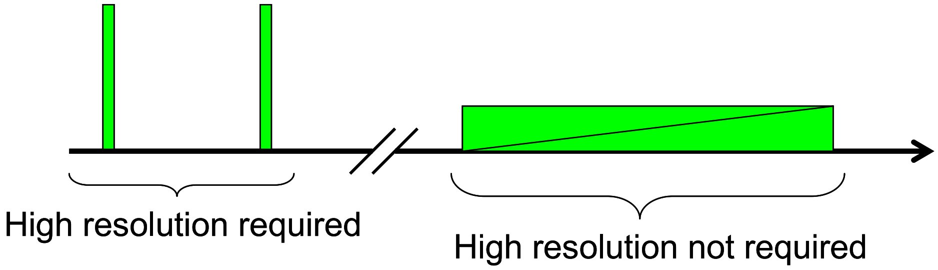

Figure 9 Simulation setup example where non-uniform setting is applied to save on computational time

<u>Input</u>

The edit menu option allows the user to choose from four different options. The pulse sequence as shown in Figure 10 (a) allows the use to set the number of pulses desired, use cut of dephasing, and choose the geometry in with the simulation is to be run. If a pulse is applied to the medium, the medium has a coherence time (T_2) in which it remembers its phase, once another pulse is applied a phenomena called rephasing occurs which in essence makes the coherence of the atoms in the medium go back in time. After a time equal to the delay between the first and second pulse is reached an echo is produced. However, there is a maximum delay where rephasing can occur and that time is equal to the material's coherence time. The cutoff dephasing allows the user to mimic waiting a time T_2 or longer in the lab.

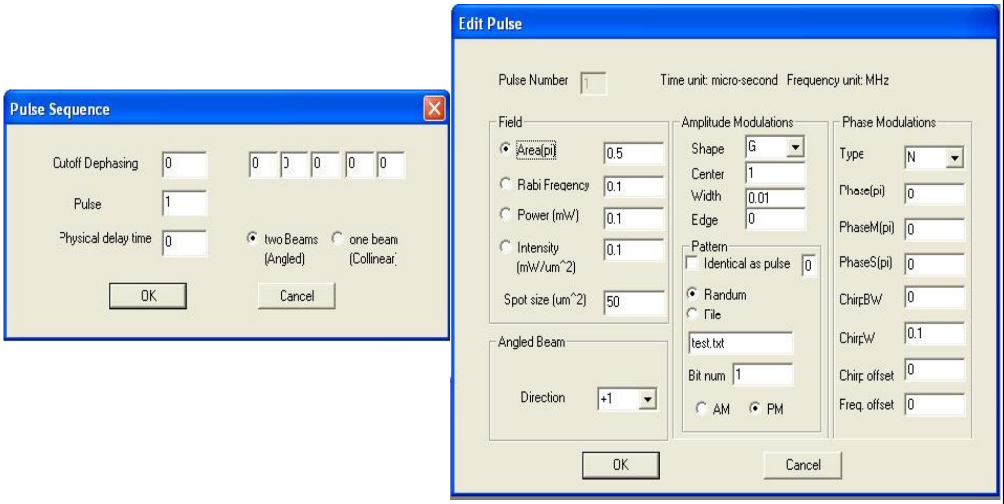

Cutoff Dephasing 0 0) 0 0 0

Pulse 1

Physical delay time 0

● two Beams (Angled) ○ one beam (Collinear)

Pulse Number 1 Time unit: micro-second Frequency unit: MHz

● Area(pi) 0.5

○ Rabi Freqency 0.1

○ Power (mW) 0.1

○ Intensity (mW/um^2) 0.1

Spot size (um^2) 50

Direction +1

Shape G

Center 1

Width 0.01

Edge 0

☐ Identical as pulse 0

● Randum

○ File

test.txt

Bit num 1

○ AM ● PM

Type N

Phase(pi) 0

PhaseM(pi) 0

PhaseS(pi) 0

ChirpBW 0

ChirpW 0.1

Chirp offset 0

Freq. offset 0

(a) Pulse sequence (b) Edit pulse

Figure 10 Pulse sequence (left) and edit pulse (right)

The edit pulse menu option gives the user the ability to edit the pulse or pulses chosen one at a time and the pulse number shows which pulses is being edited. The pulse area is related to the pulse intensity and the Rabi frequency is related to the chirp amplitude used to probe the medium. In the case where a brief pulse is used, the user can chose the area, power, spot size in the medium, direction if the geometry of choice is angled beam. In addition, the pulse shape can also be altered and the shape can be:

- G: Gaussian
- P: Patterns
- S: square
- S/C: square with a cosine edge
- S/G: Square with Gaussian edge
- S/T: Square with a triangular edge

The center of the pulse along with the width and edge duration can be set as well. In the case where a chirped pulse is used, the Rabi frequency is used instead of the area, and the shape of the pulse can either be square, or square with differently shaped edges. In this case, the chirp time (T_c [μs]) and bandwidth (B_c [MHz]) have to be set as well, and the chirp rate (κ) is defined as $\kappa = \frac{B_c}{T_c}$. Another alternative is to use a patterned pulse, where a random pattern can be generated by the simulator itself or loaded from a file generated by the user. If more then one patterned pulse is used, then the user can chose the patterns in different pulses to be the same or different.

Simulations

Once all the settings have been entered, the user can run the simulation using the "Run Simulation" menu option. Figure 11 (a) and (b) shows the setting options for iteration and accumulation respectively. In this research the iteration setting option was "loops without setting change" and was mainly used for noise analysis. The use of iterations allows a better prediction for the noise behavior. To simulate accumulation, the user can choose the number of shots desired and can save the population inversion (r3) every shot or every 5, 10, 20… shots. The accumulation or integration writing and readout processes are shown in Figure 12.

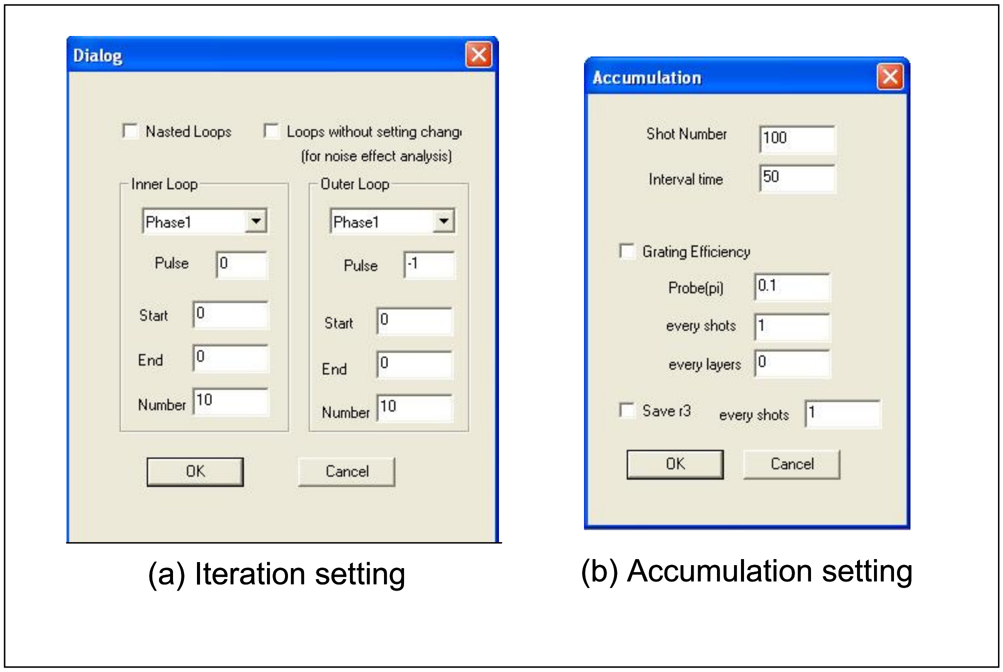
Dialog

☐ Nasted Loops ☐ Loops without setting chang
(for noise effect analysis)

Inner Loop
Phase1
Pulse 0
Start 0
End 0
Number 10

Outer Loop
Phase1
Pulse -1
Start 0
End 0
Number 10

(a) Iteration setting

Accumulation

Shot Number 100
Interval time 50

☐ Grating Efficiency
Probe(pi) 0.1
every shots 1
every layers 0

☐ Save r3 every shots 1

(b) Accumulation setting

Figure 11 (a) iteration and (b) accumulation setting options

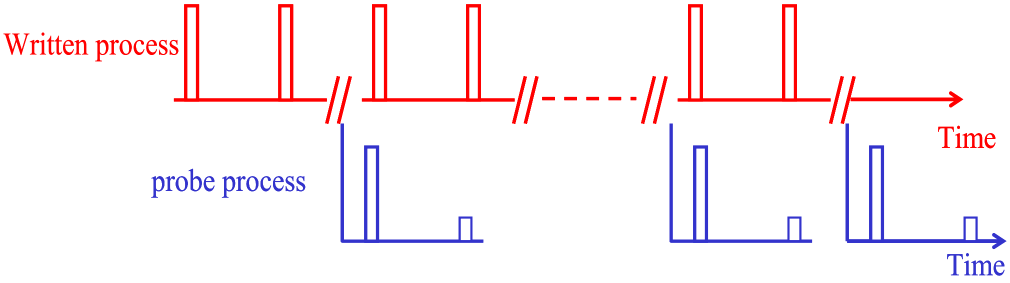

Figure 12 Writing and probing process where integration is used in S2 materials

Save Options

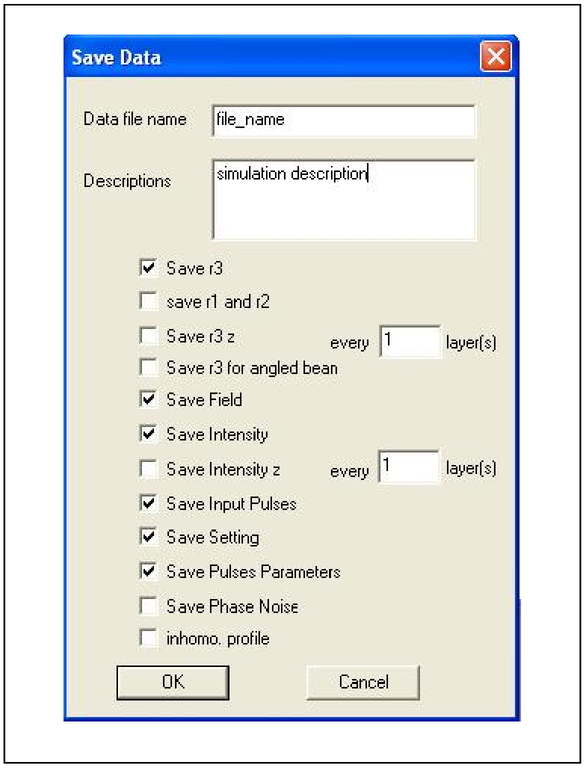

Data file name: file_name

Descriptions: simulation description

☑ Save r3
☐ save r1 and r2
☐ Save r3 z every 1 layer(s)
☐ Save r3 for angled bean
☑ Save Field
☑ Save Intensity
☐ Save Intensity z every 1 layer(s)
☑ Save Input Pulses
☑ Save Setting
☑ Save Pulses Parameters
☐ Save Phase Noise
☐ inhomo. profile

Figure 13 Save data options

As shown in Figure 13, the user can choose which results to save. Depending on the simulation type the user can choose the appropriate results he/she desires to view. For instance, if the simulation of choice is in a collinear regime, there is no need to save the population inversion (r3) for angled beam. However, if the simulation is for a thick medium, the results containing the intensity information for each layer needs to be saved for processing.

Parameters Summary

The MB simulator contains numerous parameters, but if not all of these parameters are altered, the defaulted values are used. For instance, most of the material parameters are constant because the interest is to simulate how a certain material (Tm^{3+}:YAG which is used in the lab) behaves. As it will be shown in a later chapter, the thickness of the material will be varied but the default value for most of the material parameters is otherwise used. Table 1 summarizes the most widely used parameters in the MB simulator.

Table 1 Frequently used parameter summary for the MB simulator

	Parameter		Symbol
Material	Absorption coefficient		A
	Thickness		L
	Absorption length		αL
	Population decay		T_1
	Exponential dephasing		T_2
Laser Source	Laser coherence time		T_c
Computation	Temporal	Computation time	T
		Number of points	N_t
	Spectral	Computation Bandwidth	B
		Number of points	N_s
	Spatial	Number of layers	Z
		beams	N_b
		Step	Step
Input pulses	Non-chirped pulses	Area	*
		Shape	*
		Type	*
		Width	*
	Chirped pulses	Rabi Frequency	Ω_c
		Shape	*
		Type	*
		Chirp Bandwidth	B_c
		Chirp Width	T_c
Simulations	Iteration		I
	Accumulation		J

Simulation Running and Processing Example

The MB simulator as shown in the previous section has the ability to predict the output field under various setups. Some of the parameters are usually selected to match the lab setup. For instance, the material parameters are chosen in order to match the properties of Tm^{3+}:YAG used in the lab. However, if the user wishes to investigate how other materials will affect the output, the MB simulator offers the flexibility to alter the material parameters. In this section, a simple simulation example is given in order to show the steps taken to achieve a successful simulation and how it is applied to extract the delay between the reference and the return signal.

Let's assume that it is desired to program a spatial-spectral grating into an S2 material and then probe the medium. The programming will be achieved using two brief Gaussian pulses one representing the reference signal and the second representing the return signal. As discussed earlier, accurately predicting the delay between the two pulses allows for range extraction. Though in a real scenario the return signal is attenuated, in this simulation the two pulses are set to have the same amplitude, duration, and shape. The pulses area is set to 0.001μ while the two pulses are delayed by $1\mu s$.

The geometry used in this simulation was angled beam, the reference pulse was on the -1 direction and the return pulse was on the +1 direction as depicted in Figure 14. Once the two pulses are incident on the medium they create a spatial-spectral grating with a spectral period equal to the inverse of the delay between the reference and return signal. A chirped field with a chirp rate equal to 4 MHz/μs was used to obtain the desired delay. To obtain the delay information from the output data, in the angled beam geometry case, the input field is mixed with the output echo field resulting in a beat signal containing the delay information. The beat information is then run through a Power Spectral Density (PSD) function to obtain the delay as shown in Figure 15.

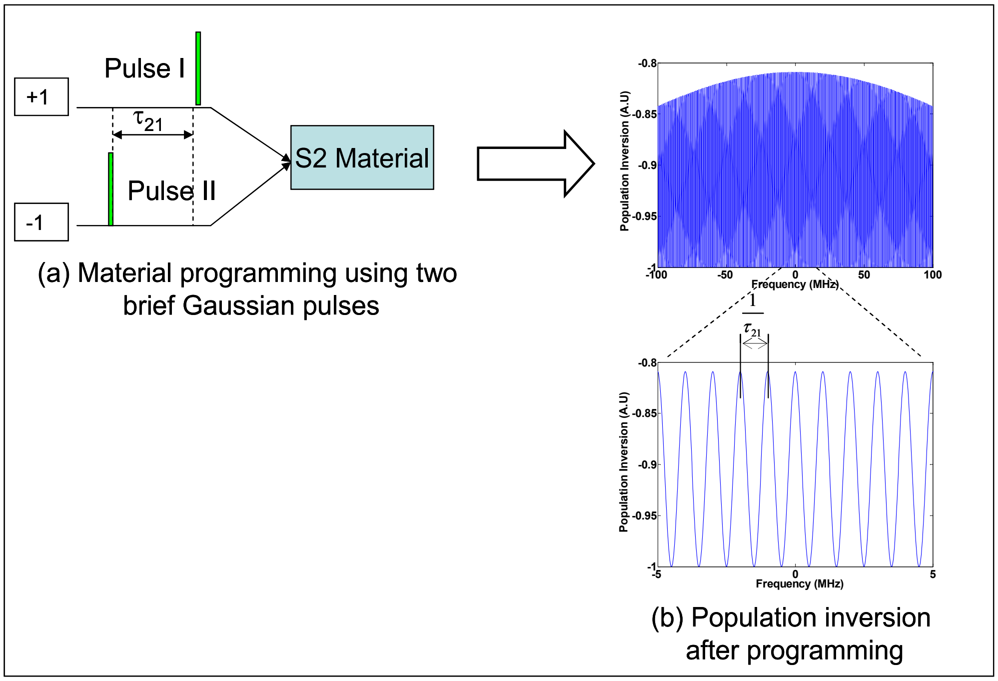

(a) Material programming using two brief Gaussian pulses

(b) Population inversion after programming

Figure 14 (a) simulation setup for programming the medium using an angled beam geometry (b) population inversion created in the medium

We should note that Figure 14 represents the writing process where two brief Gaussian pulses are used to imprint a spectral grating on the S2 material while Figure 15, relates to the readout process where the simulation setup and the results are illustrated.

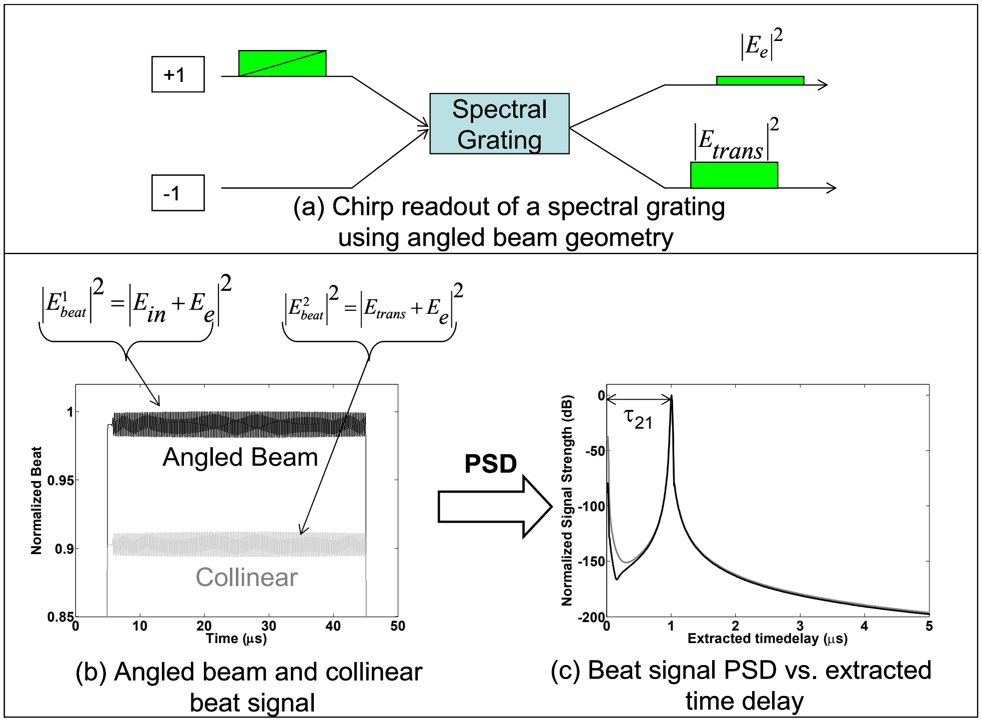

(a) Chirp readout of a spectral grating using angled beam geometry

(b) Angled beam and collinear beat signal

(c) Beat signal PSD vs. extracted time delay

Figure 15 (a) simulation readout setup (b) readout beat for angled (dark) and collinear (gray) output (c) power spectral density showing the delay peak at τ_{21}.

The computation parameters must always be carefully set. Temporal, spectral, and spatial computational settings need to be taken into account. In this example the spatial setting was not considered since the medium was assumed to be thin. The following will explain how the computational settings are taken into account.

The sample rate is defined as the number of samples per microsecond and establishes the temporal setting for the writing process. The time step is defined as the inverse of the sample rate, and the time step can be defined as: $\Delta t = \frac{\text{cycle}}{\text{\# of points}}$.

In all the simulations shown in this thesis we used a minimum of 20 points per cycle.

For the example shown above the sampling rate R_t is calculated to be 20 Ksample/sec (0.02 points/μs).

When the chirp field is involved in the readout process the temporal computational settings change. In this case, the time step is related to the chirp bandwidth B_c . The goal is to assign 20 samples to the highest frequency cycle, and, the time step $\Delta t = \frac{2}{B_c}$.

The computational time defines how far in time one wishes the simulation to run, the temporal computational time was set to 51.5 μs. The temporal number N_t can be calculated as:

$$N_t = \frac{T}{\Delta t}$$

The frequency step is defined as the inverse of the temporal computational time $\Delta\omega = \frac{1}{T}$. In the simulations presented in this thesis, the frequency step was set to $\Delta\omega = \frac{1}{5 \times T}$. Once the computational bandwidth B_{comp} is decided one can find the number of spectral points N_ω needed for the simulation:

$$N_\omega = \frac{B_{comp}}{\Delta\omega}$$

Post Simulation Analysis

In the simulations presented in this thesis, the results of interest concern extracting the delay between the transmitted and received signal. To extract the delay, the transmitted field is mixed with the generated echo field. The simulated data is processed using the Matlab code presented in Figure 16. The first few lines in the code specify the name of the file and load the data. Then the number of FFT offset points is defined and is used to eliminate unwanted data[2] and to suppress the large DC offset[3]. The number of FFT points to be used depends on the length of the original data vector to be processed. The "periodogram" function is used to estimate the power spectral density (PSD) of the data. A windowing function "Blackman" is also used to minimize the finite sampling error. Finally, the new PSD data is saved into a new file. The PSD data is then loaded and processed depending on the nature of the simulation.

Usually the data is plotted in terms of the "extracted time delay", T_e, as shown in Figure 15 (c), T_e depends on the time step, number of FFT points (N_{FFT}) used and the chirp rate as shown in the following equation:

$$T_e = \sum_{i=1}^{N} \frac{i}{N \times \Delta t \times \kappa}$$

---

[2] Since the echo field is delayed compared to the transmitted field, a part of the signal of interest is not useful and might introduce undesired artifact

[3] Because the output field had a large DC offset due to the magnitude difference between the echo and transmission field.

Where $N = \frac{N_{FFT}}{2} + 1$ and κ is the chirp rate in MHz/μs. For a spectral grating with a 1 MHz period, the PSD as a function of the extracted time delay will show a peak at 1 μs.

```
%%% Matlab Code to Load simulator Data and calculate the power spectral
%%% density of the concerned Data

%%% load the data
fname='read_pattern_SP';
totalName= strcat(fname, '_Beat');
intensityData = load(totalName);

%%% setting the FFT parameters and number of points used in the FFT
offset=200000;
fftnn=2^19;
fftN=fftnn;
k=1:fftN;
dataForfft(k)=intensityData(k+offset,1);
dataForfft=dataForfft-mean(dataForfft);

%%% plot the data desired for FFT
figure;
plot(dataForfft);

%%% plot and calculate the power spectral density of the data
figure;
periodogram(dataForfft,blackman(length(dataForfft)),fftnn);
[psdata, fftwindow]=periodogram(dataForfft,blackman(length(dataForfft)),fftnn);

%%% save the new PSD data
fnamesave=strcat(fname, '_psd1_allbeams');
save(fnamesave,'psdata', '-ASCII');


%%% calculate and save another set of data if applicable

dataForfft(k)=intensityData(k+offset,2);
dataForfft=dataForfft-mean(dataForfft);
figure;
plot(dataForfft);
figure;
periodogram(dataForfft,blackman(length(dataForfft)),fftnn);
[psdata, fftwindow]=periodogram(dataForfft,blackman(length(dataForfft)),fftnn);
fnamesave=strcat(fname, '_psd2');
save(fnamesave,'psdata', '-ASCII');
```

Figure 16 Matlab code to generate the power spectral density a desired output

CHAPTER FOUR

PROPAGATION EFFECTS

Introduction

The goal of this chapter is to study the effects of propagation in thick S2 media. The major reason behind studying propagation is related to the fact that in practice only thick media is used. Though propagation have been studied earlier [10, 11], related nonlinear effects have not been closely investigated. This chapter also tackles the impact that propagation has on different types of waveforms used to program the S2 material.

In an OCT medium the first order interaction of the medium with an optical field is described by Beer's law as discussed in detail in [1], $I = I_0 e^{-\alpha z}$, where I_0 is the input intensity of the electric field at z = 0, and z is the coordinate of propagation in the medium. Because the amount of light absorbed by the medium depends on the length of the medium L and the absorption coefficient α, an important unitless parameter is defined as the absorption length αL. The propagation effect becomes prominent when α increases which leads to inaccuracy in the approximation using Beer's Law. The coupled Maxwell-Bloch equations become necessary to accurately predict the effects of propagation in OCT processes.

To closely study the nonlinear effects of propagation, a first set of simulations considered programming a single delay in the S2 media using brief Gaussian pulses.

Programming a single delay enabled us to study harmonics separately from intermodulation caused by interference present when multiple delays are used in programming. In current radar systems, coded waveforms are used to increase the processing gain. Therefore, two types of simulations involving coded waveforms were studied, one involving temporally overlapped and the other non-overlapped coded waveforms.

The absorption length considered in this chapter is in the order of 2 and 20 steps were used in the calculations. The propagation effects were analyzed in terms of signal peak, noise level, and thus dynamic range.

Single Delay Using Brief Gaussian Pulses

Simulation Settings

In this set of simulations, two brief Gaussian pulses 1μs apart were used to program the medium and a chirped field was used to probe it. In addition to varying the absorption coefficient and the number of spatial calculation steps, the input pulse area and the readout chirp Rabi frequency were varied. Table 2 shows the simulation parameters for programming and probing the medium and Table 3 shows the values assigned to the varying input pulse area A_{in} and the readout chirped pulse Rabi frequency Ω_c.

Table 2 Summery of the parameters setting for single delay propagation simulation

	Parameters		Symbol	Value
Material	Absorption coefficient		α	$100\ \mathrm{m}^{-1}$
	Thickness		L	0.02 m
	Absorption length		αL	2
Computation	Temporal	Computation time	T	45 μs
		Number of points	N_t	110000
	Spectral	Computation Bandwidth	B	100 MHz
		Number of points	N_s	10000
	Spatial	Number of layers	Z	20
Input pulses	Programming pulses	Area	*	0.001μ
		Shape	*	G
		Type	*	N
		Width	*	0.01 μs
	Readout pulse	Rabi Frequency	Ω_c	0.0001
		Shape	*	S/C
		Type	*	C
		Chirp Bandwidth	*	160 MHz
		Chirp Width	*	40 μs

The non-uniform computational setting was used in this simulation. The simulation temporal computation time was divided into two sections. The first section contained the two programming pulse, the computation time section was set to 1.5 μs and the number of temporal points was calculated to be 10,000 points. The second section contained the readout chirped field where the computation time was set to 43.5 μs with 100,000 points.

Table 3 Values assigned to A_{in} and Ω_c

Input pulse area*μ (A_{in})	Readout Rabi Frequency, Ω_c (MHz)
0.001	0.0001
0.01	0.001
0.025	0.01
0.05	0.1
0.1	

Simulation Results

The results that follow were obtained using the Matlab code shown in Figure 16, the number of FFT points, N_{FFT}, used was 2^16 and the number of offset points, N_{offset}, was 25000 points (about 10.9 μs temporal shift) to process the desired data only. Figure 17 depicts how the readout Rabi frequency and the input pulse area affect the readout signal. Figure 17 (a) and (b), and Figure 17 (c) and (d) show how the noise floor rises as the readout Rabi frequency increases, and, Figure 17 (a) and (c) and Figure 17 (b) and (d), show the rise of harmonics as the input pulse area increases.

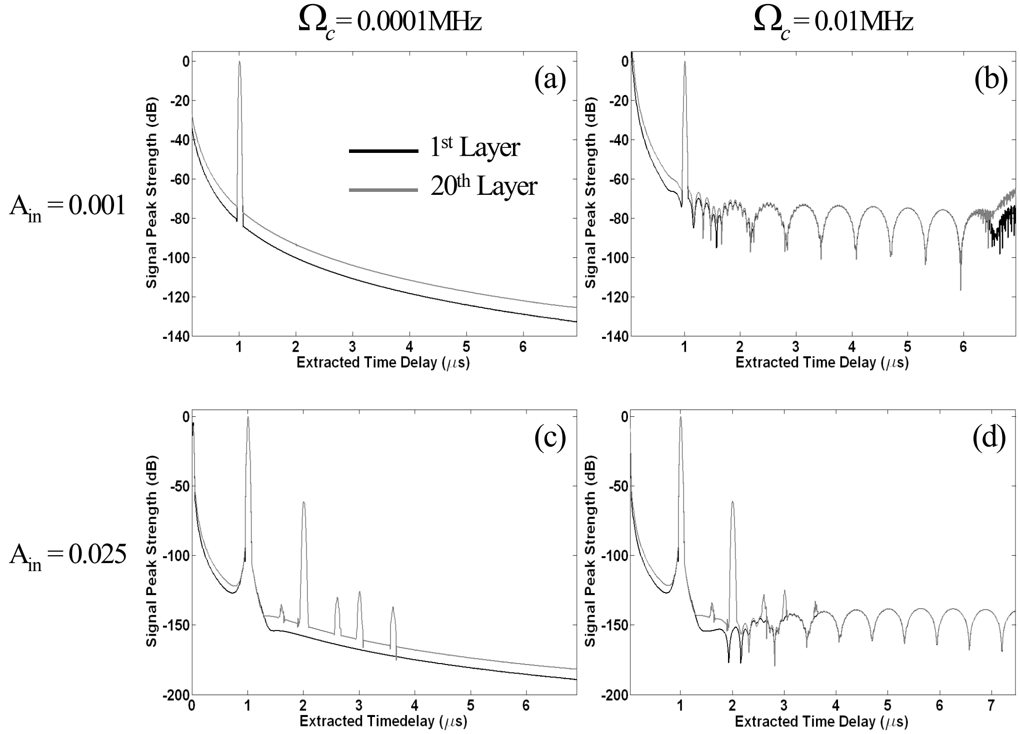

Figure 17 Effect of readout Rabi Frequency and the input pulse area on output signal in a thick medium. (a) Rabi frequency 0.1kHz, pulse area 0.001π. (b) Rabi frequency 10kHz, pulse area 0.001π. (c) Rabi frequency 0.1kHz, pulse area 0.025π. (d) Rabi frequency 10kHz, pulse area 0.025π

Figure 18 shows how, for a fixed readout Rabi frequency, the change in input pulse area affects the principal, the 2^{nd} order harmonic peaks, the dynamic range (principal peak to noise ratio), and the spur free dynamic range ratio(principal peak to the highest spur). The noise level was obtained by taking the mean value from 2.5 μs to 4 μs of the extracted time delay.

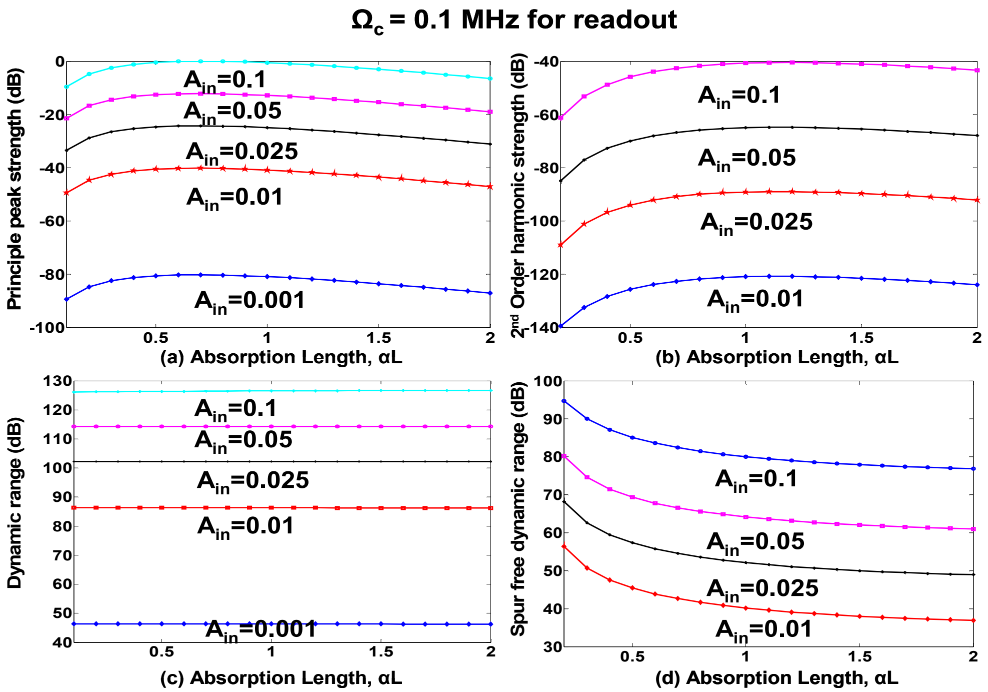

Figure 18 Input pulse area variation and its effect on the (a) 1st order peak, (b) 2nd order peak, (c) dynamic range (d) spur free dynamic range

In this case, the results indicate that as the input pulse area or readout chirp Rabi frequency increases (which corresponds to the programming and probing pulses intensity), harmonics start to appear as the signal propagates through the thick medium as shown in Figure 17. In addition and as depicted in Figure 18 (a), the first order peak or the principal peak maximizes at a certain thickness which in this particular case corresponds to an absorption length of 0.6. The second order peak on the other hand maximizes at a different absorption length which corresponds to about 1.2 of the absorption length as seen in Figure 18 (b). The peak to the noise level ratio illustrated in Figure 18 (c) appeared to be constant throughout the absorption length, indicating that the length of the medium does not affect the peak to noise ratio in this particular case. Figure 18 (d) depicts the principal peak to the second order harmonic peak, showing that the ratio deceases as the absorption length increases, indicating that the second order peak manifests more rapidly then the principal peak.

Single Delay Using Non-Overlapped Coded Waveforms

Simulation Setting

In this section, rather then programming the medium with brief Gaussian pulses, two non-overlapped coded waveforms has been used to program the grating and a chirped field was used to probe the medium as depicted in Figure 19. The use of brief pulses in a radar application is not common, long coded waveforms are used instead to increase processing gain. The pulses used in this simulation are 1.2 μs apart and contain 1000 bits where each bit has a width of 0.001 μs, therefore the total length of the pulse is 1 μs. The coding was achieved using a random BPSK sequence and both pulses contain the same random bit sequence. The parameter settings are summarized in Table 4.

Non-uniform setting has been applied to this simulation, where the temporal computational time has been divided into two sections, the first section includes the programming pulses and the computational time was 3 μs long while the number of points was 60,000 points, the second section contained the readout pulses and the computed time scale was 52 μs long while the number of points was set to 100,000 points.

Table 4 Summary of the parameters setting for single delay propagation simulation (pulse non-overlapped patterns)

	Parameters		Symbol	Value
Material	Absorption coefficient		α	$100\ m^{-1}$
	Thickness		L	0.02 m
	Absorption length		αL	2
Computation	Temporal	Computation time	T	55 μs
		Number of points	N_t	160000
	Spectral	Computation Bandwidth	B	100 MHz
		Number of points	N_s	55000
	Spatial	Number of layers	Z	20
Input pulses	Programming pulses	Area per bit	*	0.0025
		Shape	*	P (pattern)
		Type	*	S (square)
		Width (for a single bit)	*	0.001 μs
		Number of bits	*	1000
	Readout pulse	Rabi Frequency	Ω_c	0.0001
		Shape	*	S/C
		Type	*	C
		Chirp Bandwidth	*	160 MHz
		Chirp Width	*	40 μs

The first and second programming pulses used for programming contain the same random bit sequence. Figure 19 depicts the simulation setup, the figure in the right hand side illustrates the PSD output versus the extracted time delay. The number of FFT points used to calculate the PSD was 2^16. Three regions of interest have been defined, the signal peak, the sidelobe region, and the noise floor region. The sidelobe region is generated from the envelope created by the random pattern on top of the principal grating. In theory, the peak to sidelobe ratio is proportional to the number of bits used in the sequence. However, the peak to sidelobe ratio is also dependent on the type of sequence used and the signal to sidelobe ratio can vary significantly depending on the type of codes used.

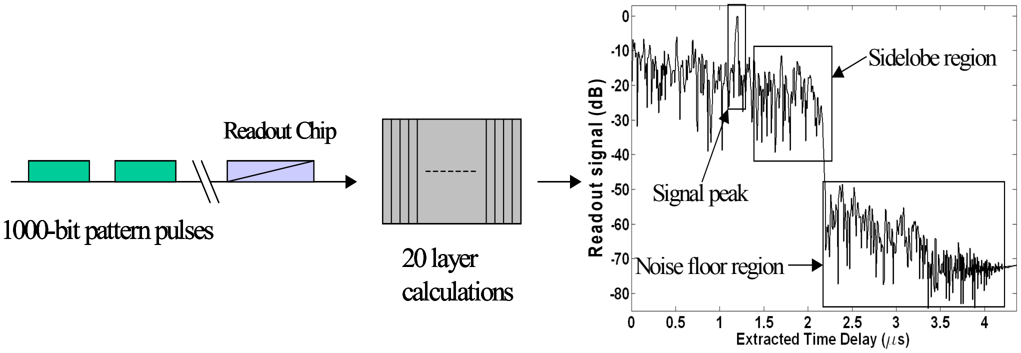

Figure 19 Simulation setup for propagation of a patterned pulse in a tick medium, the right-hand side of the figure shows the PSD of the output intensity at layer 3. Three distinct areas of interest can be defined, the signal peak, the sidelobe, and the noise floor

Simulation Results

The signal peak strength and the behavior of the sidelobe level and the noise level versus the absorption length, αL, are depicted in Figure 20 (a), (b), and (c) respectively. The sidelobe value was calculated as the mean of the values from 1.3 μs to 2.0 μs of the extracted time delay and the noise value was calculated as the mean of the values from 2.5 μs to 4 μs of the extracted time delay.

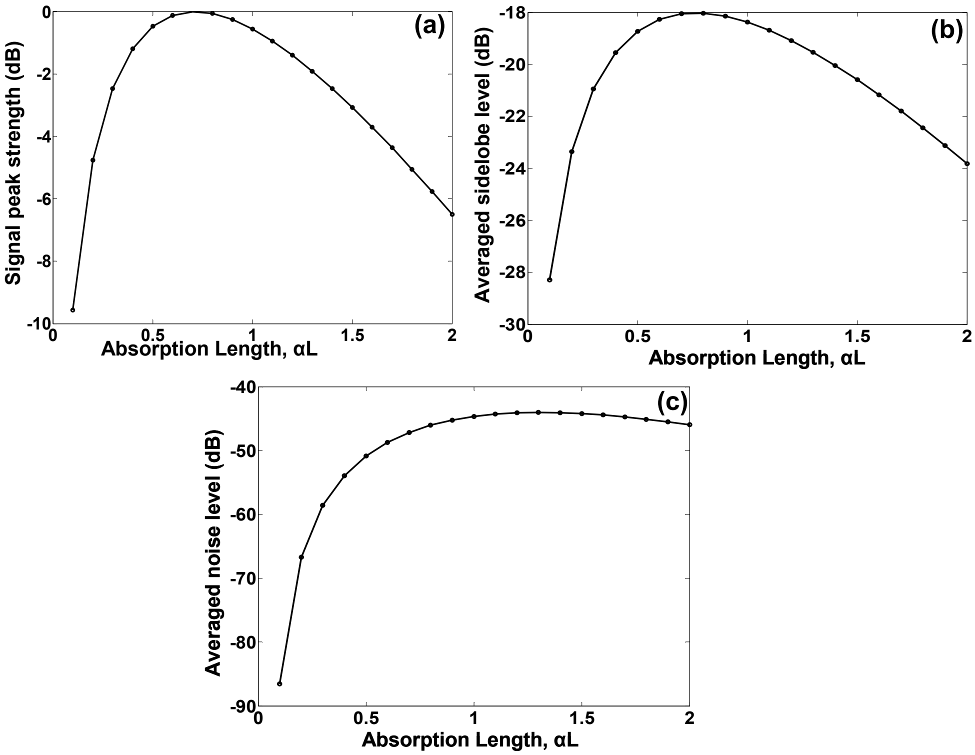

Figure 20 (a) signal peak, (b) sidelobe and (c) noise floor behavior as the signal propagates through the medium

Figure 21 shows the dynamic range of the output signal, Figure 21 (a) depicts the peak to sidelobe ratio and Figure 21 (b) illustrates the peak to the averaged noise floor.

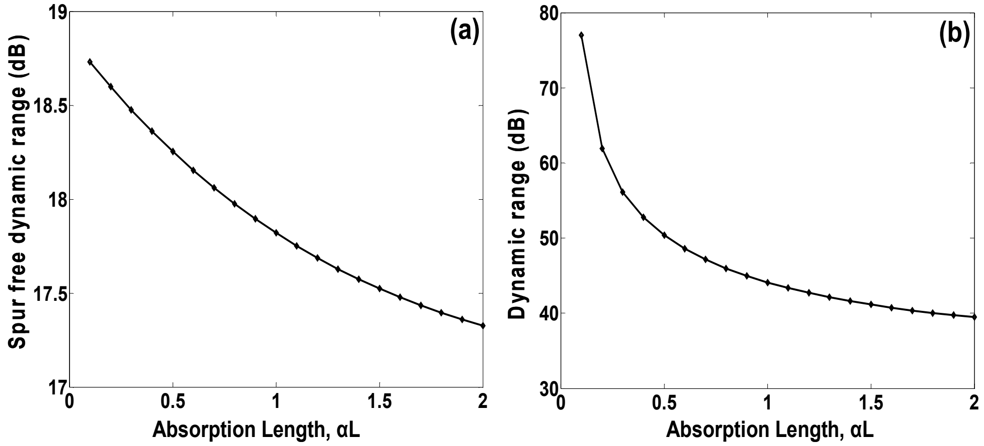

Figure 21 Spur free dynamic range and dynamic range behavior throughout the medium (a) spur free dynamic range vs. absorption length (b) dynamic range vs. absorption length

Figure 20 (a) shows that the peak strength is maximized at an absorption length of 0.7, there is also a 10 dB improvement compared to an absorption length of 0.1. The average sidelobe level, shown in Figure 20 (b), maximizes at an absorption length of 0.7 with a 10 dB improvement. Comparing the two figures, we notice that the peak and averaged sidelobe levels behave similarly as the signal propagates through the thick medium. The noise floor, on the other hand, maximizes at a different absorption length which impacts the signal to noise ratio as shown in Figure 21 (b). The dynamic range when patterned pulses are used tends to deteriorate as the length of the medium increases. The spur free dynamic range as shown in Figure 21 (a) varies as the absorption length increases but the variation is in the order of about 1dB.

Single Delay Using Overlapped Pulses

Simulation Setting

In this section, overlapped coded waveforms are investigated. Two pulses, 2 μs long and 1μs apart, containing 2000 random bits have been used to program that medium, a chirped field has been used to probe the grating. The simulation settings are summarized in Table 5. The non-uniform setting has been used here as well, the first section includes the programming pulses and the computational time was 3.5 μs long while the number of points was 70,000 points, the second section contained the readout pulses and the computational time was 52 μs long while the number of points was set to 100,000 points. The number of FFT points used to calculate the PSD was 2^16.

Table 5 Summery of the parameters setting for single delay propagation simulation (pulse overlapped patterns)

	Parameters		Symbol	Value
Material	Absorption coefficient		A	100 m^{-1}
	Thickness		L	0.02 m
	Absorption length		αL	2
Computation	Temporal	Computation time	T	55 μs
		Number of points	N_t	170000
	Spectral	Computation Bandwidth	B	100 MHz
		Number of points	N_s	55000
	Spatial	Number of layers	Z	20
Input pulses	Programming pulses	Area per bit	*	0.0025
		Shape	*	P (pattern)
		Type	*	S (square)
		Width (for a single bit)	*	0.001 μs
		Number of bits	*	2000
	Readout pulse	Rabi Frequency	Ω_c	0.0001
		Shape	*	S/C
		Type	*	C
		Chirp Bandwidth	*	160 MHz
		Chirp Width	*	40 μs

Simulation Results

The simulation results are given in Figure 22 and Figure 23. Figure 22 (a), (b), and (c) depict the behavior of the signal peak, sidelobe, and noise floor in terms of the medium thickness respectively. The sidelobe value was calculated as the mean of the values from 1.2 μs to 2.8μs, the noise floor was calculated as the mean of the value from 3.5 μs to 5 μs.

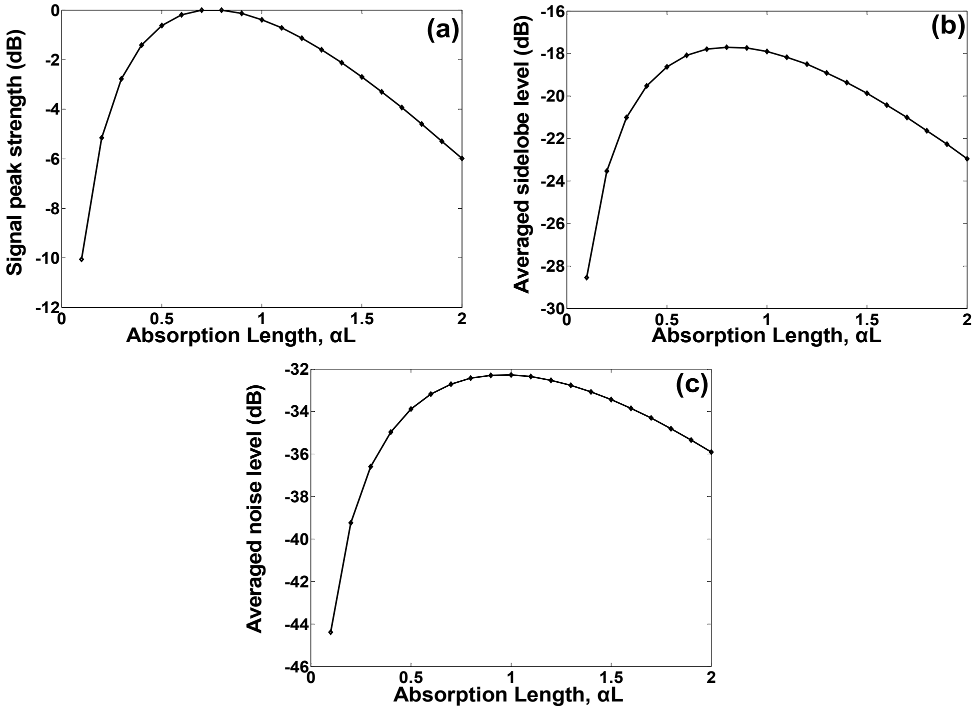

Figure 22 Dynamic range behavior throughout the medium (a) signal peak to sidelobe level, (b) signal peak to averaged noise level.

The signal peak relative to the noise floor and the signal peak relative to the sidelobe level vs. the medium thickness are shown in Figure 22 and Figure 23 respectively.

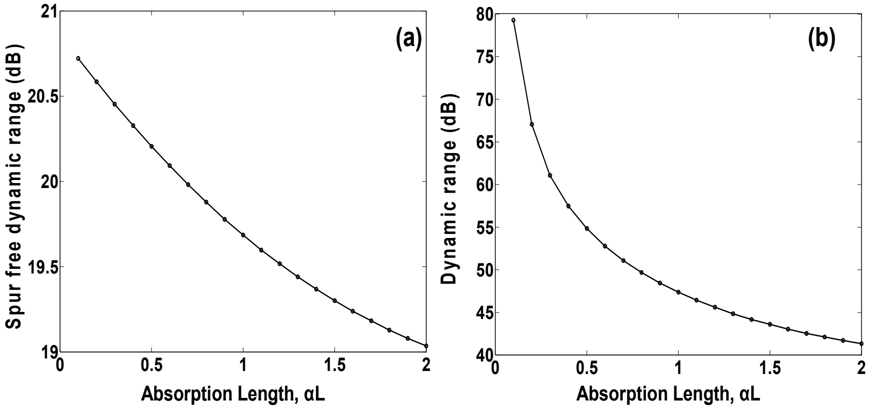

Figure 23 Dynamic range behavior throughout the medium (a) signal peak to sidelobe level, (b) signal peak to averaged noise level.

From the results shown above, the dynamic range decreases as the absorption length increases. Comparing the spur free dynamic range for the overlapped and non-overlapped case, we note that the overlapped case shows a better spur free dynamic range, an improvement of 3dB. This is due to the fact that 2000 bit patterns were used in the overlapped case compared to 1000 bit patterns in the non-overlapped case.

Results Summary and Discussion

The overall goal of this chapter was to investigate the propagation effects on the OCT process. The results show that for any type of waveform used, there is an optimum absorption length where the output signal maximizes. In addition, the simulation results show that the dynamic range and the spur free dynamic range tend to degrade as the absorption length increases. The DR showed a significant drop of about 40 dB from the $\alpha L = 0.1$ to $\alpha L = 2$, and the FSDR showed a drop of about 1.3 dB when 1000 bit sequence was used and 1.7 dB drop when 2000 bit sequence was used. The results also proved that the length of the codes used affects the SFDR, when using 1000 bit and 2000 bits, a 3 dB SFDR improvement was achieved.

The SFDR presented in this chapter appear to be low and does not show the real value achieved in the lab environment. The first reason is that in the simulation the longest bit sequence was 2000 bits long and the choice was constrained by the computational time. Using longer sequences will improve the SFDR. Also, a random coded sequence was used but in the lab agile coding sequences are used to achieve a better SFDR. Coding sequences such as the complimentary codes and maximum length sequences offer a better sidelobe cancellation [7]. Furthermore, integration was not used the simulation, integration is common in the field of Radar and up to 500 shots have been used in the lab by our group to improve processing gain.

CHAPTER FIVE

INTERFERENCE AND CROSS TALK IN A MULTIPLE DELAY CASE

Interference and cross talk are important phenomena to consider when multiple signals are processed. In radar, the field reflected from the object is detected in the form of multiple returns. In this chapter we study how these multiple signals interfere with each other and how they affect the readout process.

A calculation of interference and cross talk pertaining to two delay scenario is presented. Both collinear beam and angled beam geometries are investigated. The studied scenario is depicted in Figure 24, where three brief Gaussian pulses are used to program the medium and a frequency chirped pulse is used to probe the medium. In the programming, the first pulse is considered as the reference and the two other pulses are considered as the returns.

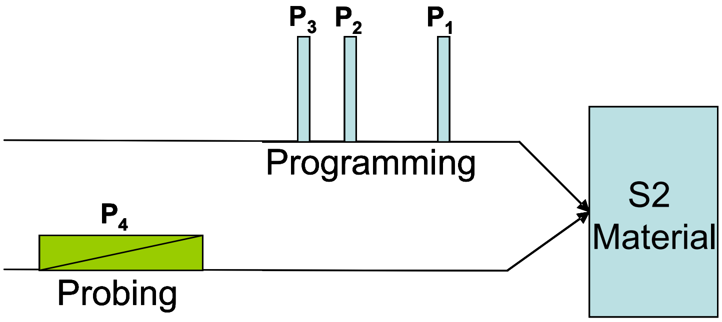

Figure 24 Programming and probing the S2 material using three brief Gaussian pulses P_1, P_2, and P_3, to program the medium and a chirped field P_4 to probe the medium

Introduction to Multiple delay Programming and Probing

When more then two pulses are used to program the S2 material, a multitude of gratings with different periods are imprinted. Let's take the case where three pulses are used to program the medium, where the first pulse is used as the reference and the other two pulses are used as the returns. As depicted in Figure 25 the gratings imprinted in the S2 material depend on the temporal position of the pulses used. The pulse at time t_1 and the one at t_2 create a grating with a period (or delay[4]) $\tau_1 = t_2 - t_1$. The pulses at t_1 and t_3 create a grating with a period $\tau_2 = t_3 - t_1$. In addition, a grating with a period $\tau_3 = t_3 - t_2 = \tau_2 - \tau_1$ is imprinted in the medium. Finally, another grating with delay $2\tau_2 - \tau_1$ or $2\tau_1 - \tau_2$ is generated depending of the position of the pulses in the time scale.

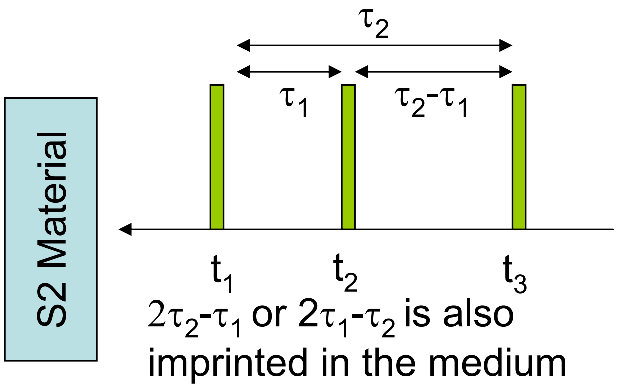

Figure 25 Programming the S2 material using three pulses generates 4 grating with different periods

---

[4] After the grating is readout and the PSD function is used, the delay manifests as a delay peak at a time that is equal the inversed period of the grating. That is why the term period and delay are used interchangeably in this case.

When a frequency chirped field is incident on the medium it interferes with the programmed grating, and at the output, a transmitted field E_T along with echo fields is generated. When mixing the transmission field with different echo fields or mixing echo fields against each other, the resulting beat signal contains the features of the spectral grating present in the medium. However, echo fields manifest at different times, thus, beating a transmission field with an echo field at a particular time will result in a beat signal that contains the delay at which that echo manifested. In this section the intermodulations will be discussed in terms of delays rather then frequencies. To define the order of each delay, one needs to find out what fields contribute to which delay. The calculation that follows answers that question.

Calculations

This calculation pertains to a two-delay scenario, three pulses write the grating where one acts as the reference and the other two as the returns. The grating is read out using a frequency chirped field. The output field E_{out} is composed of the transmitted chirped field E_T, and the echo fields E_{τ_1}, E_{τ_2}, E_{τ_3}, E_{τ_4}. The goal of this calculation is to obtain the magnitude and phase for the mixed fields.

The chirped field can be represented as:

$E_T = \exp\left[i\left(\omega_s t + \frac{1}{2}\kappa t^2\right)\right]$, when delayed by a time τ_p it becomes:

$E_T = \exp\left[i\left(\omega_s (t-\tau_p) + \frac{1}{2}\kappa (t-\tau_p)^2\right)\right]$, where τ_p = 1, 2, 3, or 4.

The first calculation concerns mixing the transmission field with the echo field E_{τ_1} :

Beating E_T with E_{τ_1} :

$$
\begin{aligned}
\left|E_T + E_{\tau_1}\right|^2 &= E_T E_{\tau_1}{}^* + E_T{}^* E_{\tau_1} \\
&= \left|E_T E_{\tau_1}\right| \exp\left[i\left(\omega_s t + \frac{1}{2}\kappa t^2 \right)\right] * \exp\left[-i\left(\omega_s (t-\tau_1) + \frac{1}{2}\kappa (t-\tau_1)^2 \right)\right] \\
&\quad + \left|E_T E_{\tau_1}\right| \exp\left[-i\left(\omega_s t + \frac{1}{2}\kappa t^2 \right)\right] * \exp\left[i\left(\omega_s (t-\tau_1) + \frac{1}{2}\kappa (t-\tau_1)^2 \right)\right] \\
&= \left|E_T E_{\tau_1}\right| \exp\left[\mathrm{i}\omega_s t + \frac{i}{2}\kappa t^2 - i\omega_s t + i\omega_s \tau_1 - \frac{i}{2}\kappa t^2 + i\kappa \tau_1 t - \frac{i}{2}\kappa \tau_1{}^2 \right] \\
&\quad + \left|E_T E_{\tau_1}\right| \exp\left[\text{-i}\omega_s t - \frac{i}{2}\kappa t^2 + i\omega_s t - i\omega_s \tau_1 + \frac{i}{2}\kappa t^2 - i\kappa \tau_1 t + \frac{i}{2}\kappa \tau_1{}^2 \right] \\
&= \left|E_T E_{\tau_1}\right| \exp\left[i\left(\kappa \tau_1 t + \omega_s \tau_1 - \frac{1}{2}\kappa \tau_1{}^2 \right)\right] \\
&\quad + \left|E_T E_{\tau_1}\right| \exp\left[-i\left(\kappa \tau_1 t + \omega_s \tau_1 - \frac{1}{2}\kappa \tau_1{}^2 \right)\right] \\
&= 2\left|E_T E_{\tau_1}\right| \cos\left(\kappa \tau_1 t + \omega_s \tau_1 - \frac{1}{2}\kappa \tau_1{}^2 \right)
\end{aligned}
$$

From the calculations, we see that the period of the cosine wave is $T_1 = \frac{1}{\kappa \tau_1}$ and the phase

$$\theta = \omega_s \tau_1 - \frac{1}{2}\kappa \tau_1^2$$

The same calculation applies when the transmitted field mixes with the other echo fields, resulting in:

$$\left|E_T+E_{\tau_2}\right|^2=2\left|E_TE_{\tau_2}\right|\cos\left(\kappa\tau_2t+\omega_s\tau_2-\frac{1}{2}\kappa\tau_2{}^2\right)$$

$$\left|E_T+E_{\tau_3}\right|^2=2\left|E_TE_{\tau_3}\right|\cos\left(\kappa\tau_3t+\omega_s\tau_3-\frac{1}{2}\kappa\tau_3{}^2\right)\text{ where }\tau_3=\left|\tau_2-\tau_1\right|$$

$$\left|E_T+E_{\tau_4}\right|^2=2\left|E_TE_{\tau_4}\right|\cos\left(\kappa\tau_4t+\omega_s\tau_4-\frac{1}{2}\kappa\tau_4{}^2\right)\text{ where }\tau_4=\left|2\tau_1-\tau_2\right|$$

Now we calculate the beat of two ***echoes mixing with each other***:

$$\begin{aligned}
\left|E_{\tau_1}+E_{\tau_2}\right|^2&=E_{\tau_1}E_{\tau_2}{}^*+E_{\tau_1}{}^*E_{\tau_2}\\
&=\left|E_{\tau_1}E_{\tau_2}\right|\exp\left[i\left(\omega_s(t-\tau_1)+\frac{1}{2}\kappa(t-\tau_1)^2\right)\right]*\exp\left[-i\left(\omega_s(t-\tau_2)+\frac{1}{2}\kappa(t-\tau_2)^2\right)\right]\\
&\quad+\left|E_{\tau_1}E_{\tau_2}\right|\exp\left[-i\left(\omega_s(t-\tau_1)+\frac{1}{2}\kappa(t-\tau_1)^2\right)\right]*\exp\left[i\left(\omega_s(t-\tau_2)+\frac{1}{2}\kappa(t-\tau_2)^2\right)\right]\\
&=\left|E_{\tau_1}E_{\tau_2}\right|\exp\left[i\omega_st-i\omega_s\tau_1+\frac{i}{2}\kappa t^2-i\kappa t\tau_1+\frac{i}{2}\kappa\tau_1{}^2-i\omega_st+i\omega_s\tau_2-\frac{i}{2}\kappa t^2+i\kappa t\tau_1-\frac{i}{2}\kappa\tau_1{}^2\right]\\
&\quad+\left|E_{\tau_1}E_{\tau_2}\right|\exp\left[-i\omega_st+i\omega_s\tau_1-\frac{i}{2}\kappa t^2+i\kappa t\tau_1-\frac{i}{2}\kappa\tau_1{}^2+i\omega_st-i\omega_s\tau_2+\frac{i}{2}\kappa t^2-i\kappa t\tau_1+\frac{i}{2}\kappa\tau_1{}^2\right]\\
&=\left|E_{\tau_1}E_{\tau_2}\right|\exp\left[i\left\{\kappa(\tau_2-\tau_1)t+\omega_s(\tau_2-\tau_1)-\frac{1}{2}\kappa(\tau_2{}^2-\tau_1{}^2)\right\}\right]\\
&\quad+\left|E_{\tau_1}E_{\tau_2}\right|\exp\left[-i\left\{\kappa(\tau_2-\tau_1)t+\omega_s(\tau_2-\tau_1)-\frac{1}{2}\kappa(\tau_2{}^2-\tau_1{}^2)\right\}\right]\\
&=\left|E_{\tau_1}E_{\tau_2}\right|\cos\left(\kappa(\tau_2-\tau_1)t+\omega_s(\tau_2-\tau_1)-\frac{1}{2}\kappa(\tau_2{}^2-\tau_1{}^2)\right)
\end{aligned}$$

The same calculation applies for the other echoes mixing:

$$\begin{aligned}
\left|E_{\tau_1}+E_{\tau_3}\right|^2&=\left|E_{\tau_1}E_{\tau_3}\right|\cos\left(\kappa(\tau_1-\tau_3)t+\omega_s(\tau_1-\tau_3)-\frac{1}{2}\kappa(\tau_1{}^2-\tau_3{}^2)\right),\text{ since }\tau_3=\tau_2-\tau_1\\
&=\left|E_{\tau_1}E_{\tau_3}\right|\cos\left(\kappa(\tau_1-(\tau_2-\tau_1))t+\omega_s(\tau_1-(\tau_2-\tau_1))-\frac{1}{2}\kappa(\tau_1{}^2-(\tau_2-\tau_1)^2)\right)\\
&=\left|E_{\tau_1}E_{\tau_3}\right|\cos\left(\kappa(2\tau_1-\tau_2)t+\omega_s(2\tau_1-\tau_2)-\frac{1}{2}\kappa(2\tau_1\tau_2-\tau_2{}^2)\right)
\end{aligned}$$

$$\begin{aligned}
\left|E_{\tau_1}+E_{\tau_4}\right|^2&=\left|E_{\tau_1}E_{\tau_4}\right|\cos\left(\kappa(\tau_1-\tau_4)t+\omega_s(\tau_1-\tau_4)-\frac{1}{2}\kappa(\tau_1{}^2-\tau_4{}^2)\right),\text{ since }\tau_4=2\tau_1-\tau_2\\
&=\left|E_{\tau_1}E_{\tau_4}\right|\cos\left(\kappa(\tau_1-(2\tau_1-\tau_2))t+\omega_s(\tau_1-(2\tau_1-\tau_2))-\frac{1}{2}\kappa(\tau_1{}^2-(2\tau_1-\tau_2)^2)\right)\\
&=\left|E_{\tau_1}E_{\tau_3}\right|\cos\left(\kappa(\tau_2-\tau_1)t+\omega_s(\tau_2-\tau_1)-\frac{1}{2}\kappa(-3\tau_1{}^2+4\tau_1\tau_2-\tau_2{}^2)\right)
\end{aligned}$$

$$\left|E_{\tau_2}+E_{\tau_4}\right|^2=\left|E_{\tau_2}E_{\tau_4}\right|\cos\left(\kappa(\tau_2-\tau_4)t+\omega_s(\tau_2-\tau_4)-\frac{1}{2}\kappa({\tau_2}^2-{\tau_4}^2)\right),\text{ since }\tau_4=2\tau_1-\tau_2$$

$$=\left|E_{\tau_1}E_{\tau_4}\right|\cos\left(\kappa(\tau_2-(2\tau_1-\tau_2))t+\omega_s(\tau_2-(2\tau_1-\tau_2))-\frac{1}{2}\kappa({\tau_2}^2-(2\tau_1-\tau_2)^2)\right)$$

$$=\left|E_{\tau_1}E_{\tau_4}\right|\cos\left(\kappa(\tau_3)t+\omega_s(\tau_3)-\frac{1}{2}\kappa(4\tau_1\tau_2-4{\tau_1}^2)\right)\text{ since }\tau_3=\tau_2-\tau_1$$

$$\left|E_{\tau_2}+E_{\tau_3}\right|^2=\left|E_{\tau_2}E_{\tau_3}\right|\cos\left(\kappa(\tau_2-\tau_3)t+\omega_s(\tau_2-\tau_3)-\frac{1}{2}\kappa({\tau_2}^2-{\tau_3}^2)\right),\text{ since }\tau_3=\tau_2-\tau_1$$

$$=\left|E_{\tau_2}E_{\tau_3}\right|\cos\left(\kappa(\tau_2-(\tau_2-\tau_1))t+\omega_s(\tau_2-(\tau_2-\tau_1))-\frac{1}{2}\kappa({\tau_2}^2-(\tau_2-\tau_1)^2)\right)$$

$$=\left|E_{\tau_2}E_{\tau_3}\right|\cos\left(\kappa(\tau_1)t+\omega_s(\tau_1)-\frac{1}{2}\kappa(2\tau_1\tau_2-{\tau_1}^2)\right)$$

$$\left|E_{\tau_3}+E_{\tau_4}\right|^2=\left|E_{\tau_3}E_{\tau_4}\right|\cos\left(\kappa(\tau_3-\tau_4)t+\omega_s(\tau_3-\tau_4)-\frac{1}{2}\kappa({\tau_3}^2-{\tau_4}^2)\right),\text{ since }\tau_3=\tau_2-\tau_1\text{ and }\tau_4=2\tau_1-\tau_2$$

$$=\left|E_{\tau_3}E_{\tau_4}\right|\cos\left(\kappa((\tau_2-\tau_1)-(2\tau_1-\tau_2))t+\omega_s((\tau_2-\tau_1)-(2\tau_1-\tau_2))-\frac{1}{2}\kappa((\tau_2-\tau_1)^2-(2\tau_1-\tau_2)^2)\right)$$

$$=\left|E_{\tau_3}E_{\tau_4}\right|\cos\left(\kappa(\tau_3)t+\omega_s(\tau_3)-\frac{1}{2}\kappa(2\tau_1\tau_2-3{\tau_1}^2)\right)$$

At this point, the fields contributing to different delays are known and summarized for the collinear and the angled beam geometry:

Summary (collinear)

Delay τ_1:

$$\left|E_T+E_{\tau_1}\right|^2=2\left|E_TE_{\tau_1}\right|\cos\left(\kappa\tau_1t+\omega_s\tau_1-\frac{1}{2}\kappa{\tau_1}^2\right)$$

$$\left|E_{\tau_2}+E_{\tau_3}\right|^2=\left|E_{\tau_2}E_{\tau_3}\right|\cos\left(\kappa(\tau_1)t+\omega_s(\tau_1)-\frac{1}{2}\kappa(2\tau_1\tau_2-{\tau_1}^2)\right)$$

Delay τ_2:

$$\left|E_T + E_{\tau_2}\right|^2 = 2\left|E_T E_{\tau_2}\right|\cos\left(\kappa\tau_2 t + \omega_s\tau_2 - \frac{1}{2}\kappa\tau_2{}^2\right)$$

Delay $\tau_2 - \tau_1$:

$$\left|E_T + E_{\tau_3}\right|^2 = 2\left|E_T E_{\tau_3}\right|\cos\left(\kappa\tau_3 t + \omega_s\tau_3 - \frac{1}{2}\kappa\tau_3{}^2\right)$$

$$\left|E_{\tau_1} + E_{\tau_2}\right|^2 = \left|E_{\tau_1} E_{\tau_2}\right|\cos\left(\kappa(\tau_2 - \tau_1)t + \omega_s(\tau_2 - \tau_1) - \frac{1}{2}\kappa(\tau_2{}^2 - \tau_1{}^2)\right)$$

$$\left|E_{\tau_1} + E_{\tau_4}\right|^2 = \left|E_{\tau_1} E_{\tau_3}\right|\cos\left(\kappa(\tau_2 - \tau_1)t + \omega_s(\tau_2 - \tau_1) - \frac{1}{2}\kappa(-3\tau_1{}^2 + 4\tau_1\tau_2 - \tau_2{}^2)\right)$$

Delay $2\tau_1 - \tau_2$:

$$\left|E_T + E_{\tau_4}\right|^2 = 2\left|E_T E_{\tau_4}\right|\cos\left(\kappa\tau_4 t + \omega_s\tau_4 - \frac{1}{2}\kappa\tau_4{}^2\right)$$

$$\left|E_{\tau_1} + E_{\tau_3}\right|^2 = \left|E_{\tau_1} E_{\tau_3}\right|\cos\left(\kappa(2\tau_1 - \tau_2)t + \omega_s(2\tau_1 - \tau_2) - \frac{1}{2}\kappa(2\tau_1\tau_2 - \tau_2{}^2)\right)$$

Summary (angled beam)

Delay τ_1:

$$\left|E_T + E_{\tau_1}\right|^2 = 2\left|E_T E_{\tau_1}\right|\cos\left(\kappa\tau_1 t + \omega_s\tau_1 - \frac{1}{2}\kappa\tau_1{}^2\right)$$

Delay τ_2:

$$\left|E_T + E_{\tau_2}\right|^2 = 2\left|E_T E_{\tau_2}\right|\cos\left(\kappa\tau_2 t + \omega_s\tau_2 - \frac{1}{2}\kappa\tau_2{}^2\right)$$

Delay $\tau_2 - \tau_1$:

$$\left|E_T + E_{\tau_3}\right|^2 = 2\left|E_T E_{\tau_3}\right|\cos\left(\kappa\tau_3 t + \omega_s\tau_3 - \frac{1}{2}\kappa\tau_3{}^2\right)$$

$$\left|E_{\tau_1} + E_{\tau_2}\right|^2 = \left|E_{\tau_1} E_{\tau_2}\right|\cos\left(\kappa(\tau_2 - \tau_1)t + \omega_s(\tau_2 - \tau_1) - \frac{1}{2}\kappa(\tau_2{}^2 - \tau_1{}^2)\right)$$

Delay $2\tau_1 - \tau_2$:

$$\left|E_T + E_{\tau_4}\right|^2 = 2\left|E_T E_{\tau_4}\right|\cos\left(\kappa\tau_4 t + \omega_s\tau_4 - \frac{1}{2}\kappa\tau_4{}^2\right)$$

Calculation Summary

The calculation above gives the fields contributing to different delays. In the collinear case, the first delay τ_1 is due to the beating signal containing the transmission field and the first delay echo along with the beating signal containing the second and third delay echo. The mixing of the transmission field against the second delay echo contributes to the second delay τ_2. Three mixing signals contribute to the 3rd delay τ_3, the first beating signal contains the transmission field and the third delay echo, the second contains the first and second delay echoes, and the third contains the first and fourth delay echoes. The fourth delay is due to two mixing signals one containing the transmission field and the fourth delay echo and the other containing the first and third delay echoes.

For angled beams, the transmission field and different delay echoes are spatially separated. The mixing signals contributing to a particular delay will be different then the collinear case where the transmission and different delay echoes are spatially overlapped. The first delay τ_1 is due to the beating signal containing the transmission field and the first delay echo. The first delay τ_2 is due to the beating signal containing the transmission field with the second delay echo. Two beating signals contribute the third delay, one containing the transmission field and the third delay echo and the other containing the first and second delay echoes. Finally, the fourth delay is generated from the beating of the transmission field and the fourth delay echo.

Simulation Settings

The scope of this simulation is to investigate the interference between different delays. To understand the cross talk effect, the simulations run involved keeping one of the delay peaks constant and varying the other. The medium was programmed using three brief Gaussian pulses, and the read out was achieved using a chirped field. In these simulations, how the peak magnitude is affected by varying one of the delays is investigated. The three brief pulses used for writing will produce a two delay scenario which creates four spectral gratings, each grating represented by the delays τ_1, τ_2, τ_3, τ_4. The delay τ_1 was kept constant and the delay τ_2 was varied. In one case, the varied delay (long delay) will be greater then τ_1 (short delay), and in the other case the varied delay (short delay) will be less then τ_1 (long delay). Note that thin material and single shot were used in this simulation. Table 6 summarizes the simulation settings.

Table 6 Simulation parameter summary for a multiple delay simulation

	Parameters		Symbol	Value
Computation (writing)	Temporal	Computation time	T	2.2 μs
		Number of points	N_t	44000
	Spectral	Computation Bandwidth	B	100 MHz
		Number of points	N_s	20000
	Spatial	Number of layers	Z	1
Computation (readout)	Temporal	Computation time	T	50
		Number of points	N_t	100000
	Spectral	Computational bandwidth	B	100
		Number of points	N_s	20000
Input pulses	Programming pulses	Area	*	0.1
		Shape	*	G
		Type	*	N
		Width	*	0.001 μs
	Readout pulse	Rabi Frequency	Ω_c	0.0001
		Shape	*	S/C
		Type	*	C
		Chirp Bandwidth	*	160 MHz
		Chirp Width	*	40 μs

Simulation Results

Figure 26 depicts how the long and short delays behave as the delay τ_2 is varied for the collinear case. The delay peak was normalized to the longest delay. The long delay remains constant while the short delay starts to decrease in magnitude as the two delays get close to each other. The overlap region is shown in the figure and it illustrates the region where the cross talk between the two delays is significant.

Figure 27 and Figure 28 respectively illustrate how the delay τ_3 peak amplitude and delay τ_4 peak amplitude change in terms of the varied delay. Both peaks in this case experience fluctuations.

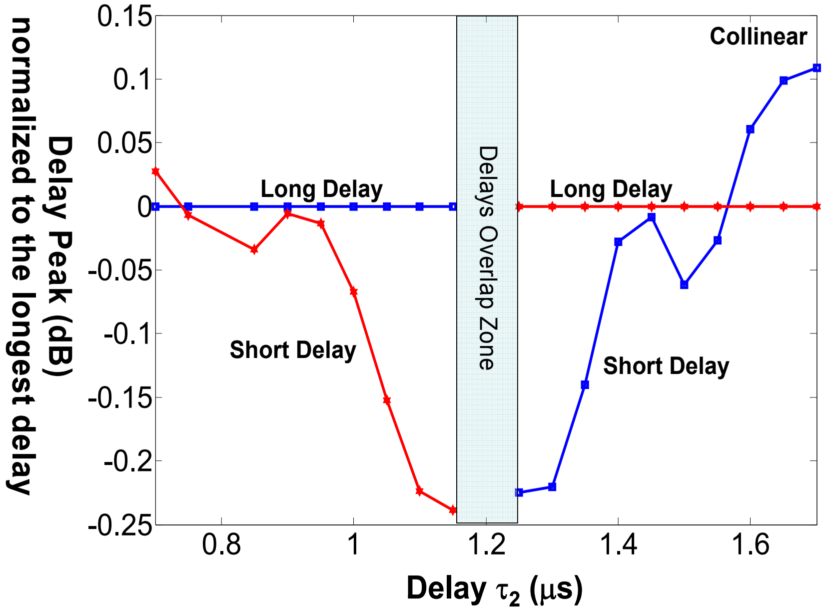

Figure 26 Delay peak (dB) normalized to the longest delay vs. the varying delay τ_2. The short delay remain constant, the long delay decrease in amplitude as the two delays as closer to each other.

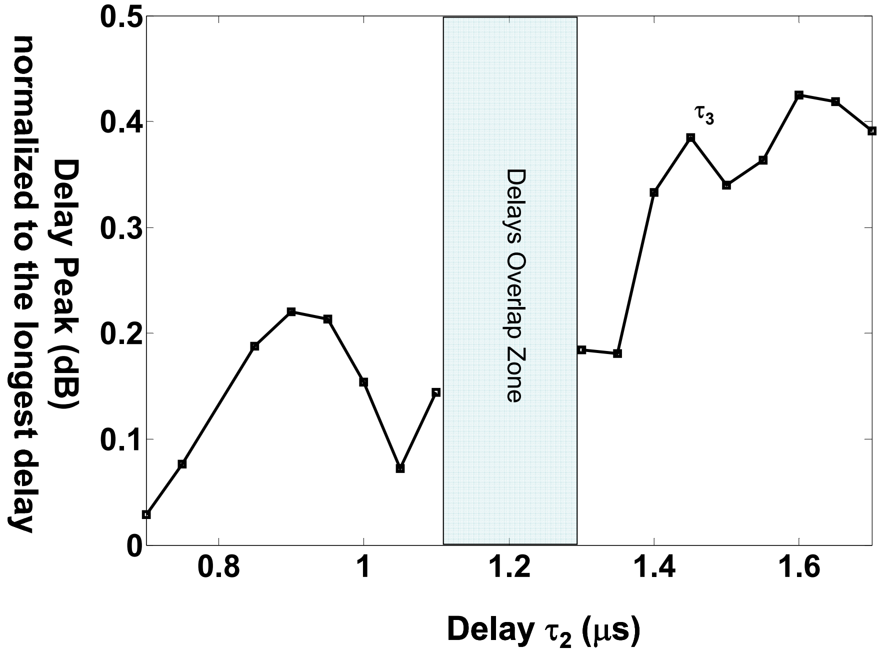

Figure 27 Delay peak (dB) normalized to the longest delay vs. the varying delay τ_2. Behavior of the delay τ_3 as the delay τ_2 varies.

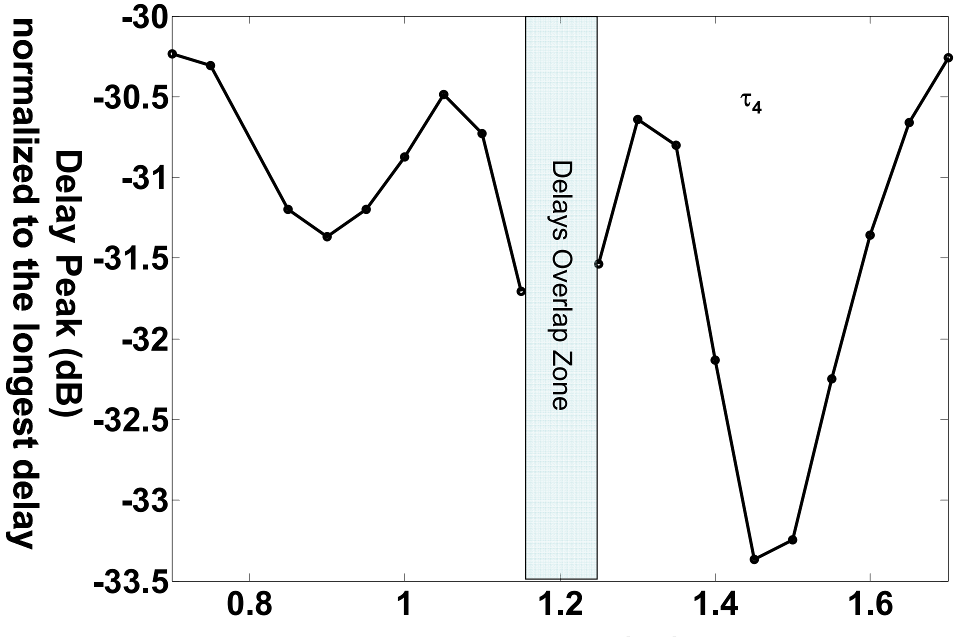

Figure 28 Delay peak (dB) normalized to the longest delay vs. the varying delay τ_2. Behavior of the delay τ_4 as the delay τ_2 varies.

From the results presented above we note that the delay peaks do indeed change as the position of delay τ_2 changes. The results prove that cross talk between the delay peaks occurs in the collinear geometry.

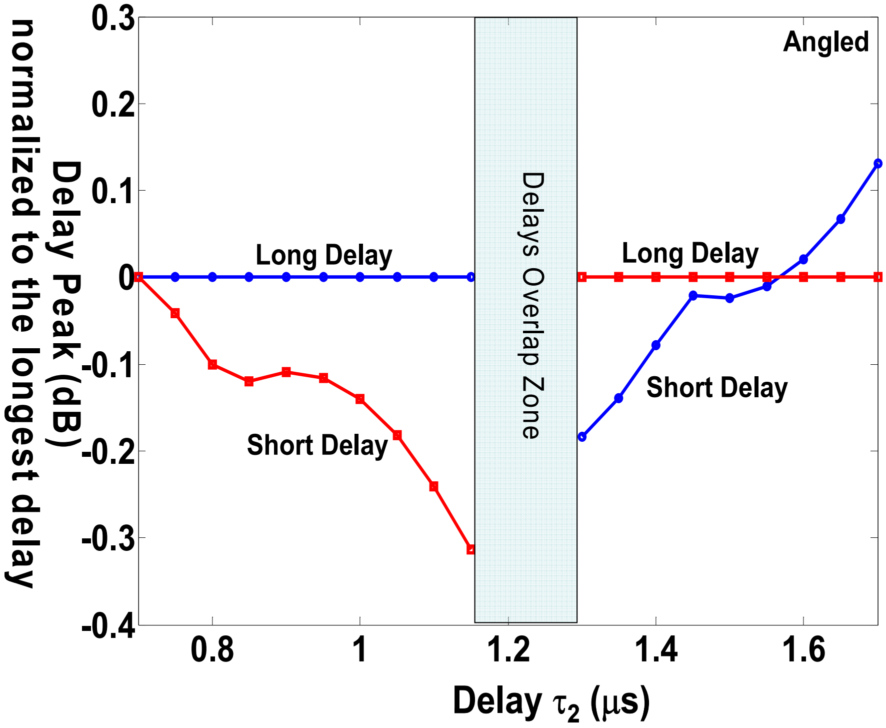

Figure 29 Delay peak (dB) normalized to the longest delay vs. the varying delay τ_2. The short delay remain constant, the long delay decrease in amplitude as the two delays as closer to each other.

For the angled beam geometry, Figure 29 illustrates the delay peak normalized to the longest delay in terms of the varying delay τ_2. The results show that cross talk is noticeable in the angled beam geometry as well.

Conclusion

In this chapter, an introduction to multiple delays programming and probing in the S2 material has been presented. When using three pulses to program the medium, four gratings with periods depending on the position of the pulses are imprinted in the S2 material. When probing the medium, intermodulations start to appear due to the beating of the transmitted field and the output echo fields along with the beating of the echo field against each other. The calculation presented in this chapter showed how the transmitted field and echo fields contribute to different delays. Finally, the simulation results proved that cross talk between different delays occurs in the S2 material for both the angled beam and the collinear geometries.

CHAPTER SIX

INTEGRATION IN S2 MATERIAL PROGRAMMING

Integration is used in radar systems to increase the system signal to noise ratio (SNR). A number of received pulses are added and the detection decision is based upon the resultant integrated signals, this process is called signal integration. [7].

In an S2 material, integration is achieved by exposing the material to a number of shots containing the reference and the return signals, this is achieved by either using the same or different coding waveforms. The use of integration increases the magnitude of both the useful signal and the noise floor, but the amount of signal added is higher then the amount of noise. In general, if a spread spectrum signal is used for a number of exposures J, then the signal will increase by J and the noise will increase as the $\sqrt{J}$ [5]. In this section, simulation results involving the use of integration or multiple exposures are presented.

In this chapter, we will try to understand how the harmonics behaves in terms of the number of shots used. Harmonics behavior is studied by programming the S2 material with a single delay. Simulations involving a multiple delay case have also been carried out to study how intermodulations behave in terms of the number of exposures used.

The simulations run in this chapter assume that the pulses used are brief and the medium is thin. The reason for these choices resides in the fact that we wanted to use the simplest setting possible to solely extract the effects of integration and not confusing them with other effects due to propagation or coded waveforms.

Single Delay Integration

Simulation Settings

In this simulation, two brief Gaussian pulses were used to program the medium and the probing was achieved using a chirped field. The simulation was run for 100 shots for three different values of the input pulses areas, 0.001π, 0.01π, and 0.02π. The simulation settings summary is shown in Table 7.

As shown in Table 7, the material is considered to be thin to separate the effects of propagation from integration. The programming pulses used are brief and Gaussian. In this simulation, the programming and probing were simulated separately using the "load to file" feature of the MB simulator offers, therefore, there is no need for non-uniform computational setting. The readout chirped pulse settings are shown in Table 7.

Table 7 Summery of the parameters setting for single delay multiple shots simulation

	Parameters		Symbol	Value
Material	Absorption coefficient		α	100 m^{-1}
	Thickness		L	0.001 m
	Absorption length		αL	0.1
Computation (writing)	Temporal	Computation time	T	1.2 μs
		Number of points	N_t	30000
	Spectral	Computation Bandwidth	B	100 MHz
		Number of points	N_s	10000
	Spatial	Number of layers	Z	1
Computation (readout)	Temporal	Computation time	T	50
		Number of points	N_t	100000
	Spectral	Computational bandwidth	B	100
		Number of points	N_s	10000
Input pulses	Programming pulses	Area	*	0.001
		Shape	*	G
		Type	*	N
		Width	*	0.001 μs
	Readout pulse	Rabi Frequency	Ω_c	0.0001
		Shape	*	S/C
		Type	*	C
		Chirp Bandwidth	*	160 MHz
		Chirp Width	*	40 μs

Simulation Results

Figure 30 depicts the signal strength in terms of the extracted time delay after the 1st shot and the 100th shot for the case where the input pulse area was set to 0.01π. The figure depicts that harmonics are present in the 100th shot compared to the 1st shot. The principal peak (P) and the 1st, 2nd, and 3rd order harmonics (H_1, H_2, and H_3) are shown in Figure 30. By analyzing the progression of shots, the harmonics increase gradually as the number of shots increases. The N_{fft} points used to calculate the power spectral density of the output intensity was 2^16, in addition, the FFT calculation started at 6.25 μs.

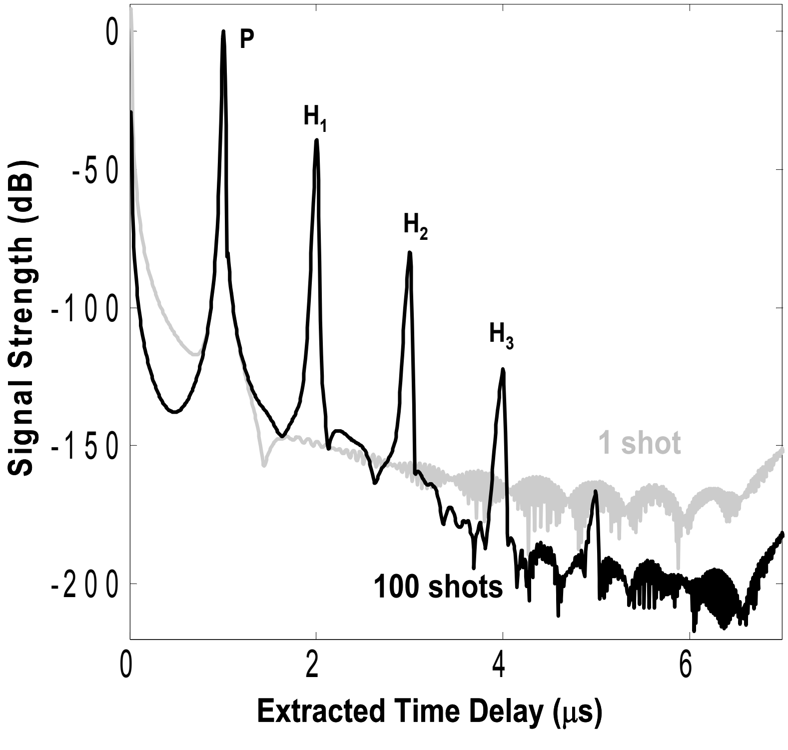

Figure 30 Signal strength in terms of the extracted time delay for the 1st and 100th shot (input pulse area 0.01π). Harmonics are observed in the 100th shots

The results that follow show the behavior of each harmonic as the number of shots increases for three different input pulse areas. Figure 31 depicts the signal strength for the principal peak and the harmonics normalized to the maximum value of the principal peak. in terms of the number of shots for an input pulse area of 0.02π.

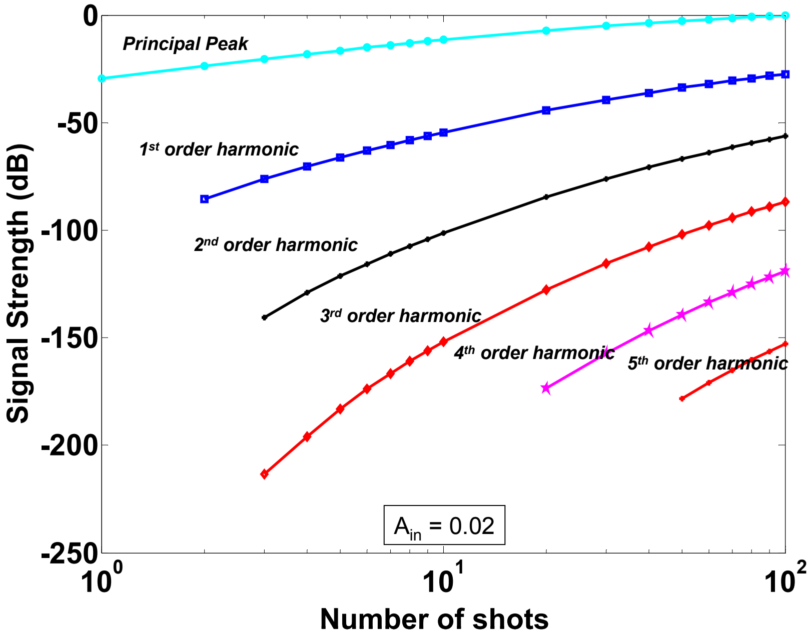

Figure 31 Signal strength for the principal peak and harmonics in terms of the number of shots for 0.02π input pulse area.

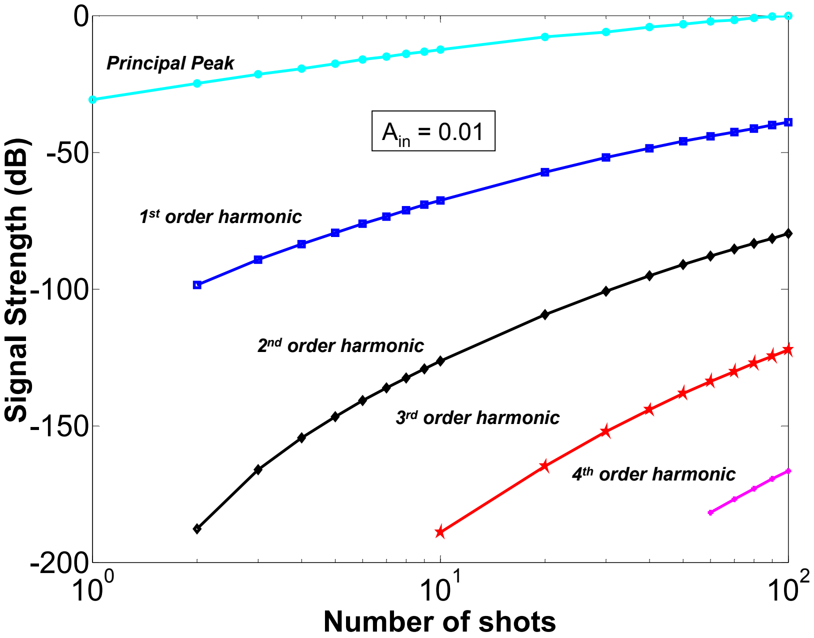

Figure 32 Signal strength for the principal peak and harmonics in terms of the number of shots for 0.01π input pulse area

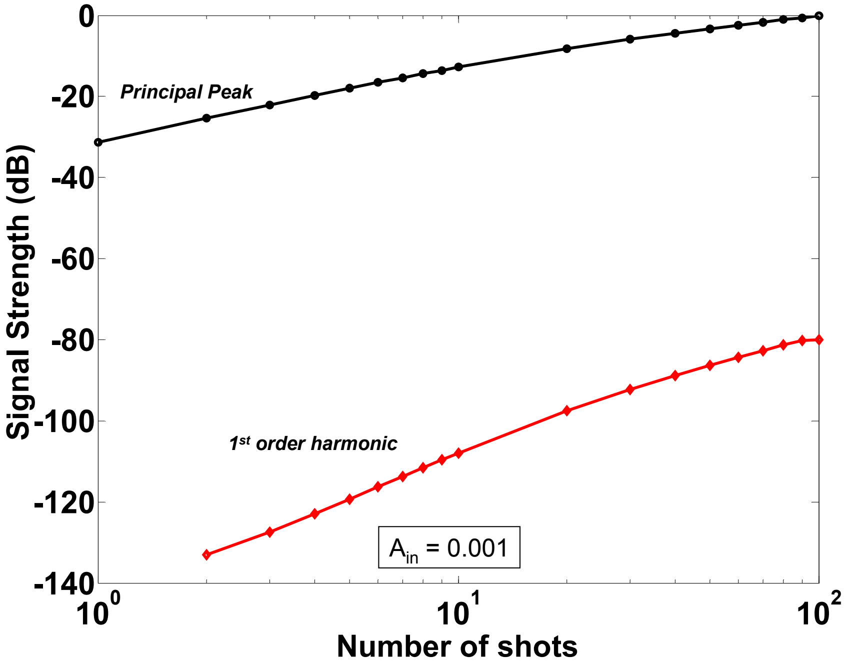

Figure 33 Signal strength for the principal peak and harmonics in terms of the number of shots for 0.001π input pulse area. Figure depicts how the principal peak and the harmonic increase in terms of the number of shots

In the simulation presented in this section where a single delay was simulated, we have shown that the harmonics start to manifest as the number of shots increases. As Figure 31, Figure 32, and Figure 33 show, the input pulse area also affects the harmonics. The higher order harmonics start manifesting earlier when the input pulse area is higher.

Multiple Delay Integration

Simulation Settings

In this section the simulations intend to explore how the output signal behaves as multiple shots combined with multiple delays are incident on the medium. Three brief Gaussian pulses have been used to program the S2 material, when read out; these pulses generate a multitude of delays with different orders. The first pulse area was 0.01π while the second and third pulses areas were 0.005π as depicted in Table 8. A chirped field with a chirp rate of 4 MHz/μs was used for readout. Five hundred shots, increasing by steps of 10, until shot 100, and then by 50 steps until shot 500 were simulated.

Table 8 Summery of the parameters setting for multiple delays multiple shots simulation

	Parameters		Symbol	Value
Material	Absorption coefficient		α	100 m^{-1}
	Thickness		L	0.001 m
	Absorption length		αL	0.1
Computation (writing)	Temporal	Computation time	T	2 μs
		Number of points	N_t	50000
	Spectral	Computation Bandwidth	B	100 MHz
		Number of points	N_s	10000
	Spatial	Number of layers	Z	1
Computation (readout)	Temporal	Computation time	T	50
		Number of points	N_t	100000
	Spectral	Computational bandwidth	B	100
		Number of points	N_s	10000
Input pulses	Programming pulses	Area	*	θ_1=0.001 θ_2=0.005 θ_3=0.005
		Shape	*	G
		Type	*	N
		Width	*	0.001 μs
	Readout pulse	Rabi Frequency	Ω_c	0.0001
		Shape	*	S/C
		Type	*	C
		Chirp Bandwidth	*	160 MHz
		Chirp Width	*	40 μs

Simulation Results

Figure 34 illustrates the power spectral density of the output signal intensity after 10 shots. The N_{fft} points used to calculate the power spectral density of the output intensity was 2^16, in addition, the FFT calculation started at 6.25 μs.

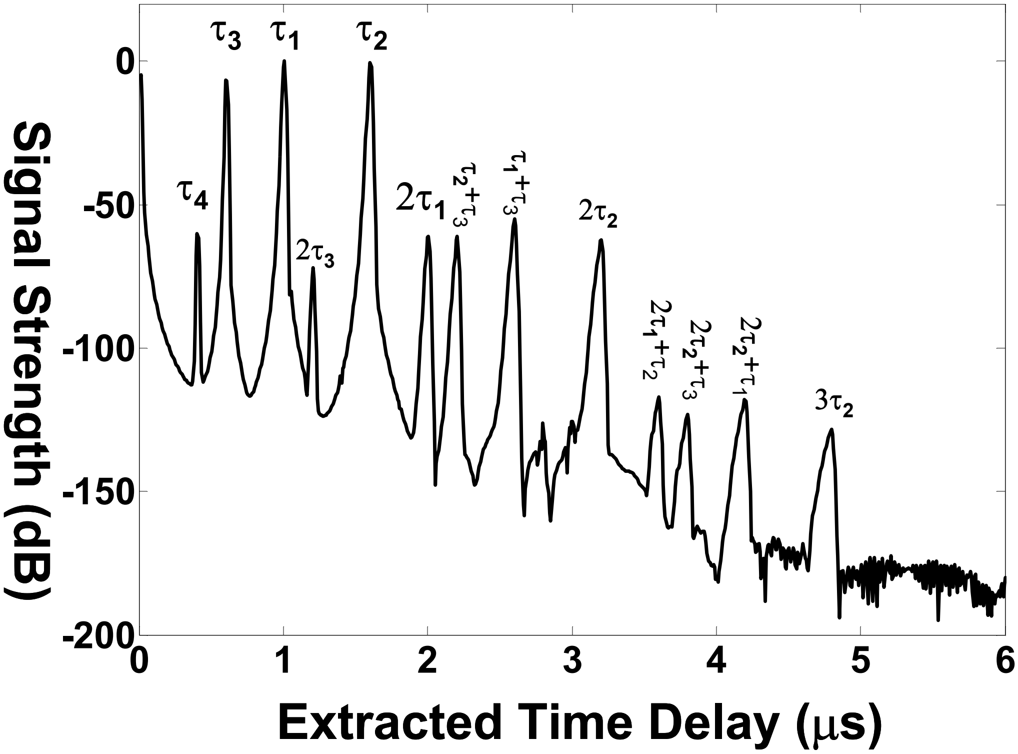

Figure 34 Signal peak strength vs. the extracted time delay, figure showing the peaks at different delays after 10 shots, higher order harmonics start to manifest after the number of shots increases.

As mentioned earlier in chapter 4 each peak, which is produced by beating either the transmission field with the output echo fields or the beating of the echo fields against each other, can be grouped by its order. Each delay peak has been processed to evaluate how it behaves while the number of shots increases. Figure 35 illustrates how different delay peaks behave as the number of shots increases. The order of the peaks has been selected depending on their slope in terms of the number of shots. Table 9 shows the calculated slope for each delay peak. The slope calculation considered the first 100 shots since a saturation behavior starts to occur after that.

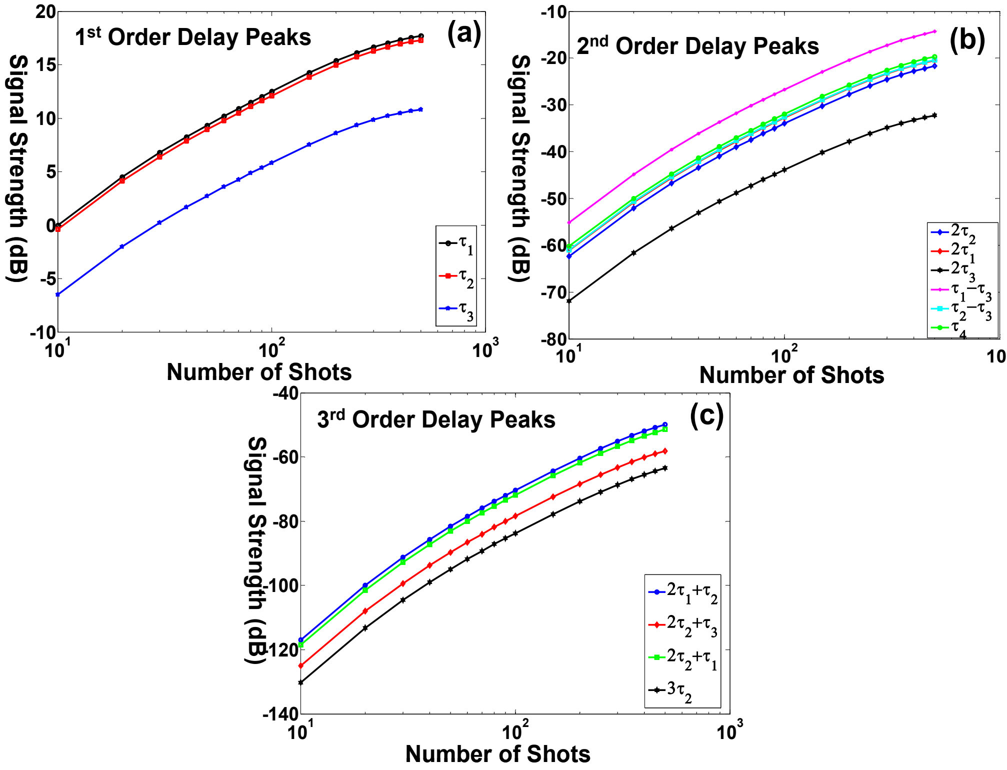

Figure 35 Delay peak vs. number of shots. (a) 1st order delay peaks (b) 2nd order delay peaks (c) 3rd order delay peak. All the values are relative to the first delay peak at shot1.

Table 9 Calculated slope (dB/decade) for each group of the delay peaks, the slopes were calculated to the 100th shot since saturation occurs after that

1st order	2nd order	3rd order
$\tau_1 = 12.5$	$2\tau_1 = 28.4$	$2\tau_1 + \tau_2 = 46.7$
$\tau_2 = 12.5$	$2\tau_2 = 28.4$	$2\tau_2 + \tau_3 = 46.6$
$\tau_3 = 12.35$	$2\tau_3 = 28.0$	$2\tau_2 + \tau_1 = 46.6$
	$\tau_1 + \tau_3 = 28.45$	$3\tau_2 = 46.5$
	$\tau_2 + \tau_3 = 28.4$	
	$\tau_4 = 28.2$	

From Table 9, it is evident that the delays τ_1, τ_2, and $\tau_3 = \tau_2 - \tau_1$ are of first order with a slope of 12.5 dB/decade. The delays $2\tau_1$, $2\tau_2$, $2\tau_3$, $\tau_4 = 2\tau_1 - \tau_2$, $\tau_1 + \tau_3$ and $\tau_2 + \tau_3$ are of second order with a slope of 28.4 dB/decade. Finally, the delays $2\tau_1 + \tau_2$, $2\tau_2 + \tau_3$, $2\tau_2 + \tau_1$, and $3\tau_3$ are of 3rd order with a slope of 46.6 dB/decade.

Once the order of the intermodulation is defined, the conclusion is depicted in Figure 36. The 2nd order intermodulations grow faster then the 1st order ones and for a particular noise floor, there exists an optimum SFDR that corresponds to a certain numbers of shots.

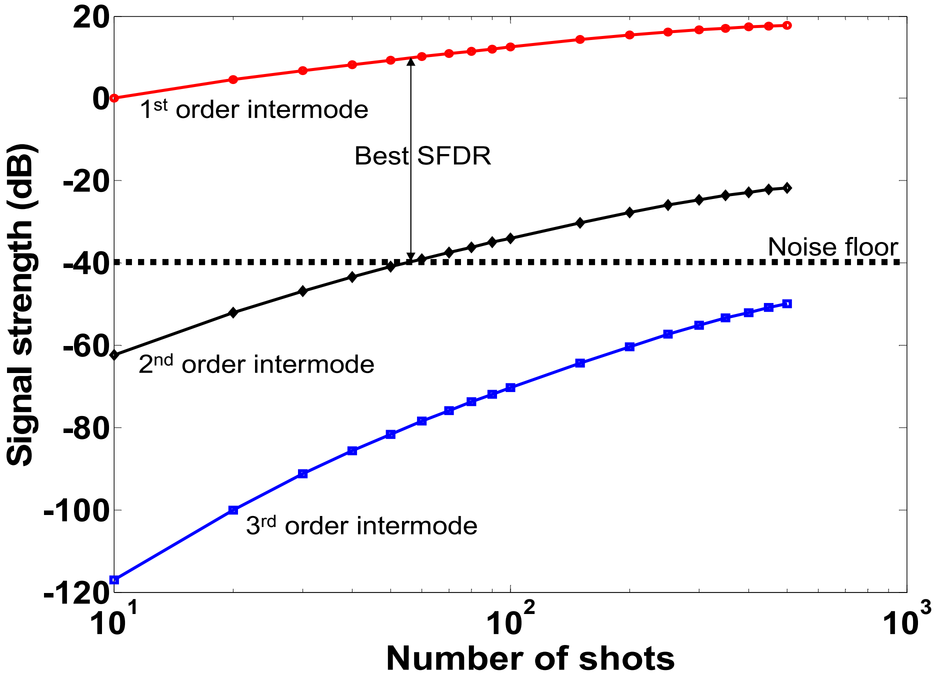

Figure 36 Different intermodulation orders and best SFDR for a particular noise floor

Results Summary and Discussion

The study of integration of multiple shots showed that when a single delay is programmed in the S2 material, harmonics are dependent on the number of shots used as well as on the strength of the input pulses area used to program the medium. In the case where multiple delays were considered, several intermodulations have been observed at the output, a slope has been calculated for all the different intermodulations which defined their order. We showed that as the order of the intermodulations gets higher their slope grows faster as the number of shots increases. A key conclusion of this chapter is that if a particular noise floor is enforced on the system, then the optimum number of shots that provides the best SFDR can be calculated.

In this chapter brief Gaussian pulses have been used to program the S2 material and the medium was considered thin, these assumptions are not valid in real world application, since long coded waveforms (increase processing gain) along with thick medium (increase absorption efficiency) are typically used.

CHAPTER SEVEN

COHERENCE EFFECT

Coherence time (T_2) as introduced earlier in chapter 2, depends on the homogenous linewidth of the S2 material, $T_2 = \frac{1}{\pi \Delta f_h}$. The coherence time represents the time window where the medium remembers its phase, and rephasing can only occur within that particular time window. In this chapter the effect of coherence time on intermodulations in both the programming and probing process will be investigated. T_2 is varied and the behavior of each intermodulation is analyzed. Three cases will be considered:

- Case 1: T_2 varies in writing and is infinite in readout
- Case 2: T_2 is infinite in writing and varies in readout
- Case 3: T_2 varies in both writing and readout

The simulation results are explained by a calculation shown in the next section for validation.

Calculation

In this calculation we explore three cases. The first case considers the coherence as it affects the programming process only, the second case considers the coherence as it affects the readout process, and the third case considers the coherence as it affects both the programming and readout process.

Coherent Effect on the Grating Writing Processing

It is known that the grating strength decays exponentially with coherence time. If we denote γ as the grating strength, T_2 as the coherence time, and τ_i as the delay, then the grating strength is generally exponentially proportional to $-\tau_i / T_2$ or $\gamma_i \propto \exp(-\tau_i / T_2)$, the equation is valid for i = 1, 2, and 3. However, for the third order intermodulation $\tau_4 = 2\tau_1 - \tau_2$, the delay becomes proportional to $-\tau_2/T_2$ rather then $-\tau_4/T_2$.

Coherent Effect on the Grating Readout Processing

For the readout using heterodyne detection, we calculate the delay signals and spurs, where E_T is the transmission field, and $E_{\tau_1}, E_{\tau_2}, E_{\tau_3}, E_{\tau_4}$ are the first, second, third, and fourth delay echoes respectively.

For i = 1 and 2, the readout signal is related to the coherence effect as:

$$S_i \propto \left|E_T E_{\tau_1}\right|^2 \exp(-\tau_i / T_2)$$

For i = 3 the readout signal is:

$$S_3 \propto \left|E_T E_{\tau_3}\right|^2 e^{\frac{-2\tau_3}{T_2}} + \left|E_{\tau_1} E_{\tau_2}\right|^2 e^{\frac{-2(\tau_2+\tau_1)}{T_2}}$$

For i = 4 the readout signal is:

$$S_4 \propto \left|E_T E_{\tau_4}\right|^2 e^{\frac{-2\tau_4}{T_2}} + \left|E_{\tau_1} E_{\tau_3}\right|^2 e^{\frac{-2\tau_2}{T_2}}$$

Coherent Effect on Both the Writing and Readout Processing

Combining the effect on the writing and readout processing, we calculate the delay signals and spurs as

$$S_i \propto e^{\frac{-4\tau_i}{T_2}} \quad \text{for i = 1 and 2}$$

$$S_3 \propto \left|E_T E_{\tau_3}\right|^2 e^{\frac{-4\tau_3}{T_2}} + \left|E_{\tau_1} E_{\tau_2}\right|^2 e^{\frac{-4(\tau_2+\tau_1)}{T_2}}$$

$$S_4 \propto \left|E_T E_{\tau_4}\right|^2 e^{\frac{-2\tau_2}{T_2}} e^{\frac{-2\tau_4}{T_2}} + \left|E_{\tau_1} E_{\tau_3}\right|^2 e^{\frac{-4(\tau_1+\tau_3)}{T_2}}$$

Simulation Settings

The simulations undertaken involved short delays for both the cases where $2\tau_1>\tau_2$ and $2\tau_1<\tau_2$ as well as a long delay case to make sure that the coherence decay equally affects shot and long delays. Thin material was considered and no integration was used in these simulations.

In these cases, the computational time varies depending on the pulse temporal position (20 points per cycle was the chosen resolution for all the simulations in this chapter). The coherence time was set to 1μs, 10 μs, 100 μs and infinity in all cases. The writing pulse area was considered to be 0.1π. The readout was accomplished using a chirped pulse with a chirp rate of 4 MHz/μs and a Rabi frequency of 0.0001 to minimize nutation effects. Note that the reader can refer to Table 8 for the readout parameters settings since the same parameters were used in this simulation.

Simulation Results

Figure 37 shows the output field signal strength vesus the extracted time delay for the long delays case where T_2 was varied in both writing and readout. The delays τ_1, τ_2, τ_3, and τ_4 ($2\tau_1$-τ_2) are depicted in Figure 37. The dark line represents the case where T_2 is infinite in both writing and readout (ideal case), and the gray line represents the case where T_2 was set to 1μs in both writing and readout. The results show that indeed the coherence time affects the amplitude of different delay peaks. The following results provide a more quantitative view of that change.

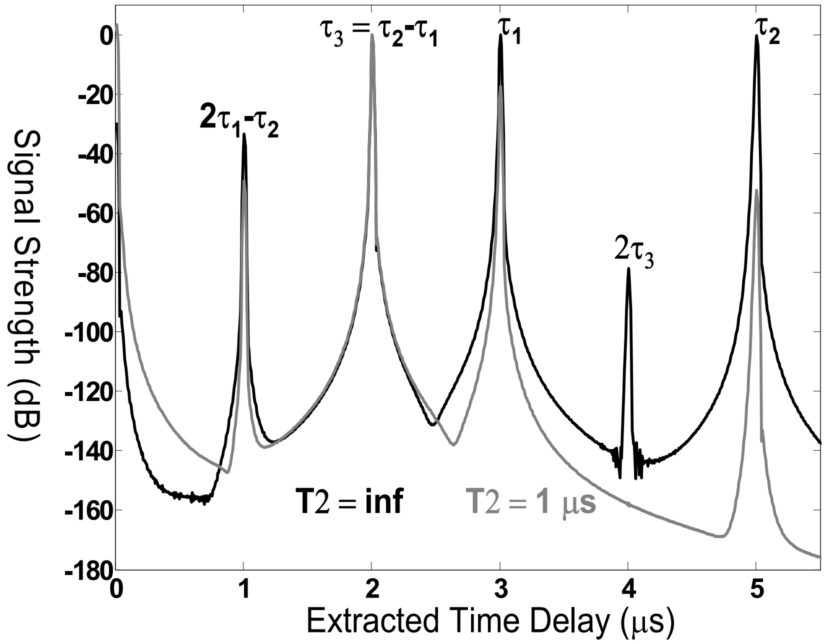

Figure 37 Signal strength vs. extracted time, the dark line for T_2 is infinite and gray line for T_2=1μs.

For the cases run where T_2 is infinite in readout and varies in writing (case1), T_2 is infinite in writing and varies in readout (case2), and T_2 varies in both writing and readout (case3), the data were processed and a decay factor was calculated to compare how the simulation results match the calculations. The decay factor calculation is given below.

If we denote, S_i as the output signal strength, τ_i as the delay peak, and a_i as the slope then:

$$S_i = \exp\left(-\frac{a_i \tau_i}{T_2}\right)$$

We should note that the calculation for the decay factor for S3 and S4 assumed a single exponential function, however, the calculation showed that in these cases there is a double exponential dependence.

To convert to dB

$$S_{i(dB)} = 20\log\left(S_i\right)$$

$$\Delta S_{i(dB)} = 20\log(e)\left[\frac{a_i \tau_i}{T_2}\right] \text{ where } \Delta S_{i(dB)} = S_{i(dB)}\Big|_{T_2=\infty} - S_{i(dB)}\Big|_{T_2=1}$$

Solving for the slope

$$a_i = \frac{T_2 \times \Delta S_{i(dB)}}{20\log(e)\tau_i}$$

Figure 38 depicts the magnitude change for the delays as a function of the inverse of coherence decay for the case where T_2 was varied in both writing and readout. Figure 39 depicts the delays signal change as a function of the inverse of the coherence decay where T_2 was infinite in writing while T_2 varied in the readout. Figure 40 shows the delay signal change as the inverse of the coherence decay in writing where T_2 is infinite in reading.

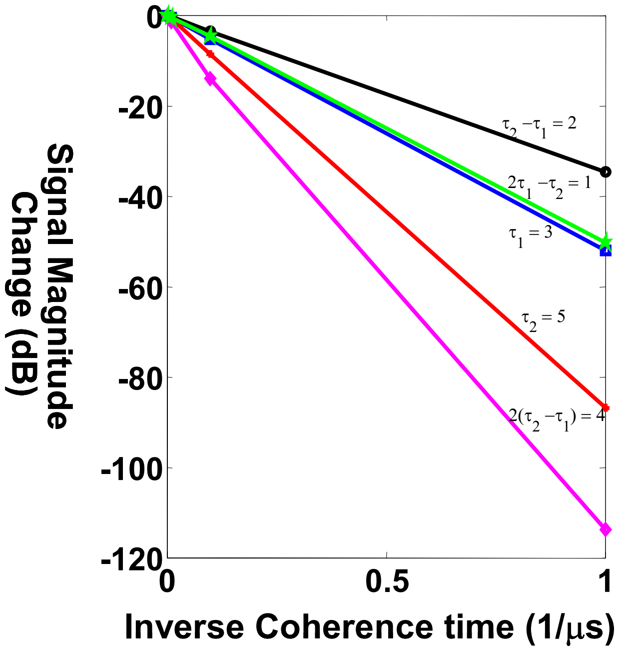

Figure 38 Delays magnitude change vs. the inverse of coherence decay, $2\tau_1 > \tau_2$, T_2 varied in both writing and readout.

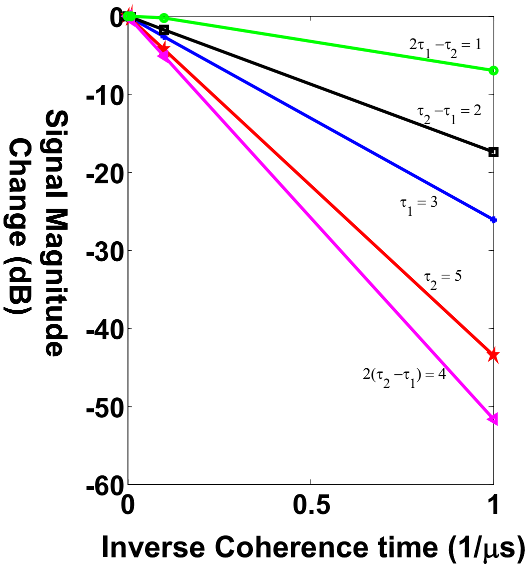

Figure 39 Delays magnitude change vs. the inverse of coherence decay, $2\tau_1 > \tau_{2,}$ T_2 is infinite in writing.

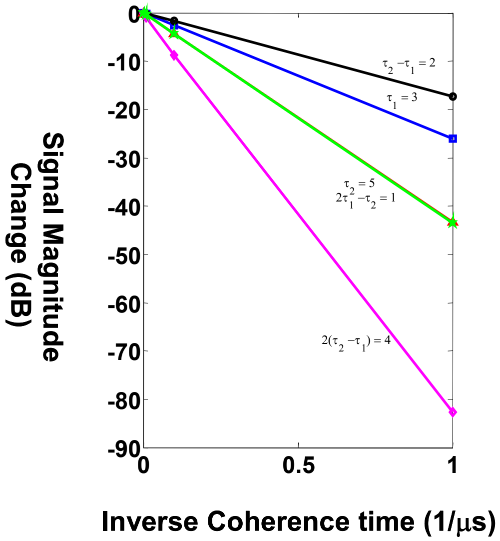

Figure 40 Delays magnitude change vs. the inverse of coherence decay, $2\tau_1 > \tau_{2,}$ T_2 is infinite in reading

Table 10 Signal peak strength and decay factor results for a long delay case ($2\tau_1>\tau_2$) (a) T_2 infinite in writing (b) T_2 infinite in readout (c) T_2 varies in both writing and readout

Delays (T_2 infinite in writing)	$\Delta S_{i(dB)}$	a_i
$\tau_1 = 3$ μs	-26.095	1.0014
$\tau_2 = 5$ μs	-43.534	1.0024
$\tau_3 = \tau_2-\tau_1 = 2$ μs	-17.401	1.0017
$\tau_4 = 2\tau_1-\tau_2 = 1$ μs	-6.9888	0.8046

(a)

Delays (T_2 infinite in reading)	$\Delta S_{i(dB)}$	a_i
$\tau_1 = 3$ μs	-26.104	1.0018
$\tau_2 = 5$ μs	-43.429	1.0000
$\tau_3 = \tau_2-\tau_1 = 2$ μs	-17.415	1.0025
$\tau_4 = 2\tau_1-\tau_2 = 1$ μs	-43.468	1.00089

(b)

Delays (T_2 varied in both writing and reading)	$\Delta S_{i(dB)}$	a_i
$\tau_1 = 3$ μs	-52.147	2.0012
$\tau_2 = 5$ μs	-86.927	2.0016
$\tau_3 = \tau_2-\tau_1 = 2$ μs	-34.771	2.0016
$\tau_4 = 2\tau_1-\tau_2 = 1$ μs	-50.417	5.8054

(c)

Table 10 summarizes the results of the signal peak strength for all the delays and provides the corresponding decay factor. As shown in the calculations, when T_2 is infinite in readout or in writing all the three delays (τ_1, τ_2, and τ_3) experience a unity decay factor. For the case where T_2 was varied in both writing and readout the decay factor experienced by the delays (τ_1, τ_2, and τ_3) is 2, and that is due to the accumulated T_2 effect of both writing and readout, as provided by the calculations. The delay τ_4 on the other hand shows a decay factor that is higher then the accumulated T_2 affect. We can relate the difference between the calculated and simulated factor in the case where i = 4 to the fact that dependence of the signal on both exponentials is significant. Though we assumed a single exponential for i = 3, the simulation results agreed with the simulation and that is due to the fact the only one of the exponential factor has a significant impact on the readout signal.

In the short delays case, two cases were considered, the case where $2\tau_1>\tau_2$ and the case where $2\tau_1<\tau_2$. Figure 41, Figure 42, and Figure 43 depict the case where $2\tau_1>\tau_2$. Figure 41 depicts the case where T_2 was varied in both writing and readout, Figure 42 depicts the case where T_2 was infinite in writing and Figure 43 depicts the case where T_2 is infinites in readout.

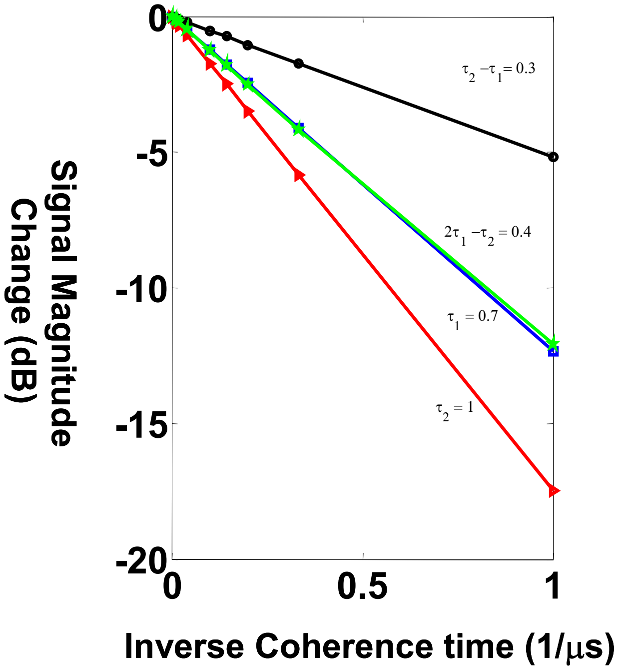

Figure 41 delays magnitude change vs. the inverse of coherence decay, $2\tau_1> \tau_2,$ T_2 varied in both writing and readout.

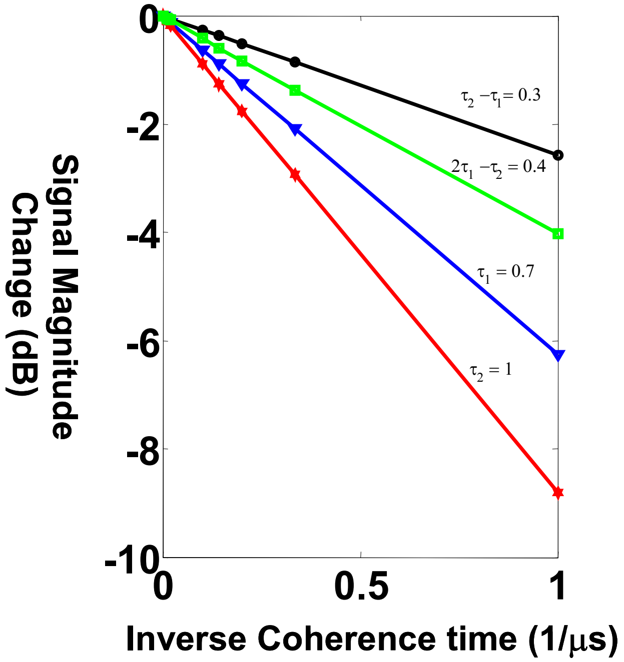

Figure 42 delays magnitude change vs. the inverse of coherence decay, $2\tau_1 > \tau_2$, T_2 is infinite in writing.

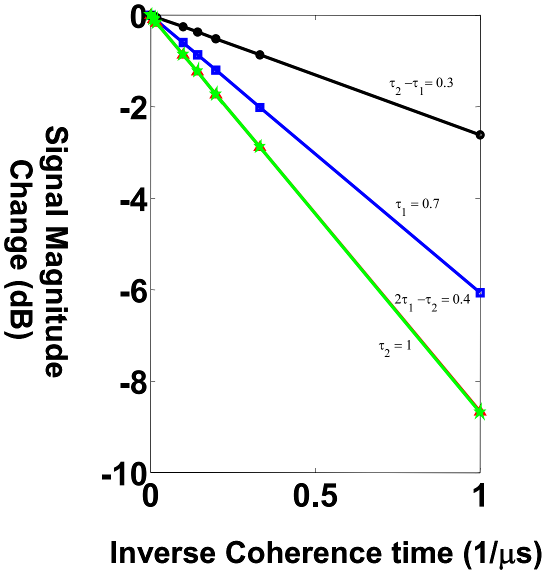

Figure 43 Delays magnitude change vs. the inverse of coherence decay, $2\tau_1 > \tau_2$, T_2 is infinite in readout.

Table 11 Signal peak strength and decay factor results for the short delay case ($2\tau_1>\tau_2$) (a) T_2 infinite in writing (b) T_2 infinite in readout (c) T_2 varies in both writing and readout

Delays (T2 infinite in writing)	$\Delta S_{i(dB)}$	a_i
$\tau_1 = 0.7\ \mu s$	-6.2584	1.0293
$\tau_2 = 1\ \mu s$	-8.8079	1.0140
$\tau_3 = \tau_2-\tau_1 = 0.3\ \mu s$	-2.5769	0.9889
$\tau_4 = 2\tau_1-\tau_2 = 0.4\ \mu s$	-4.0292	1.1597

(a)

Delays (T2 infinite in reading)	$\Delta S_{i(dB)}$	a_i
$\tau_1 = 0.7\ \mu s$	-6.0728	0.9988
$\tau_2 = 1\ \mu s$	-8.6739	0.9986
$\tau_3 = \tau_2-\tau_1 = 0.3\ \mu s$	-2.6257	1.0076
$\tau_4 = 2\tau_1-\tau_2 = 0.4\ \mu s$	-8.6847	0.9999

(b)

Delays (T2 varied in both writing and reading)	$\Delta S_{i(dB)}$	a_i
$\tau_1 = 0.7\ \mu s$	-12.325	2.0271
$\tau_2 = 1\ \mu s$	-17.479	2.0123
$\tau_3 = \tau_2-\tau_1 = 0.3\ \mu s$	-5.1899	1.9917
$\tau_4 = 2\tau_1-\tau_2 = 0.4\ \mu s$	-12.093	3.4806

(c)

Table 11 summarizes the results of the signal peak strength for all the delays and the decay factors corresponding to them for the short delay case where $2\tau_1>\tau_2$. As expected from the calculations, the first order delays experience a unity decay factor when T_2 was infinite in writing or in readout, when T_2 was applied to both writing and readout the accumulated effect results in a decay factor of 2. Delay τ_4, on the other hand, does not seem to follow the response predicted.

The case where $2\tau_1<\tau_2$ is depicted in Figure 44 (T_2 varies in both writing and readout), Figure 45 (T_2 infinite in writing), and Figure 46 (T_2 infinite in readout). Table 12 summarizes the results of the delay peaks and the decay factors corresponding to the delay.

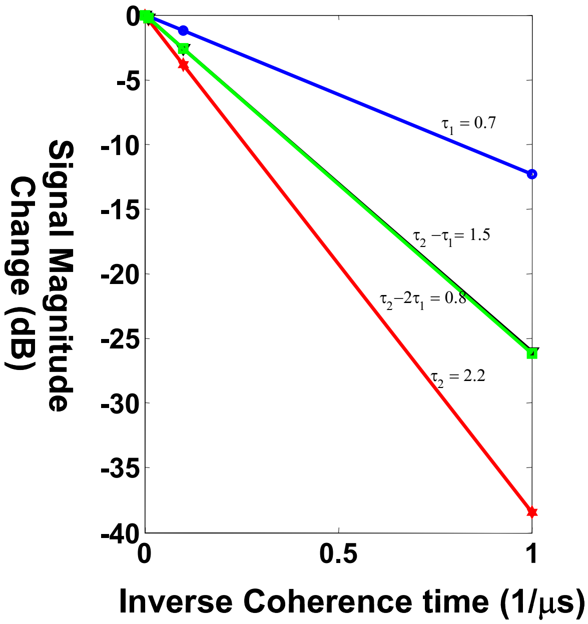

Figure 44 Delays magnitude change vs. the inverse of coherence decay, $2\tau_1<\tau_2$, T_2 varied in both writing and readout.

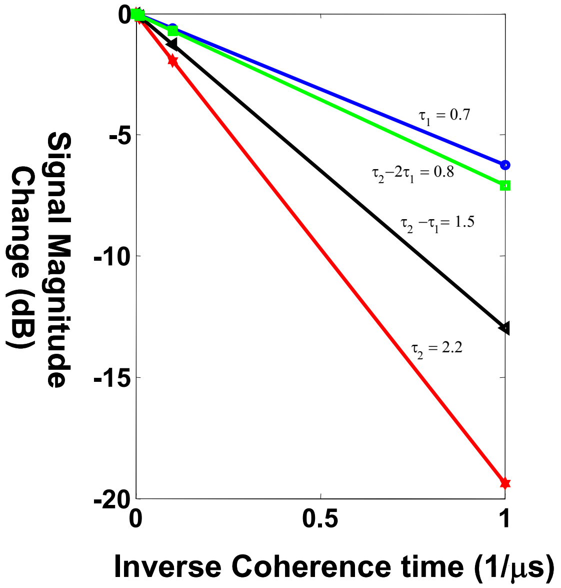

Figure 45 Delays magnitude change vs. the inverse of coherence decay, $2\tau_1<\tau_2$, T_2 is infinite in writing.

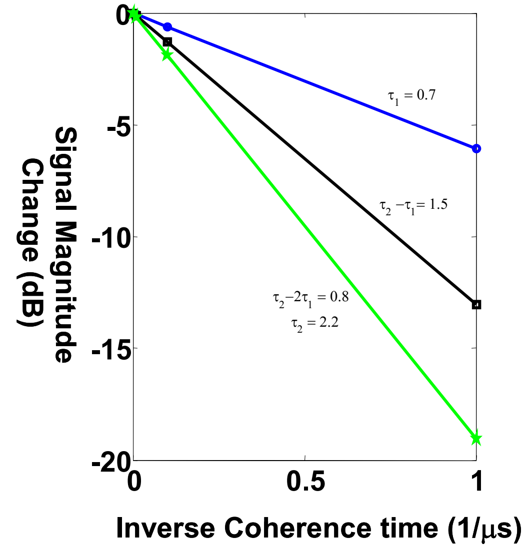

Figure 46 Delays magnitude change vs. the inverse of coherence decay, $2\tau_1<\tau_2$, T_2 is infinite in readout.

Table 12 Signal peak strength and decay factor results for the short delay case ($2\tau_1<\tau_2$) (a) T_2 infinite in writing (b) T_2 infinite in readout (c) T_2 varies in both writing and readout

Delays (T2 infinite in writing)	$\Delta S_{i(dB)}$	a_i
$\tau_1 = 0.7$ μs	-6.2631	1.0301
$\tau_2 = 1$ μs	-19.381	1.0142
$\tau_3 = \tau_2-\tau_1 = 0.3$ μs	-12.964	0.9950
$\tau_4 = 2\tau_1-\tau_2 = 0.4$ μs	-7.0974	1.0214

(a)

Delays (T2 infinite in reading)	$\Delta S_{i(dB)}$	a_i
$\tau_1 = 0.7$ μs	-6.0777	0.9996
$\tau_2 = 1$ μs	-19.085	0.9987
$\tau_3 = \tau_2-\tau_1 = 0.3$ μs	-13.05	1.0016
$\tau_4 = 2\tau_1-\tau_2 = 0.4$ μs	-19.076	0.9983

(b)

Delays (T2 varied in both writing and reading)	$\Delta S_{i(dB)}$	a_i
$\tau_1 = 0.7$ μs	-12.326	2.0273
$\tau_2 = 1$ μs	-38.457	2.0125
$\tau_3 = \tau_2-\tau_1 = 0.3$ μs	-25.998	1.9954
$\tau_4 = 2\tau_1-\tau_2 = 0.4$ μs	-26.178	3.7673

(c)

The same conclusions are drawn for the decay factor calculations shown in Table 12. All the delay peaks agreed with calculation results except for the delay τ_4 which did not agree with predictions.

To ensure that the length of the delays does not influence the effect of the coherence decay on the delays decay factor, a series of simulations involving longer delays was carried out. Figure 47 depicts the delays magnitude change as function of the inverse of coherence decay, T_2 varied in both writing and readout. Figure 48 depicts the delays signals change as function of the inverse of coherence decay, T_2 is infinite in writing while T_2 varies in the readout. Figure 49 shows the delays signal change as the inverse of coherence decay in writing, T_2 is infinite in reading.

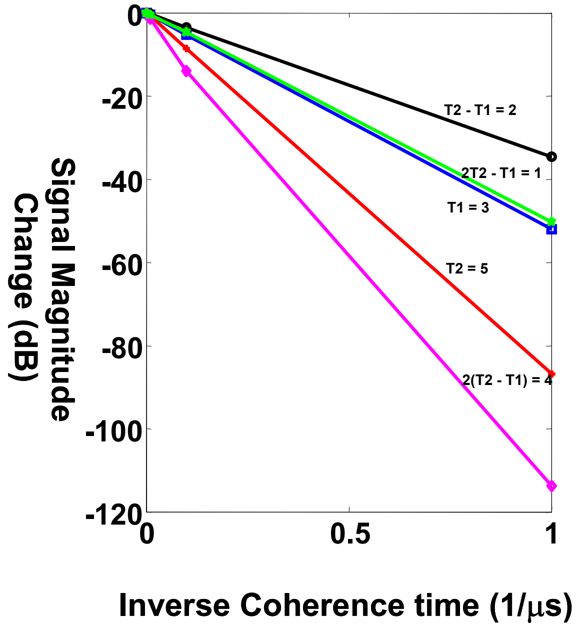

Figure 47 Delays magnitude change vs. the inverse of coherence decay, $2\tau_1 > \tau_{2,}$ T_2 varied in both writing and readout.

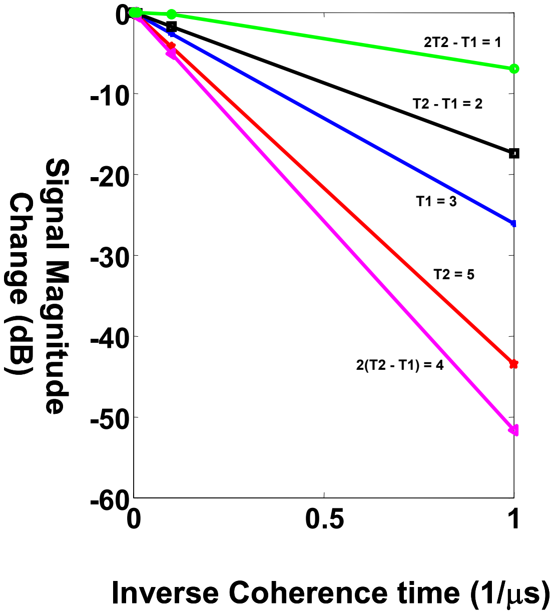

Figure 48 Delays magnitude change vs. the inverse of coherence decay, $2\tau_1 > \tau_{2,}$ T_2 is infinite in writing.

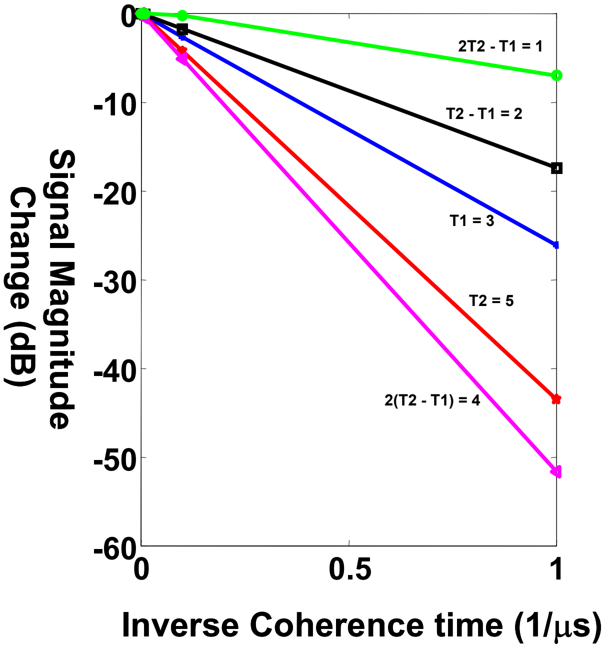

Figure 49 Delays magnitude change vs. the inverse of coherence decay, $2\tau_1 > \tau_2$, T_2 is infinite in reading

Table 13 Signal peak strength and decay factor results for a long delay case ($2\tau_1 > \tau_2$) (a) T_2 infinite in writing (b) T_2 infinite in readout (c) T_2 varies in both writing and readout

Delays (T_2 infinite in writing)	$S_{i(dB)}$	a_i
$\tau_1 = 3$ μs	-26.095	1.0014
$\tau_2 = 5$ μs	-43.534	1.0024
$\tau_3 = \tau_2 - \tau_1 = 2$ μs	-17.401	1.0017
$\tau_4 = 2\tau_1 - \tau_2 = 1$ μs	-6.9888	0.8046

(a)

Delays (T_2 infinite in reading)	$S_{i(dB)}$	a_i
$\tau_1 = 3$ μs	-26.104	1.0018
$\tau_2 = 5$ μs	-43.429	1.0000
$\tau_3 = \tau_2 - \tau_1 = 2$ μs	-17.415	1.0025
$\tau_4 = 2\tau_1 - \tau_2 = 1$ μs	-43.468	1.00089

(b)

Delays (T_2 varied in both writing and reading)	$S_{i(dB)}$	a_i
$\tau_1 = 3$ μs	-52.147	2.0012
$\tau_2 = 5$ μs	-86.927	2.0016
$\tau_3 = \tau_2 - \tau_1 = 2$ μs	-34.771	2.0016
$\tau_4 = 2\tau_1 - \tau_2 = 1$ μs	-50.417	5.8054

(c)

The decay factor of the magnitude of the delays obtained in the long delay case behaves in the same manner compared to the short delay case, while the delay τ_4 still does not agree with the calculation results.

Long and Overlapped Waveforms

In this section the coherence decay and its effect on long overlapped waveform was studied. The first part of the simulation investigates how the length of the coded waveform affects the output signal dynamic range, the second part of the simulation shows how the coherence decay of the material affects the signal dynamic range when long coded overlapped waveforms are used to program the material. The first series of simulations involved running 3 simulations varying the pulse length (10, 50, 100 μs), while the bit width was set to 0.005 μs. Figure 50 illustrates the simulation setup.

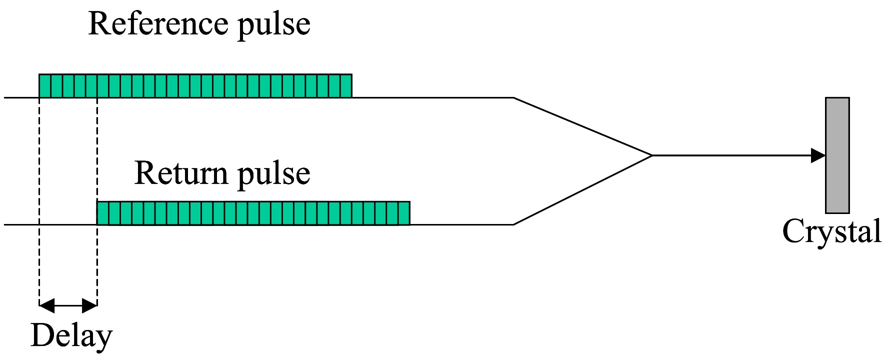

Figure 50 Simulation setup schematic for a long pattern pulse

Figure 51 shows how the peak (at 1μs) to sidelobe ratio behaves by varying pattern length for the case of T_2 = inf and T_2 = 100μs. The first observation made from Figure 51 shows that the dynamic range of the output signal increases as the length of the waveform increases. The second conclusion derived from Figure 51 is that the coherence delay tends to affect the dynamic range of the material even when long waveforms are used. As the coherence decay decreases the dynamic range decreases as well, as shown in Figure 51.

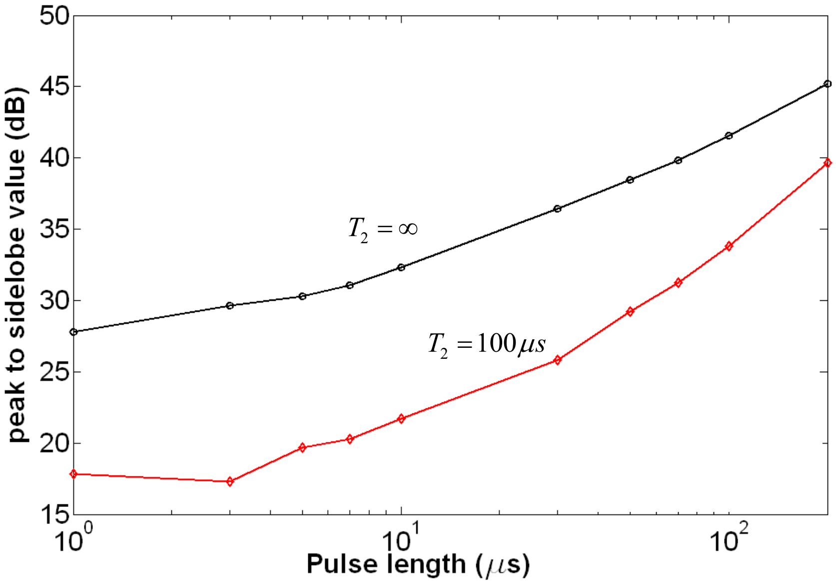

Figure 51 Peak to sidelobe ratio for varying waveform length

Results Summary and Discussion

The simulation results presented above indicate that in both the programming and readout process where the coherence decay was a factor in one or the other, the coherence time affects each of the intermodulations as predicted by the calculations.

The calculated decay factor for all the intermodulations was determined to be 1. The results agreed with the calculations for the delays τ_1, τ_2 and τ_3. The results for the delay τ_4 did not agree with the calculation prediction.

The simulations showed that the length of the delays does not affect how the coherence time influences the intermodulation decay factor. Also, in both the cases where $2\tau_1>\tau_2$ and $2\tau_1<\tau_2$ the same decay factor was calculated. In addiction and as shown in Figure 51, the dynamic range decreases as the coherence time decreases.

Overall, Looking at all the three cases, we note that T2 affects the signal peaks independently on the delay length or the delay position ($2\tau_1>\tau_2$ or $2\tau_1<\tau_2$). The simulation and calculation results agreed when for the case where i = 1, 2, and 3. However, in the case where i = 4 the calculation did not much the simulation results. The reason for the mismatch was related to the fact that in calculating the decay factor we assumed the readout signal was dependent only on one exponential function. The simulations showed that indeed both exponential functions affect the readout signal for the case where i = 4. Moreover, while the use of longer coded waveforms improves the signal dynamic range, the coherence decay still degrades it.

CHAPTER EIGHT

LASER COHERENCE TIME EFFECT

The programming and readout in the S2CHIP module is achieved by using a frequency stable laser. A laser is usually characterized by its linewidth $\Delta\gamma$ which defines its coherence time τ_{coh}. The laser linewidth and the coherence time of a laser are related as: $\Delta\gamma = \frac{1}{\pi\tau_{coh}}$. In this chapter, the effects of the laser coherence time on the signal dynamic range are examined. In addition to the laser coherence time, dynamic range at different delays is investigated. The first section of this chapter introduces the simulation settings, the second section deals with effects of the laser coherence time and the third section tackles the variation in the grating delay and it effects on the signal dynamic range.

Simulation Settings

In this set of simulations, a writing scheme was not necessary since the option of programming a perfect grating in the material through the OCT simulator was used. The grating was programmed using a grating strength of 0.1, and in the case where the laser coherence time was varied the grating period was fixed to 1 MHz. The inhomogeneous linewidth of the material was set to 10 GHz. A chirped field was used for readout. The simulation parameters are summarized in Table 14. The coherence time of the laser was varied from 1 μs to 1s as shown in Table 15. The grating period was varied from 1 μs to 7 μs in steps of 1 μs for two values of the laser coherence time, 10 μs and 100μs.

Table 14 Summery of the parameters setting for readout in the laser coherence time simulations

Computation	Temporal	Computation time	T	50
		Number of points	N_t	100000
	Spectral	Computational bandwidth	B	100
		Number of points	N_s	10000
Readout pulse	Rabi Frequency		Ω_c	0.0001
	Shape		*	S/C
	Type		*	C
	Chirp Bandwidth		*	160 MHz
	Chirp width		*	40 μs

Table 15 Coherence time values used in the simulation, each value was simulated 20 times to minimize errors associated with the random natures of the laser noise

Coherent Time (μs)
1
5
7
10
15
20
50
70
100
200
500
1000

Laser Coherence Time Effects

The PSD function was run on the output intensity of the transmitted signal for different value of the laser coherence time to obtain the results shown in Figure 52. Figure 52 shows the signal strength in terms of the extracted time delay for four different laser coherence times. The results show that as the laser coherence decreases as the noise level increases. The computational noise is shown to compare the ideal case when the coherence time of the laser is infinite (ideal case) and the case when the coherence time of the laser is varied. Three noises regions over which the noise was averaged are defined in Figure 52 (S1 [0.1 μs to 0.5 μs], S2 [2 μs to 3 μs], and S3 [5 μs to 10 μs]).

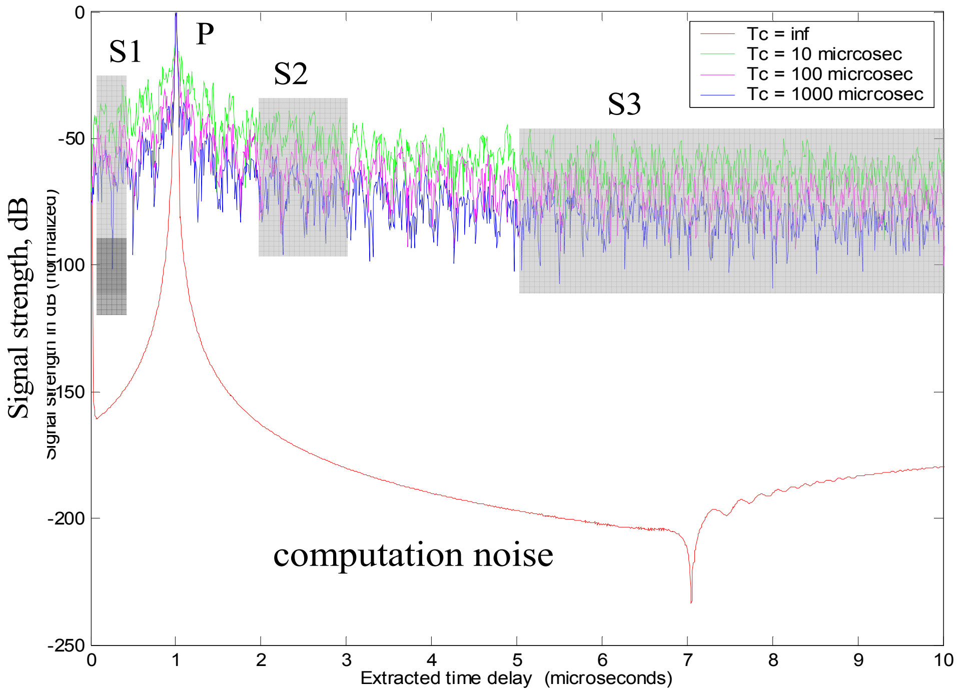

Figure 52 Power spectral density vs. extracted time delay for four different laser coherence times. The noise floor rises as the laser coherence time decreases. Three ranges where noise has been averaged have been defined S1, S2 and S3.

Noise averaging over various regions was away to check that the noise behaves the same over all the extracted time delay range of interest.

The laser coherence time, as the simulation results confirm, affects the signal dynamic range. Figure 53 depicts the signal dynamic range in terms of the inverse log of the laser coherence time in both the angled beam and collinear geometry. In calculating the signal dynamic range, the noise level was averaged over the different ranges defined in Figure 52. The results show that as the signal dynamic range degrades as the laser coherence time decreases.

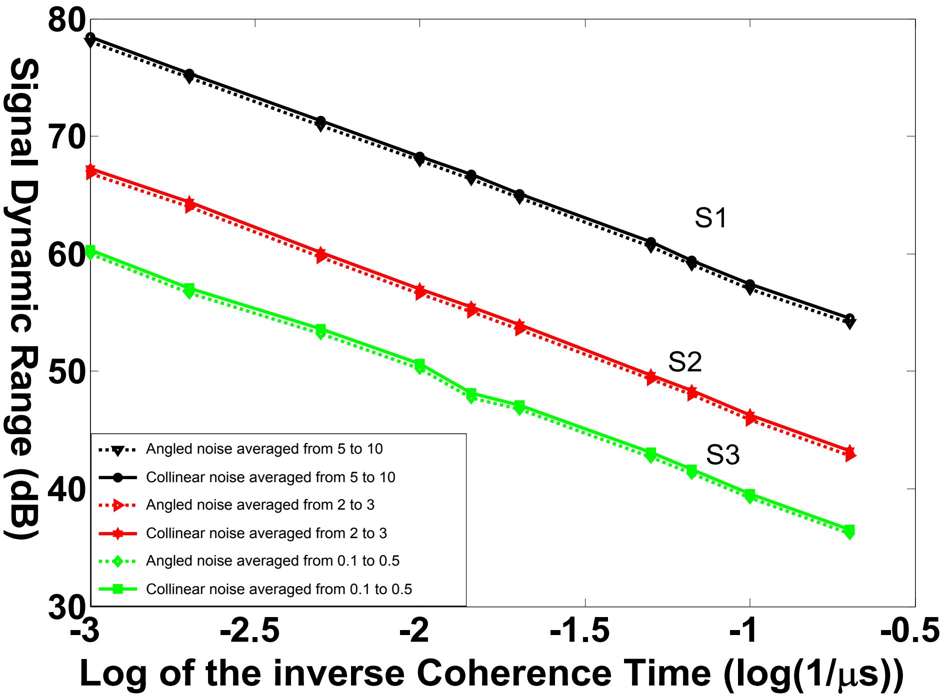

Figure 53 Signal dynamic range in terms of the log of the inverse of the coherence time. The noise level was averaged over different ranges. The Laser coherence time linearly affect the signal dynamic range. Both the angled beam and collinear geometry show similar behavior

Another set of simulations was run to understand the effect of changing the chirp bandwidth and duration on the signal dynamic range. The chirp rate was kept constant at 4 MHz/μs but the chirp bandwidth was increased to 320 MHz and the chirp duration was set to 80 μs. Figure 54 depicts the simulation results. One should note that the simulations were only run once due to the increase in computational time.

Figure 54 depicts the dynamic range in terms of the log of the inverse of the coherence time. The dynamic range in both Figure 52 and Figure 53 shows similar dynamic range in the case where the noise was averaged over the ranges S1 and S2.

However, in the case where the noise was averaged over the S3 range the difference in dynamic range is significant. For a higher chirp bandwidth the noise floor (S3) seems to be higher than in the case where lower chirp bandwidth was used.

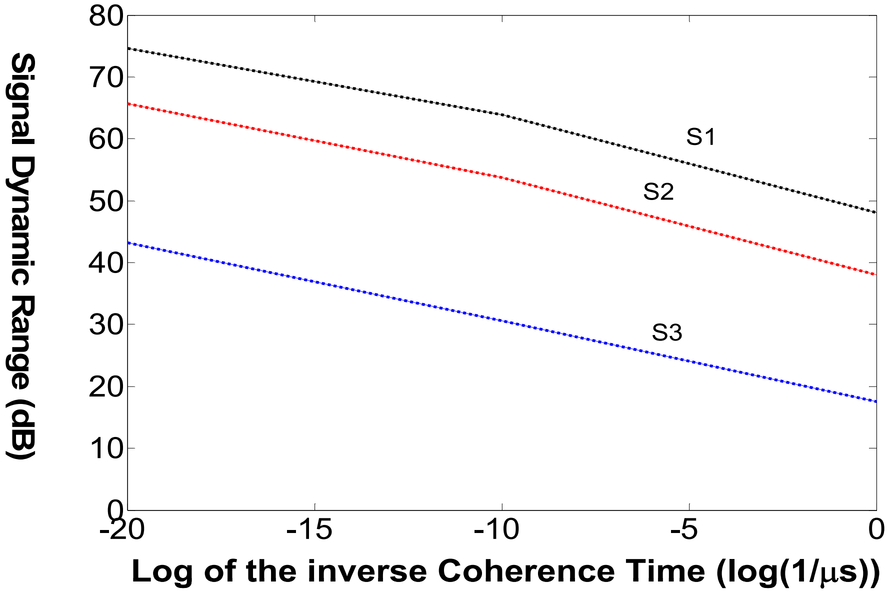

Figure 54 Signal dynamic range in terms of the log of the inverse of the coherence time. The noise level was averaged over different ranges. The chirp bandwidth was set to 320 MHz and chirp duration to 80 μs. The Laser coherence time linearly affect the signal dynamic range. Each graph represents both the angled and the collinear geometry output signal dynamic range

Delay Varying Effect on the Signal Dynamic Range

The results of the simulation where the peak delay was varied for two laser coherence time values are shown in Figure 55 (laser coherence time = 10 μs) and Figure 56 (laser coherence time = 100 μs). The noise level was averaged over 2 μs range, the averaging started about 1.5μs away from the delay peak.

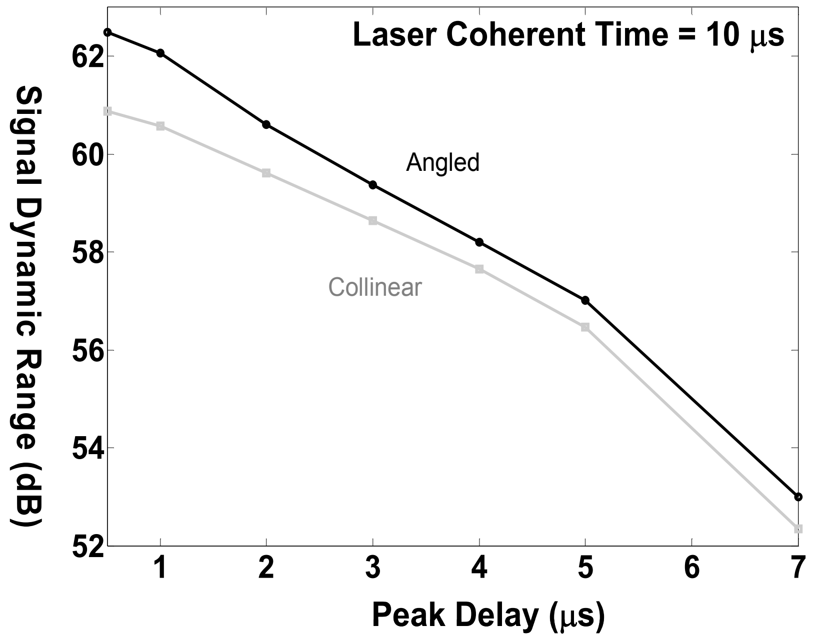

Figure 55 Signal dynamic range in terms of the peak delay for both the angled beam and collinear geometry. The laser coherence time was set to 10 μs

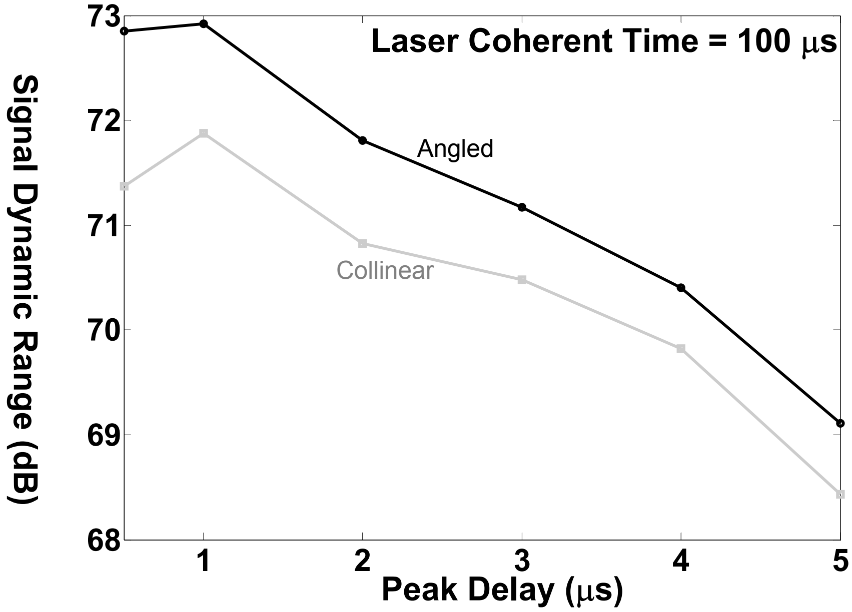

Figure 56 Signal dynamic range in terms of the peak delay for both the angled beam and collinear geometry. The laser coherence time was set to 100 μs

As expected, the angled beam geometry resulted in a better dynamic range compared to the collinear geometry. In both cases where the laser coherence time is fixed at 10 μs and 100 μs the signal dynamic range degrades as the peak delay increases.

Results Summary and Discussion

The results presented in this chapter show that the laser coherence time on the readout process affects the noise level of the output signal. As the coherence time of the laser decreases the noise level tend to increase. By running multiple iterations and averaging over different ranges, we showed that the noise floor increases steadily as the laser's coherence time decreases.

Varying the chirp bandwidth and the chirp time while keeping the chirp rate constant, showed that the noise floor is still affected by the laser's coherence time, though changing the chirp bandwidth and time shifts the noise floor. We can conclude that the signal dynamic range degrades for shorter laser coherence time.

Varying the grating period had an impact on the signal dynamic range. The results reflect that the dynamic range degrades as the delay gets longer. As far as geometry is concerned, the angled beam geometry showed a better signal dynamic range then the collinear geometry. Also, one can note that when comparing the varying delay for the two values of the laser's coherence time, the results are consistent with the first section that suggested that the short laser coherence time degrades the signal dynamic range.

CHAPTER NINE

ANGLED BEAM GEOMETRY

Introduction

This chapter presents a comparison of the collinear geometry and angled beam geometry. The heterodyne detection scheme in angled beam geometry is discussed, the simulation results show the advantages of the angled beam geometry over the collinear geometry based on the distortion and noise level.

As defined earlier, the dynamic range is defined as the processed signal strength relative to the noise level and the spur free dynamic range (SFDR) is defined as the processed signal strength relative to the highest spur. Spurs can arise from different sources, such as intermodulations, harmonics, and even sidelobes when coded waveforms are used to program the medium. The distortions and spurs may be different in the signal processing using S2 material due to its uniqueness such as the material nonlinearity, processing and readout causality, and the photodetection scheme. The comparison of different processing geometries and heterodyne detection schemes is the focus of this work.

The collinear geometry is used in S2CHIP architectures for its elegance and simplicity in beam alignment, low component count, and relaxed requirement for spatial holographic stability of the optical assembly. Despite these advantages, there are several disadvantages to a collinear geometry, which are mitigated by using angled beams. The advantages of the angled beam geometry, despite the added complexity, are presented in this work. Two different heterodyne detection schemes in angled beam geometry, “clean” reference and “auto” reference, are considered.

(a) Processing

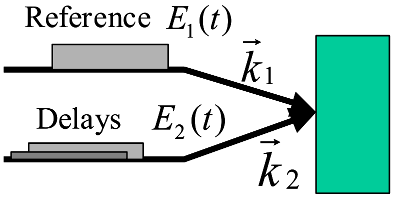

(b) Readout (“clean” reference)

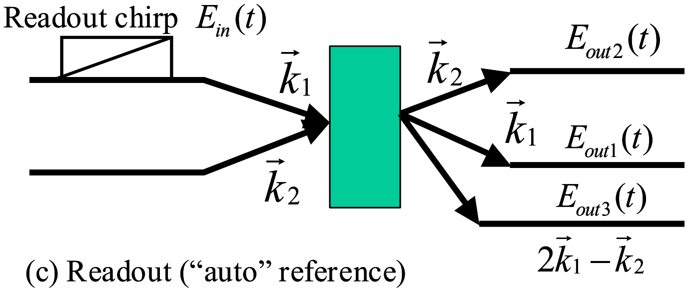

(c) Readout (“auto” reference)

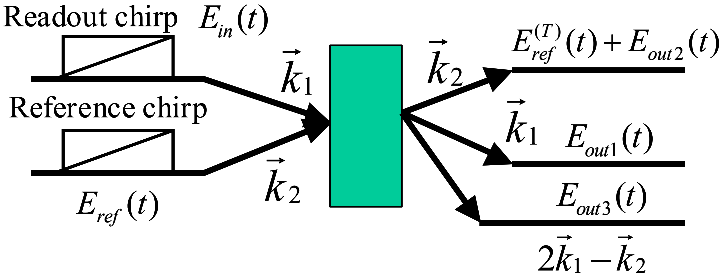

Figure 57 The angled beam geometry for signal processing and readout.

Shown in Figure 57 are the three different cases in the angled beam geometry studied in this chapter. The first one depicted in Figure 57 (a) represents the processing or the programming method, where a reference and delays representing the return signals are spatially separated by a small angle to program the medium.

The second and third cases represent the “clean” reference[5], and the “auto” reference[6] respectively. In the clean reference case, Figure 57 (b), readout chirp is in the $\vec{k}_1$ direction, the transmitted field will appear on the same direction at the output. The different order echo fields will occur at different spatial directions. For the auto reference case, the transmitted field along with the echo will occur on the $\vec{k}_2$ direction. Note that the simulations and analysis was done by the author based on the calculations done by Dr. Tiejun Chang which will be published in the near future. The results and analysis shown in this chapter has been presented in [13].

Analysis of S2 Processing with Multiple Delays

Simulation Settings

The case of multiple delayed signals is considered, where a coded waveform is used and followed in time by multiple delayed replicas, The S2 grating is then readout with chirped pulse. The simulation is run for both the clean and auto reference cases. BPSK random coded waveforms have been used to program the medium, which was considered thin and no integration was performed. The parameters summary is shown in Table 16.

---

[5] The name “clean” reference comes from the fact that the beat signal is obtained by beating the programming reference field, which have no distortions and thus clean, which the output echo fields.

[6] The “auto” reference is named so because the beat signal is obtained by beating the transmitted readout field with the output echo fields, unlike the clean reference the transmitted field contains distortion.

Table 16 Simulation parameter setting for angled beam multiple delay case

	Parameters		Symbol	Value
Computation	Temporal	Computation time	T	11.5 μs
		Number of points	N_t	230000
	Spectral	Computation Bandwidth	B	100 MHz
		Number of points	N_s	200000
	Spatial	beam	*	4
		step	*	8
Input pulses	Programming pulses	Area per bit	*	0.0025
		Shape	*	P (pattern)
		Type	*	S (square)
		Width (for a single bit)	*	0.001 μs
		Number of bits	*	1000
	Readout pulse	Rabi Frequency	Ω_c	0.0001
		Shape	*	S/C
		Type	*	C
		Chirp Bandwidth	*	160 MHz
		Chirp Width	*	40 μs

Simulation results

Intermodulation

The results depicted in Figure 58 show the sidelobes and intermodulations for different geometries, (a) collinear geometry, (b) angled geometry with "clean" reference, and (c) angled geometry with "auto" reference. The case studied considers the regime where the delay $2\tau_1 > \tau_2$. Comparing the different cases, it is clear that in the clean reference case, the intermodulation $\tau_2 - \tau_1$ as well as the DC sidelobe (DCSL) are minimized compared to the collinear and auto reference case.

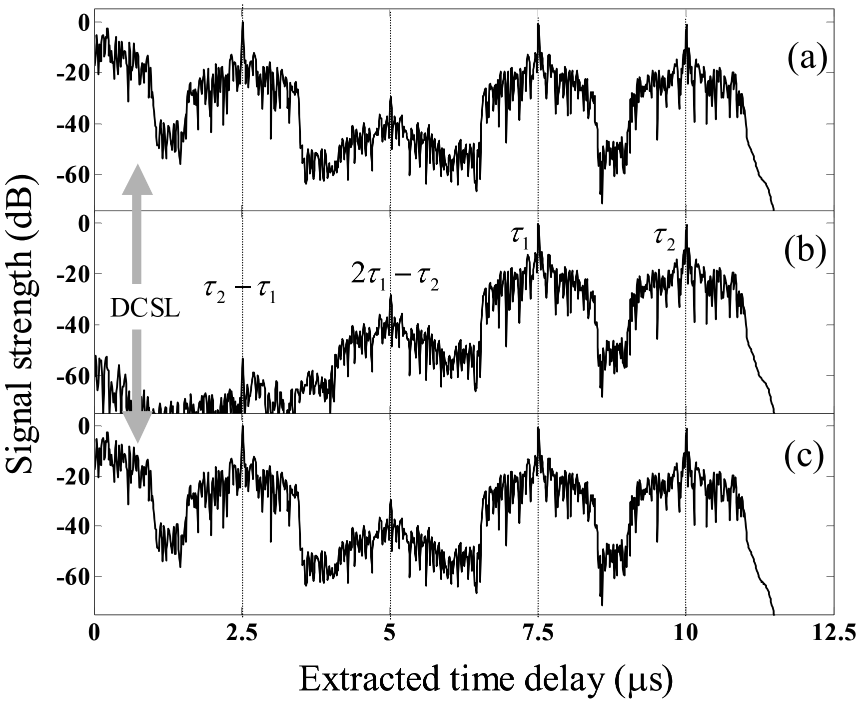

Figure 58 Simulations for showing the sidelobes and intermodes for different geometries; (a) collinear geometry, (b) angled geometry with "clean" reference, and (c) angled geometry with "auto" reference. This is for the case of $2\tau_1 > \tau_2$.

The cases where $2\tau_1 > \tau_2$ and $2\tau_1 < \tau_2$ were studied, the same settings as shown in Table 16 applied to the simulations with the exception that the temporal position of the programming pulses changed in positions. As depicted in Figure 59, for the case where $2\tau_1 > \tau_2$, it shows that the clean reference method minimizes the intermodulation $\tau_2 - \tau_1$. However, the intermodulation $2\tau_1 - \tau_2$ is the same for both geometries. One should also note that the intermode $2\tau_1 - \tau_2$ is single sided in this case. In the second case where $2\tau_1 < \tau_2$ both the intermodulations $\tau_2 - \tau_1$ and $\tau_2 - 2\tau_1$ have been minimized.

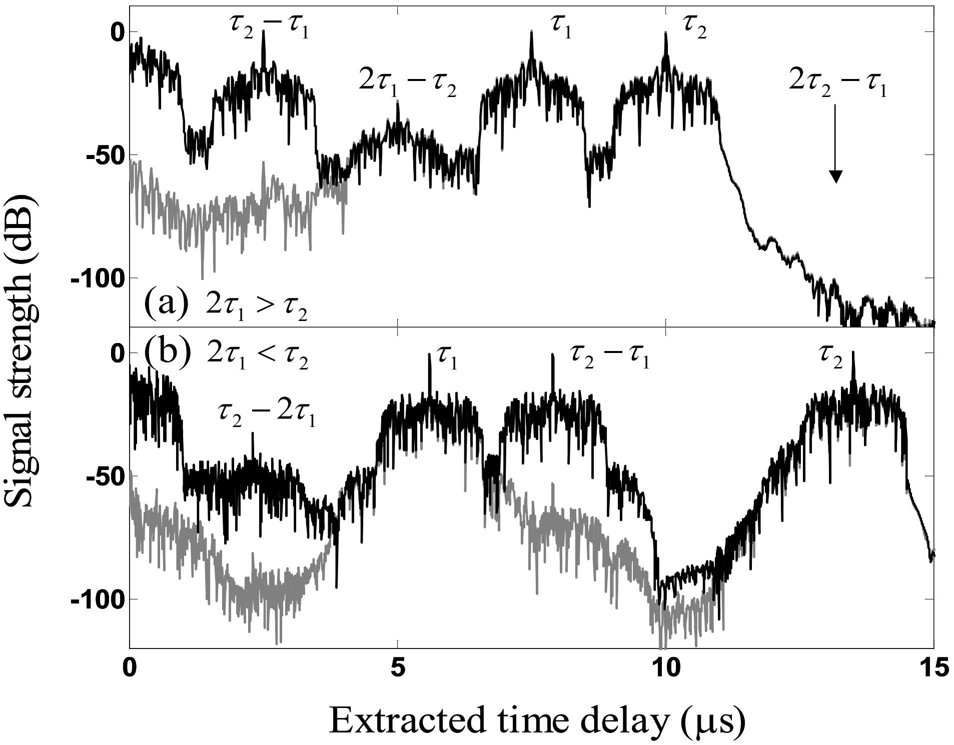

Figure 59 multiple delay output signal for the cases where (a) $2\tau_1 > \tau_2$ and (b) $2\tau_1 < \tau_2$ for both the collinear beam geometry (black) and clean reference angled beam geometry (gray)

Study of Sidelobe Reflection

Before we present the results in this section, we first answer the question: where do reflections come from that cause the sidelobe level to increase? We assume that different coded waveforms are used to program the medium, where one represents the reference and the other the return, and another chirped pulse is used to probe the medium. If the two programming pulses are separated in time, as depicted in Figure 60 (a), once probed and run through a PDS function, one would expected peaks at times τ_d and $-\tau_d$, equivalent to the time between the centers of the programming peaks. The sidelobe length equals the coded waveform length. Once the programming waveforms start to overlap as shown in Figure 60 (b), the peaks get closer to each other and the sidelobes from both sides start to interfere. This interference causes the sidelobe level to increase. Note that this discussion pertains to the collinear geometry, and that the order at which the pulses are incident on the material is actually the reverse of what is shown in the figure.

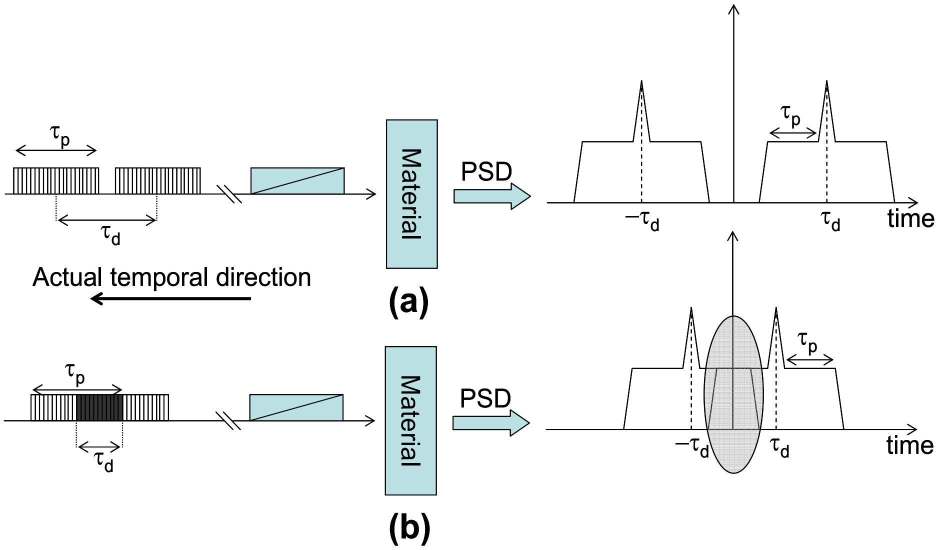

Figure 60 Illustration for programming using two coded waveforms (a) non-overlapped (b) and overlapped. When the programming waveforms overlap the sidelobe form both sides start to interfere which causes the sidelobe level to increase

In the angled beam geometry where the pulses are spatially separated, and as will be shown in the results, the sidelobe reflections are mitigated. The example is shown in Figure 61, where the programming and readout pulses are incident on the medium from different spatial directions.

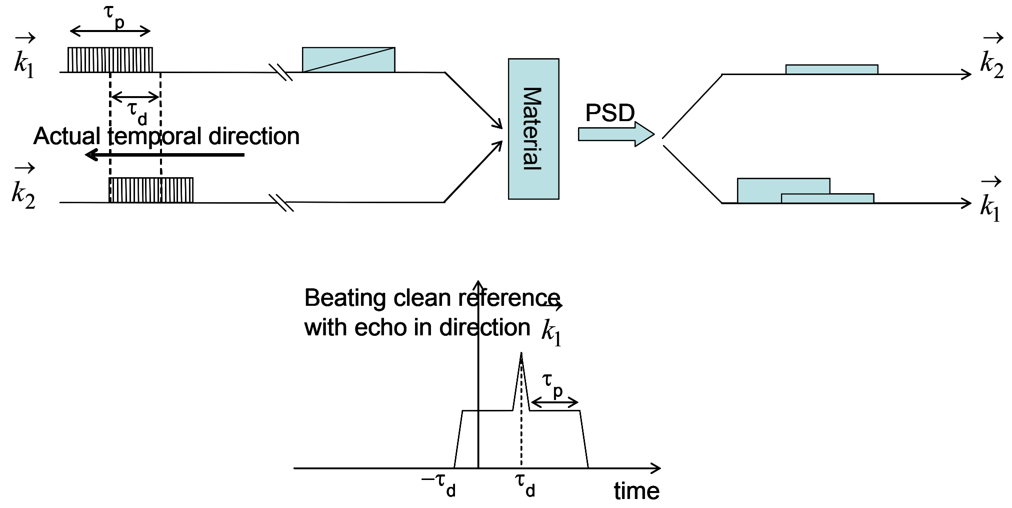

Figure 61 Angled beam geometry in programming using a coded waveform, the echo in direction $\vec{k}_1$ beaten with a clean reference produces a single sided delay which prevents interference and no sidelobe reflection is observed.

The physics is more complex yet, conceptually, when the reference and return signal overlap, sidelobe reflections are manifested in the output beat signal. As the results demonstrated when angled beam geometry is used the sidelobe reflections are mitigated compared to the collinear geometry.

Simulation Settings

To visualize the effect of sidelobe reflections, two simulations were set up. In the first simulation, the reference and return coded waveforms are overlapped such that there is a 50% overlap region between the two waveforms. The second simulation consisted of separating the pulses such that the pulses are not overlapped. The simulation parameter settings are summarized in Table 17, where the only difference between the two simulations resides in the temporal position of the reference and return signal in the programming stage. Chirped pulses were used to probe the medium and the output intensity was run through the PSD function using 2^16 FFT points as discussed in detail in previous chapters. One should note that the same random code was used for the reference and the return pulses for all the simulations.

Table 17 Simulation parameter setting for studying sidelobe reflection

	Parameters		Symbol	Value
Computation	Temporal	Computation time	T	3 μs
		Number of points	N_t	60000
	Spectral	Computation Bandwidth	B	100 MHz
		Number of points	N_s	100000
	Spatial	beam	*	4
		step	*	8
Input pulses	Programming pulses	Area per bit	*	0.0025
		Shape	*	P (pattern)
		Type	*	S (square)
		Width (for a single bit)	*	0.001 μs
		Number of bits	*	1000
	Readout pulse	Rabi Frequency	Ω_c	0.0001
		Shape	*	S/C
		Type	*	C
		Chirp Bandwidth	*	160 MHz
		Chirp Width	*	40 μs

Simulation Results

As depicted in Figure 62 (a), a comparison between the angled beam and collinear geometry shows that the sidelobe level in the collinear case is higher than the angled beam case, as expected from the predictions. To prove that the sidelobe reflection does not occur in the angled case, Figure 62 (b) illustrates a comparison between two cases in the angled beam geometry. The gray line (with the extracted time delay scale on the bottom) represents the case where the reference and return signals are not overlapped and the black line (with the extracted time delay scale on the top) corresponds to the case where the pulses are overlapped. For comparison the overlapped case was shifted such that the peaks of the two curves line up. As can see from the results, the sidelobe level in the overlapped case matches the one in the non-overlapped case showing that no sidelobe reflection effect occurred.

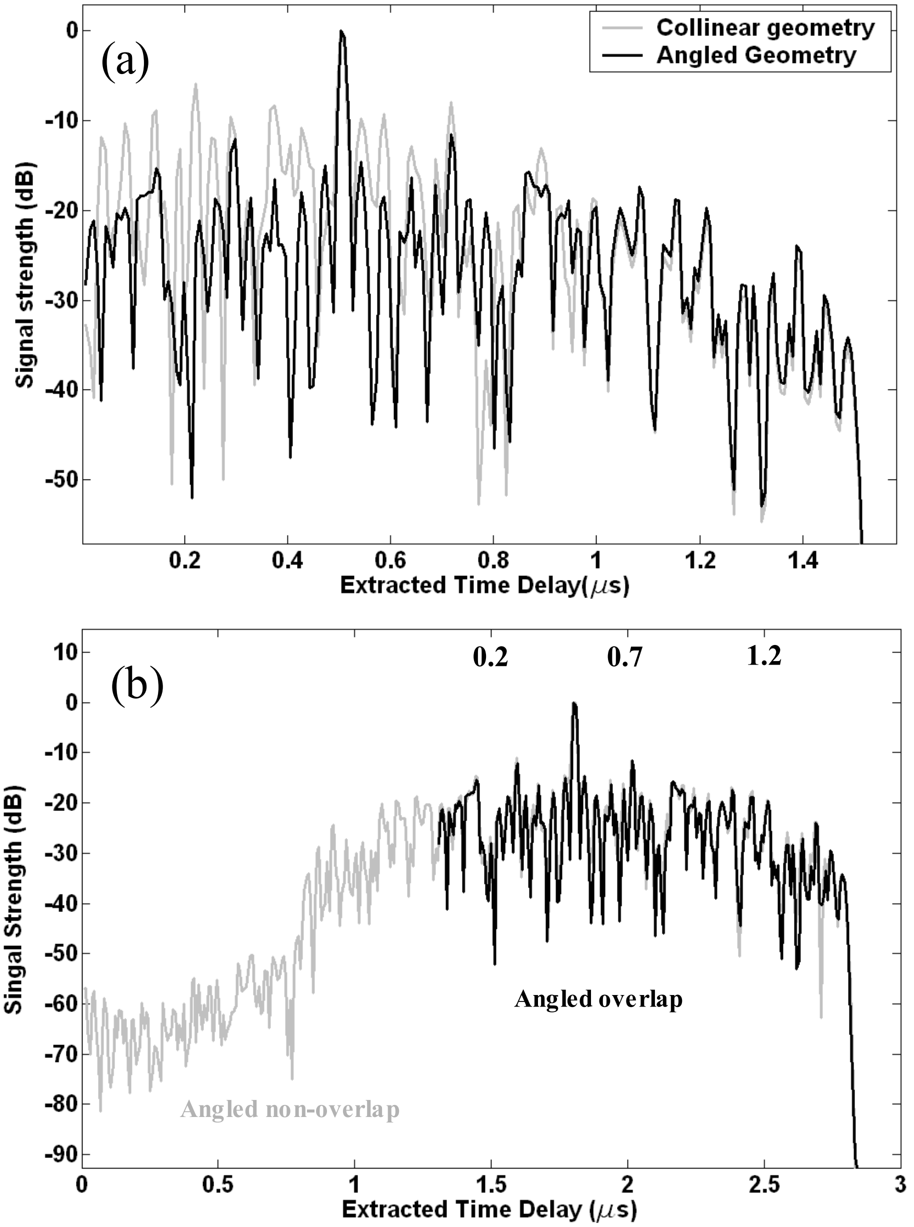

Figure 62 Sidelobe reflection is removed in angled beam geometry. (a) comparison of collinear geometry and angled beam geometry. (b) comparison of overlapped and non-overlapped waveform in angled beam geometry, where overlapped signal is shifted

Adjusting Reference

In post detection, analog to digital converters (ADCs) are used to digitize the output signal for processing. Inherently, the echo amplitude is much smaller than the transmitted field since the echo field amplitude depends on the grating strength. The heterodyne detection signal is the beat of the reference field and the echo fields. Contrary to the collinear geometry the reference is adjustable in the angled beam geometry, including "auto" reference method. The advantage of having an adjustable reference resides in the fact that the vertical resolution of the ADC is fully utilized. The beat signal in the collinear geometry case $S_c(t)$ consists of beating the output transmitted field E_{trans} with the output echo field E_e, where $S_c(t) = \left|E_{trans} + E_e\right|^2$. In the angled beam case, the beat signal $S_A(t)$ consists of beating the reference field E_{ref} with the output echo field E_e, where $S_A(t) = \left|E_{ref} + E_e\right|^2$.

When the reference is adjusted, the beat signal $S_A^{'}(t)$ becomes:

$$\begin{aligned} S_A^{'}(t) &= \left|\eta E_{ref} + E_e\right|^2 \\ &= \eta^2 \left|E_{ref}\right|^2 + \left|E_e\right|^2 + \eta E_{ref} E_e^* + E_{ref}^* E_e \end{aligned} \tag{9.1}$$

Where η is the adjusting factor. The reader might note that only one of the cross terms in the equation is causal. If the reference occurs at time t_0 and the echo occurs at time t_1, then the first cross term in the equation will have a delay t_0-t_1, and the second term will have a delay t_1-t_0 which makes this last causal and the first noncausal. The first term in $S'_A(t)$ is the transmission of the reference, the second term is the echo field, and the fourth term is the desired signal.

Figure 63 depicts the normalized beat signal of the angled (in black) and collinear (in gray) geometry. The angled beam reference field was adjusted in the angled beam geometry. Comparing the two curves one notices that the modified beat utilizes the vertical resolution of the ADC better than the original collinear beat.

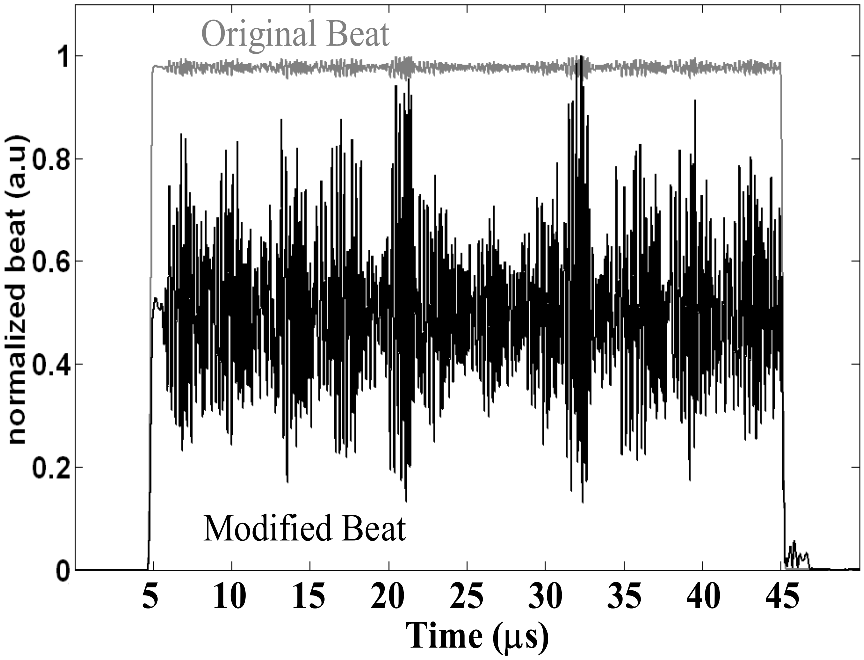

Figure 63 Adjusting the reference amplitude to fully utilize the vertical resolution of analog to digital converter. The gray curve is the readout signal from collinear geometry and the dark curve is the readout signal from the adjusted reference in angled beam geometry.

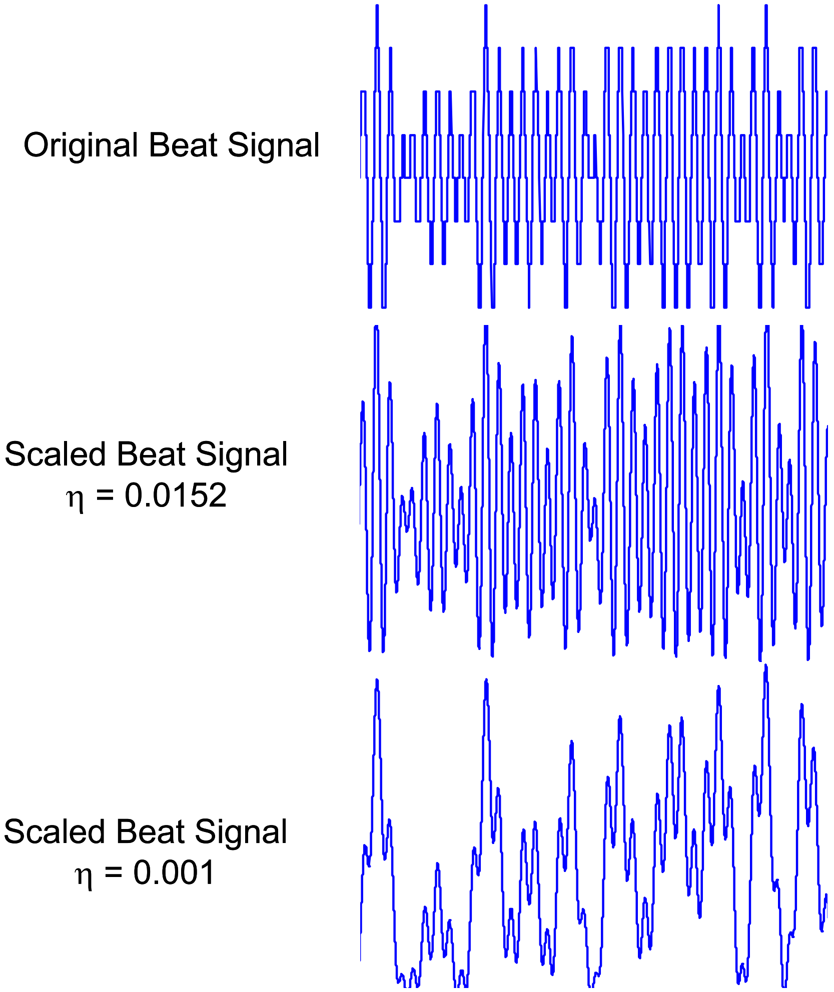

Figure 64 Comparison between the original beat signal and scaled beat signals digitized with 8-bit resolution

As depicted in Figure 64, the scaled signals showed a better vertical resolution use than the original beat signal which corresponds to the collinear geometry case. However, one must choose the scaling factor carefully. Close examination of equation (9.1) reveals that the scaling factor does not only affect the reference that is scaled but it also affect the third term in the equation which contains the intermodulation parameters. For a small scaling factor, the intermodulations ignored when the reference is big, become significant when scaling occurs. As shown in Figure 65, where the signal strength is plotted against the extracted time delay, one can clearly see that for very small scaling factors the intermodulations start to manifest.

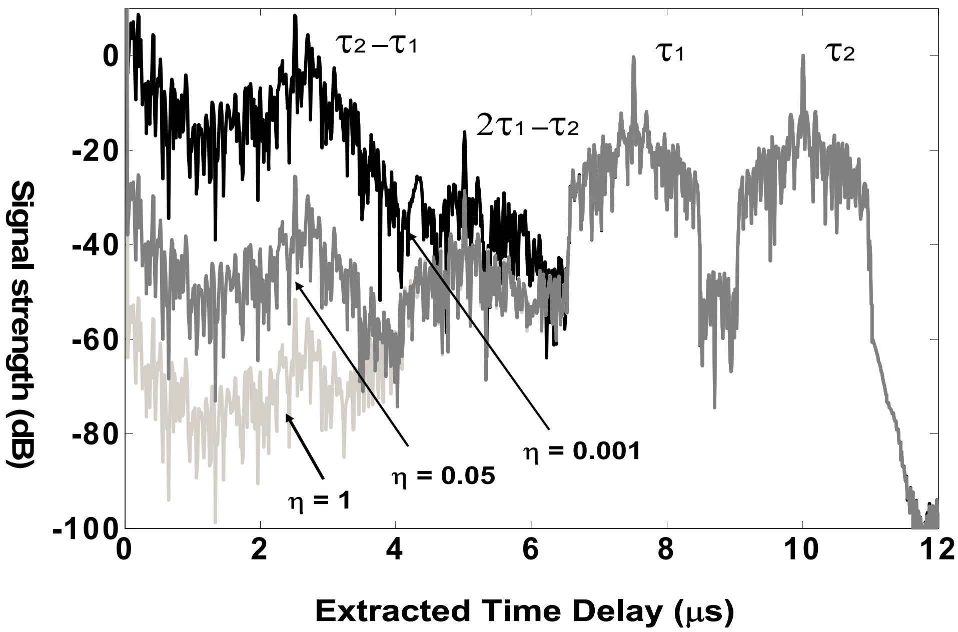

Figure 65 Signal strength vs. extracted time delay, with varied scale factor as 1, 0.05, and 0.001

Figure 66 illustrates how the intermodulations behave in terms of the scaling factor. The horizontal dashed line represents the point where the reference and echo have the same magnitude. The two principal peaks τ_1 and τ_2 are independent of the scaling factor. However, the intermodulation τ_3 shows about a 20 dB/dec slope but the intermodulation τ_4 a non-linear behavior with respect to the scaling factor.

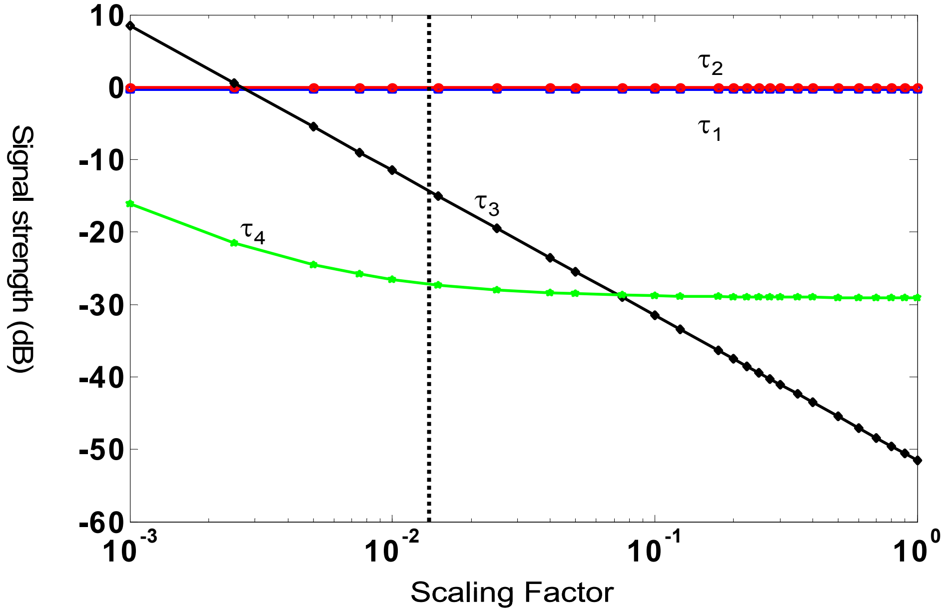

Figure 66 The normalized desired signals and intermodulations as function of adjusting factor for an 8-bit resolution

Noise Level

When using a "clean" reference, the distortions that occur in the transmitted field due to its interaction with the S2 material are eliminated. Figure 67 shows a comparison between collinear and angled beam geometries. The figure graphs the simulation results for a single delay and plots the noise floor RMS difference with a significant reduction in the noise level for the angled beam case over a collinear geometry. To address the "clean" effect in the readout processing only, a perfect single delay S2 grating in a thin material is being read out with a chirp waveform with varied amplitude. The noise level also depends on the strength of the grating to be read out. Figure 68 shows the noise level varying with the readout Rabi frequency for a fixed value of the grating strength. The big jumps around 0.5MHz are due to the saturation effects induced by the overdriving of the readout waveform.

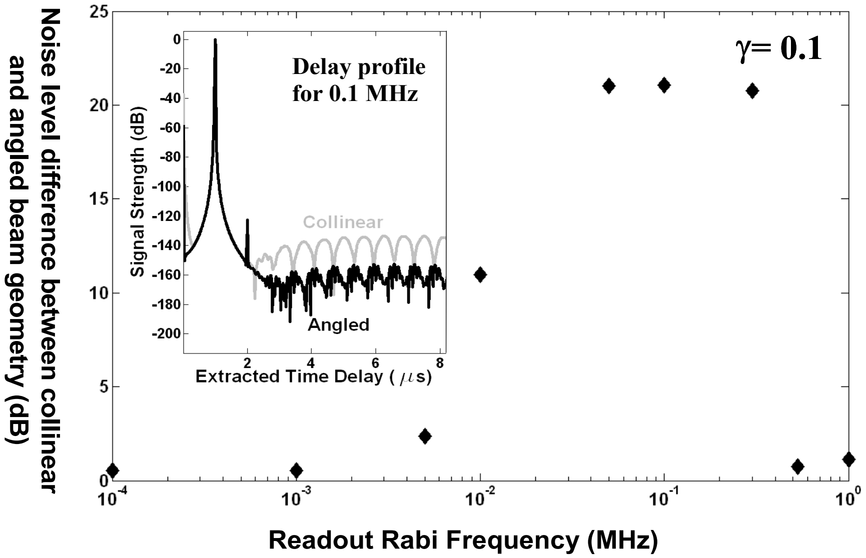

Figure 67 Noise level difference between angled and collinear geometries versus readout waveform Rabi Frequency for grating strength 0.1. Inset shows an example delay profile at 0.1 MHz, where over a 20 dB difference is observed.

The noise level also depends on the strength of the grating to be read out. Figure 68 shows the noise level as function of varying readout Rabi frequency and varying grating strength. The big jumps around 0.5MHz are due to the saturation effects induced by the overdriving of the readout waveform.

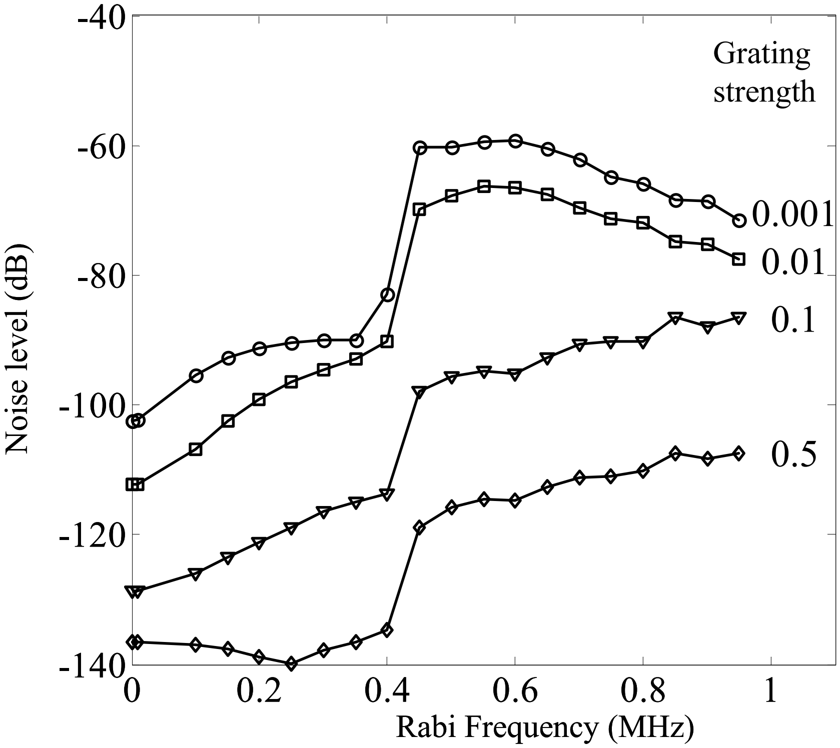

Figure 68 Noise level as function of readout Rabi frequency and grating strength

The reader should note that the simulations results presented in this section involve thin medium. In a thick medium, harmonics start to appear. [12] showed that in angled beam geometry, the harmonics due to propagation effects and nonlinearity are reduced, while the harmonics due to integration are completely removed.

Summary and Discussions

This chapter showed that the angled beam geometry requires more component count and requires a higher spatial stability then the collinear geometry. However, and despite these disadvantages, the angled beam geometry proved to have many performance advantages over its collinear counterpart.

The angled beam geometry proved able to either significantly reduce or completely remove intermodulation. Also, the use of a clean reference offers the advantage of beating the echo with a non-distorted reference which is not possible in the collinear case. Another advantage resides in the fact that the reference can be scaled, which allows for better use of the vertical resolution in digitization. Results show that sidelobe reflections are eliminated in the angled beam geometry which compared to the collinear geometry, improves on the spur free dynamic range. Finally, and as shown in [12], harmonics are removed when a thick medium is used. These conclusions show that the angled beam geometry will significantly improve the system performance in terms of reducing noise, eliminating sidelobe refection, eliminating or reducing intermodulations, and removing distortions.

CHAPTER TEN

SUMMARY

This thesis presents the characteristics of the S2CHIP under different environments in terms of signal strength, noise level and dynamic range. The characterization was achieved using the OCT simulator developed in The Spectrum Lab. Characterization involved the study of propagation, signal interference, integration, material coherence time, laser coherence time, and laser beam geometry.

In the analysis of a thick medium, the results have shown that an optimum absorption length exists where the output signal maximizes. It was also deduced that the DR and SFDR tend to degrade as the absorption length of the material increases. The use of different length coded waveform, results in better spur free dynamic range for the longer codes.

When multiple delay programming was examined, interference issues started to arise and needed to be taken into account. A calculation was presented that explained how the transmitted field and the output echo fields along with the beating of the echo fields interfere with each other. The simulation results prove that interference does occur between different delays for both the angled and collinear geometries.

Integration with multiple shot in the writing stage for a single delay case and for a multiple delays was analyzed. A slope was calculated for the different intermodulations generated due to the use of integration. The calculated slope increased as the number shots got higher. It was concluded that for a certain noise floor present in the system, an optimum number of shots can be obtained to produce the best SFDR.

In analyzing the material coherence time and how it affects the signal dynamic range, the simulation results agreed with the predictions deduced from the calculation. However, when the coherence time was a factor in both the programming and readout, and even though for the results obtained for the delays τ_1, τ_2 and τ_3 agreed with calculation, the delay τ_4 did not agree with the calculation prediction. The reason for the disagreement was associated with the non-linear behavior of the material. Overall, it was concluded that T2 affects the signal peaks independently of the delay length or the delay position ($2\tau_1>\tau_2$ or $2\tau_1<\tau_2$). The first order intermodulations are all affected linearly by the coherence decay and the third order intermodulation behaves in a nonlinear fashion. Moreover, while the use of longer coded waveforms improves the signal dynamic range, the coherence decay still degrades it. In examining the effects of the laser's coherence time, we showed that the noise floor rises due to a decrease in the laser's coherence time. The change in the delay position also proved to affect the dynamic range of the output signal.

The final analysis concerned the study of geometry, where a comparison between the angled and collinear geometry was presented. We deduced that though the angled beam geometry has some disadvantages (require more spatial stability, higher component count) it proved to be a significant improvement in the system performance by removing or reducing intermodulations, distortions.

In conclusion, out of all the characterization shown in this thesis, the system performance can be improved by an ensemble of parameter choice:

- An optimum medium thickness has to be determined for the appropriate application.
- The length and the type of codes used in the programming waveform has to be carefully selected for best spur free dynamic range
- Integration has to be used to improve on the processing gains.
- The material coherence decay though material dependent should be considered as well in the system design since it significantly affects the dynamic range.
- The programming and probing laser has to be chosen with an appropriate coherence time for better DR
- The angled geometry is to be used instead of the collinear geometry in order to obtain a better overall signal dynamic range.

All of these parameters have to be used in combinations for best system performance. Note that ongoing research on the S2CHIP proved that this revolutionary system can be used in many other applications.

REFERENCES

[1] T. W. Mossberg, “Time-Domain Frequency-Selective Optical Data Storage”, Opt. Lett. **7,** February (1982).

[2] V. Lavielle, I. Lorger, J. Le Gout, S. Tonda, and D. Dolfi, "Wideband versatile radio-frequency spectrum analyzer", Opt. Lett. **28**, 384-386 (2003).

[3] I. I. Popov, V. V. Samartsev, Atmos. Oceanic Opt. 14 (2001) 411.

[4] X. Wang, M. Afzeluis, N. Ohlsson, U. Gustafsson, S. Kröll, Opt. Lett. 25 (2000)

1473

[5] K.D. Merkel, R. K. Mohan, Z. Cole, T. Chang, A. Olson, and W. R. Babbitt, “Multi-Gigahertz radar range processing of baseband and RF carrier modulated signals in Tm:YAG”, J. Lum. **107,** 62-74 (2004).

[6] K. D. Merkel : “An Optical Coherent Transient True-Time Delay Device: Concept Development and Experimental Demonstrations Including Delay Programming With Frequency-Chirped Pulses” PHD thesis, University of Washington, 1998.

[7] M. I. Skolik, “Radar Handbook”, second edition, Mc Graw Hill, ISBN 0-07-057913-X.

[8] T. Chang, M. Tian, Wm. R. Babbitt, “Numerical Modeling of Optical Coherent Transient Processes with Complex Configurations—I. Angled Beam Geometry” J. Lumin. **107** (2004) 129–137.

[9] T. Chang, M. Tian, Z. W. Barber, Wm. R. Babbitt, “Numerical Modeling of Optical Coherent Transient Processes with Complex Configurations—II. Angled Beams with Arbitrary Phase Modulations”, J. Lumin. **107** (2004) 138–145.

[10] Carrie Cornish “Highly Efficient Photon Echo Generation and a Study of the Energy Sources of Photon Echos”, Ph.D Thesis, University of Washington, August 2000

[11] R. R. Reibel: “High Bandwidth Optical Coherent Transient True-Time Delay”, PHD thesis, Montana State University, 2002.

[12] T. Chang, R. K. Mohan, M. Tian, T. L. Harris, Wm. R. Babbitt, K. D. Merkel, “Frequency-Chirped Readout of Spatial-Spectral Absorption Features”, Phys. Rev A **70**, 063803 (2004).

[13] T. Chang, A. Khallaayoun, W. R. Babbitt, K. D. Merkel, "Advantages of an Angled Geometry in Spatial-Spectral Sensor Material for Signal Processing Applications" Accepted by HBSM 2006, june, 26-29, 2006, Aussois, France

[14] T. Chang, M. Tian, R. W. Babbitt, "Numerical Modeling of Optical Transient Processes With Complex Configuration", Accepted by HBSM 2006, june, 26-29, 2006, Aussois, France